First principles DFT study of hematite clusters on anatase TiO_2 and the effect of oxygen vacancy

M.Sc. Thesis

Kati Asikainen

Supervisors: Assa Aravindh Sasikala Devi and Matti Alatalo

Nano and Molecular Systems Research unit

Faculty of Science

University of Oulu

June 6, 2022

Abstract

The main focus of this thesis, photocatalysis, has attracted enormous attention to tackle the global energy and environmental issues. A design and synthesis of photocatalysts with high photocatalytic activities have increased the scientific interest worldwide in order to develop a green and environmentally friendly technology. Heterogeneous photocatalysis on titanium dioxide, TiO_2, is a potential solution to the issues we are facing. However, the photocatalytic efficiency of TiO_2 is greatly limited by the large band gap energy and the high recombination rate of the photogenerated electrons and holes. Therefore, attempts are made to, not only doping TiO_2 with various elements, but also loading TiO_2 surface with appropriate cocatalysts. A coupling of TiO_2 with another semiconductor with a suitable band gap and a band edge position can enhance visible light adsorption by reducing the band gap and inhibit recombination phenomena of the charge carriers.

In this thesis, hematite (α-Fe_2O_3) clusters on anatase TiO_2 (101) surface and further the effect of oxygen vacancy in the combined system were investigated. We used powerful density functional based calculations to model our systems. The simulations provided insight to phenomena occurring at the atomic level in the investigated systems and thus better understanding on photocatalytic processes on theoretical level. We found energetically favourable interaction between TiO_2 and hematite clusters, thus enabling the modification of the surface properties. Due to the adsorption, impurity states arise, narrowing the band gap of TiO_2. A notable charge transfer from the cluster to the surface was observed, which may play crucial role in the photocatalytic reactions. The band alignment of TiO_2 and hematite showed a potential formation of a heterojunction that can promote the observed charge transfer and suppress the recombination rate of TiO_2. A large Fe_2O_3 cluster size has been proposed to hinder the photocatalytic performance of TiO_2. Our results did not completely confirm or refute this claim. They suggest that the larger cluster size can have an influence on the electronic properties and thus the photocatalytic performance.

An introduction of oxygen vacancies, both at the TiO_2 and at the cluster, further altered the properties of the combined system. Oxygen vacancies can further decrease the band gap of TiO_2, thus expanding the visible light response of the system, and lead to formation of a different types of heterojunction between TiO_2 and hematite. The effect of oxygen vacancy located at the cluster is not observed to be as significant in order to decrease the band gap. In the presence of oxygen vacancy at TiO_2 we observed the direction of the charge transfer to reverse, occurring from the surface to the cluster and thus promoting the oxidization ability of TiO_2. Overall, the results indicate that hematite clusters and further oxygen vacancy can modify the surface properties of TiO_2 and the photocatalytic mechanism in the combined system. They also suggest that hematite as a cocatalyst can improve the photocatalytic performance of pristine TiO_2 surface.

Contents

1 Introduction

1.1 Semiconductor based photocatalysis

Nowadays, the environmental pollution and the challenges in environmentally-friendly energy production are among major concerns around the world. Due to the development of the industry and the improvement of standard of living, the energy consumption has greatly increased. The development of renewable energy sources has attracted a lot of attention when discussing sustainable development. Practically unlimited sunlight is available in all over the world. However, day time, weather and geographical location are factors that limit the availability of solar energy. The inefficient energy storage technology creates its own challenges for the utilization of the harvested energy. The fossil fuels have been and are still the primary energy sources on which the energy production depends on. However, their burning releases pollutants into the air and environment that threaten the life of humans and other living organisms. Another concern is that fossil fuels are limited resources that will run out as time passes. And the time is shortening as the demands for energy are growing, creating a global energy crisis.

Alongside fossil fuels, another major contribution of pollutants comes from the industry. For example textile industry, with the production of over 700 000 tons of dyes [1], generates huge amount of coloured wastewater every year which, without correct treatment, may be released into water bodies. On the other hand, the industrial processes release greenhouse gases that strengthen the climate change and other pollutants, such as small particles, to air. These effluents and air pollutants are hazardous to the health of humans and other organisms due to their possible toxic nature. There exist conventional methods for environmental clean up processes, such as biological methods and chemical precipitation to treat the wastewater [2] and for example filters and absorbents that prevents pollutants from entering the air. However, each method has its weaknesses in the removal process. For example, the filters are needed to be replaced frequently as their efficiency decreases over time. Therefore, the removal of a pollutant is still a challenging task.

Semiconductor-based photocatalysis, utilizing only solar radiation, has shown a great potential to solve the issues discussed above. The first evidence of the method was published in 1972 by Fujishima and Honda [3]. They demonstrated the splitting of water into hydrogen and oxygen by UV-light in a photoelectrochemical cell, in which TiO_2 was used as photoanode. Hydrogen has a high energy density of 140 kJ/g [4] which makes it one of the most promising energy carriers. Therefore, photocatalysis has attracted attention as it can be used to convert solar energy into chemical form, hydrogen, without producing environmental pollutants. In 1977 the application of photocatalysis in wastewater treatment was promoted by Frank and Bard as they successfully used TiO_2 as a photocatalyst to oxidize CN^- to OCN^- [5]. These early investigations have promoted the interest of the applications of photocatalysis and numerous studies have been published during last years and the trend has been growing [6]. Currently, the research of applications of photocatalysis focuses on the photocatalytic hydrogen production and energy conversion, wastewater treatment as well as many other applications, such as disinfection and inactivation of viruses and bacteria.

Photocatalysis is a chemical reaction powered by light, occurring in the presence of catalyst. The semiconductor based photocatalysis, classified as heterogeneous photocatalysis, uses semiconductors in a solid form as photocatalysts. For light to be absorbed by semi-

conductor the photon energy must be equal to or greater than the band gap energy of the semiconductor. The light absorption of the catalyst creates photoexcitations of electrons to the conduction band while holes are left in the valence band. This produces electron-hole pairs. The photogenerated electrons and holes can diffuse to the surface of the photocatalyst and act as a reductant and an oxidant, respectively, to reduce and oxidize substances which are adsorbed on the surface of the photocatalyst. Thus the photocatalyst act as a redox system in which reduction and oxidation processes occur simultaneously, taking place at the interface between solid, i.e. photocatalyst that provides an active site for the reaction, and substance in liquid or gas form. The catalyst itself does not undergo any changes. The opposite to a heterogeneous photocatalyst is a homogeneous photocatalyst which is present in the same phase as that of the substance in reactions. However, easy separation from the reaction mixture and reuse make heterogeneous photocatalysts advantageous over the homogeneous photocatalysts.

Since the discoveries of Fujishima and Honda, and Frank and Bard titanium dioxide TiO_2 has been the most extensively studied and widely used photocatalyst in many applications due to its advantageous properties: strong oxidizing power [7], chemical stability, non-toxicity and low cost. However, several drawbacks of TiO_2, such as large band gap of 3.0 eV, high recombination rate [8] and low porosity [9], restrict its efficient application. A lot of research has been made to overcome the limitations and enhance the photocatalytic performance of TiO_2 by doping it with various elements, introducing cocatalysts and exploring the increased surface area by making it in nano-dimensional [10, **?**].

TiO_2 is by no means the only photocatalyst but the research has also extended to investigate other possible photocatalytic materials as well. Among semiconductors, CdS and bismuth based materials are found to be promising materials for the photocatalysts [12, 13]. Of other metal oxide semiconductors, such as ZnO, SnO_2 and Fe_2O_3, are also potential candidates. Of those, iron oxide Fe_2O_3 and more specifically, its phase hematite, α-Fe_2O_3, has been under great attention. It is low-cost, non-toxic and has a good chemical stability as TiO_2 but the narrower band gap of only 2.2 eV makes it capable of absorbing a large portion of visible solar spectrum. Thus, the redox reactions taking place in Fe_2O_3 can be powered by visible sunlight without the production of pollutants to the environment. Due to these advantageous properties hematite is also considered to be a promising and environmentally friendly photocatalyst for the photocatalytic applications.

1.2 Iron oxides and hematite

Iron oxides are some of the most common compounds in nature. There exist 16 different iron oxides which are categorized to three classes: oxides, hydroxides and oxide-hydroxides depending on whether they are composed of iron together with oxygen and/or hydroxide [14]. Of iron oxides, FeO, known as wüstite, has the simplest crystalline structure, similar to that of sodium chloride (NaCl). It is one of the iron oxides which contains the divalent iron. Thermodynamically the most stable structure under ambient conditions is hematite, α-Fe_2O_3, which is considered in this thesis. It can be formed by oxidation of magnetite at room temperature according to the reaction [15]

$$4Fe_3O_4 + O_2 \rightarrow 6Fe_2O_3.$$

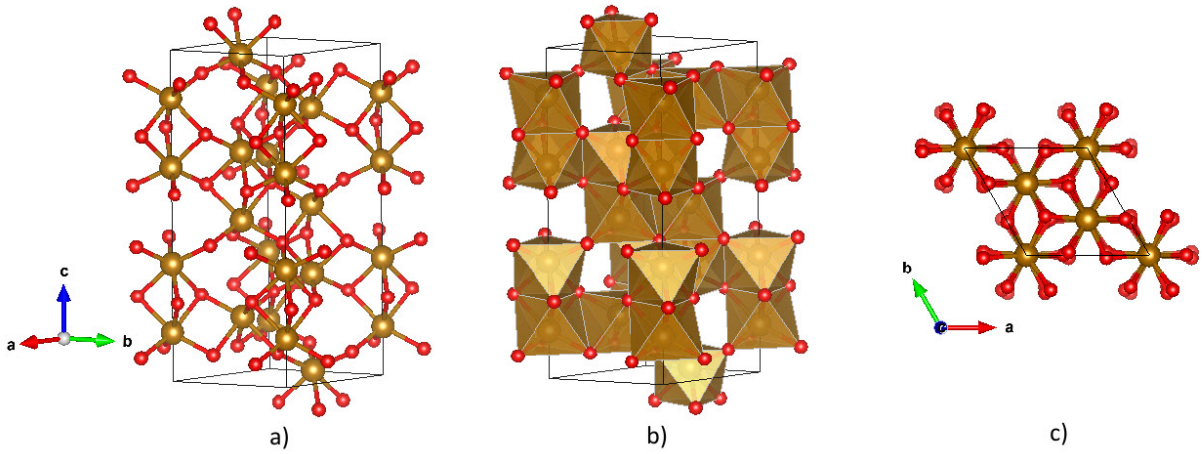

Figure 1: Schematic illustration of the crystal structure of a) hexagonal unit cell of α-Fe_2O_3 b) with polyhedral representation containing 6 formula units. c) Top view of the crystal structure of hematite. Iron atoms are marked as brown and oxygen atoms as red.

Hematite is one of the phases of iron (III) oxide. Three other crystalline polymorphs are β-Fe_2O_3, γ-Fe_2O_3 (known as maghemite) and ϵ-Fe_2O_3.

Hematite, widespread in rocks and soils, is a transition metal oxide which crystallizes in the corundum structure [16], thus belonging to the transition-metal sesquioxides the chemical formula of which has a form of α-A_2O_3 [17]. For hematite, A = Fe. Hematite has a crystalline form of the rhombohedral lattice system with space group $R3c$. The unit cell of hematite is hexagonal with lattice parameter $a = 5.035$ Å and $c = 13.747$ Å [18] which contains six formula units per unit cell. The unit cell is shown in Figure 1. The structure of hematite consists of hexagonal close-packed system. Oxygen ions, O^{2-} are arranged along the (001) plane while Fe^{3+} ions occupy two-thirds of the octahedral sites in the (001) basal plane [14] (Fig. 1c)). The particular arrangement of iron ions produces pairs of $Fe(O)_6$ octahedra (Fig. 1b)). The octahedron is trigonally distorted (Fig. 1a)) due to the fact that O-O distance along the shared faces of an octahedron are shorter than along the unshared faces Each of the iron atoms is surrounded by six oxygen atoms in the structure. Alternatively, α-Fe_2O_3 can be also described as a rhombohedral system which have three equal axes ($a = 5.43$ Å) with an angle of 55.3° between the edges [16, 17].

Hematite is an n-type semiconductor with favourable band gap of $2.0 - 2.2$ eV [19, 20], making it capable of absorbing visible light. The band gap is determined to be indirect, originating from Fe^{3+} d-d excitations. Direct, optical band gap is reported to be around 2.7 eV which corresponds the transition from O^{2-} 2p orbital to Fe^{3+} 3d orbital [20]. The band gap and its definition has been investigated, whether it is defined by d-d transition or O^{2-} 2p - Fe^{3+} 3d transition. That is related to the insulating behaviour of hematite that has been debated a lot whether hematite is described as Mott Hubbard insulator or charge transfer insulator [21, 22]. Previous experimental [22, 23] and theoretical [17, 24] studies have confirmed that, as valence band edge is dominated by oxygen 2p states and conduction band by iron 3d states, hematite is considered as a charge transfer insulator rather than a Mott insulator.

The charge transfer in α-Fe_2O_3 is dominated by the small polaron hopping [25]. In many transition metal oxide semiconductors charge carriers are self-trapped in a potential well

resulting from the ionic displacements the charge carrier created. This is called a polaron. The polaron is said to be small if it is confined to a volume which is smaller or equal to one unit cell. The charge carriers, localized in potential wells, can hop from one to another suitable position by lattice distortion associated with it. In hematite the excess electrons, usually forming those small polarons, are self-trapped at the localized potential wells at the Fe cations [26]. The sufficient motion of the phonons can bring Fe cations closer to each other and provide the needed thermal energy, allowing the electron transfer between atoms. The charge migrates with the hopping electron (see Fig. 1 in [26]).

However, Hematite has been reported to have a low electrical conductivity, $10^{-14}(\Omega\text{cm})^{-1}$, at room temperature [27]. Moreover, the studies have revealed a large anisotropy of the conductivity. The conductivity along the (001) basal plane has been observed to be four times larger than the conductivity parallel to the [001] direction (parallel to the c axis of the unit cell) [28]. This has been explained by the magnetic ordering of the hematite crystal. Along the [001] direction the Fe atoms, which are all in high spin configuration, couples antiferromagnetically whereas ferromagnetically in the (001) basal plane [26]. The ferromagnetic ordering allows excess electrons to be transferred to different Fe sites in the same (001) basal plane which is forbidden along the [001] direction.

The bulk hematite shows interesting magnetic properties. Between the Neél temperature (955 K) and the Morin temperature (263 K), and therefore also at room temperature, α-Fe_2O_3 is weakly ferromagnetic. The Fe ions are antiferromagnetically coupled across the shared faces of the FeO_6 octahedra along the [001] direction. However, in the basal plane the spins are not completely parallel, leading to a weak spontaneous magnetization. Below the Morin temperature the spins in the basal plane reorientate to the angle of 7° to the [001] direction. At this spin structure the spins are antiparallel and hematite become antiferromagnetic.

Several theoretical studies of hematite have been reported. Standard density functional theory (DFT) calculations with local density approximation (LDA) or generalized gradient approximation (GGA) functionals (see Section 2.5) are known to yield incorrect results for α-Fe_2O_3. The band gap is predicted to be too small and incorrectly Mott Hubbard insulator-type [24]. Even a metallic behaviour may be predicted. In addition, the predicted magnetic moment is generally too small. The experimentally determined magnetic moment of hematite has a value of 4.9 μ_B [29]. Both the LDA and the GGA functionals yield incorrect predictions because they ignore the on-site interaction between localized d-electrons in transition metals. The more realistic electronic structure for α-Fe_2O_3 can be obtained using hybrid functionals, that involve a portion of exact Hartree-Fock exchange energy in the exchange-correlation functional or Hubbard correction [17, 24] which we used in this thesis. It is introduced in Section 2.6. A Hubbard correction of around 4 eV has been observed to be optimal for α-Fe_2O_3 and yield results being consistent with the experimental results [17, 24, 30, 31].

1.3 Hematite as photocatalyst

α-Fe_2O_3 has been considered as a promising photocatalyst due to the tolerable band gap of around 2.0 eV but essentially it is also non-toxic and environment friendly. However, pure α-Fe_2O_3 is a poor photocatalyst, similarly as pure TiO_2. Its performance is generally limited by high recombination rate, short diffusion length of holes and carrier lifetime,

and low absorption capacity in the visible light region due to the indirect d-d transition [32, 33]. Similarly, as in the case of TiO_2, attention has been paid to develop nanostructured hematite and investigate the influence of doping, and previous studies have shown enhanced photocatalytic activity of α-Fe_2O_3 by those methods [19, 33].

Hematite has been employed to numerous applications of photocatalysis. In water treatment applications, for example degradation of dyes, such as Rhodamine B [19], α-Fe_2O_3 but especially the modified α-Fe_2O_3 with Ti and Ag nanoparticles have shown an excellent photocatalytic activity. Each of those three samples showed higher photocatalytic activity than pure TiO_2 toward the degradation of Rhodamine B. α-Fe_2O_3 has also been proposed for air purification applications, such as removal of NO_x gases [34]. The particular study gave more confirmation of the low photocatalytic performance of pure α-Fe_2O_3 but by the additional incorporation of carbon content the efficiency of α-Fe_2O_3 in the removal process was clearly enhanced.

In addition to these, α-Fe_2O_3 has been considered as a potential photoanode material for photoelectrochemical applications. For the water splitting that can be achieved by photocatalysis to be spontaneous, the conduction band position of semiconductor photoelectrode is required to be above the reduction potential of water (H^+/H_2O) and the valence band position below the oxidation potential (O^{2-}/H_2O). For example TiO_2 fulfills these requirements but due to the large band gap energy it is sensitive only to a very small portion of solar spectrum. Therefore, pure TiO_2 is not particularly suitable for the solar water splitting and the hydrogen production. α-Fe_2O_3 can be used as a photoelectrode material due to the appropriate band gap and, besides, its valence band position that locates below the oxidation potential of water. That makes it suitable for water oxidation. As a drawback, the conduction band edge of α-Fe_2O_3 is below the reduction potential, meaning the water reduction is not possible without an applied external bias voltage. α-Fe_2O_3 has been combined for example with NiO p-type semiconductor to induce p-type conduction [35]. As a result of the combination the conduction band of both α-Fe_2O_3 and NiO located above the reduction potential of water, making possible the photogenerated electrons to drive to oxygen reduction reaction.

The use of a cocatalyst as a modifier of semiconductor photocatalysts has been recognized to be an effective method to improve their photocatalytic performance. This method was utilized in the previous example of combining α-Fe_2O_3 with NiO via electrochemical deposition process. The cocatalyst could change the optical properties of the photocatalyst, suppress the recombination rate and provide active sites for oxidation and reduction. TiO_2 as well as α-Fe_2O_3 have been doped with metals and non-metals but also a combination with another semiconductor has been proposed. α-Fe_2O_3 is a promising candidate for acting as a cocatalyst, again due to the favourable band gap, and several experimental studies have reported improved photocatalytic performance by combining TiO_2 with α-Fe_2O_3. They have reported α-Fe_2O_3 to enhance the visible light absorption of TiO_2 by lowering the band gap energy [36, 37]. This enables photoactivations to be induced also by longer visible light wavelengths.

In addition, the interaction between TiO_2 and α-Fe_2O_3 has been observed to lead to a formation of a heterojunction that could provide separation of the photogenerated electrons and holes and thus, promote charge transfer and inhibit the recombination of the photogenerated charge carriers [8, 36, 37, 38, 39, 40]. However, it is observed that the Fe^{3+} may change to recombination center for the photogenerated e-h pair, leading to reduction

in photocatalytic activity when Fe concentration becomes larger [36, 40]. The optimal Fe concentration in TiO_2 photocatalyst, that improves the photocatalytic performance of TiO_2, has been reported to be fairly low [8, 40]. It is widely recognized experimentally but also theoretically that a dopant or a codopant modifies the band structure of the photocatalyst and could induce dopant states that can promote the visible light harvesting of the photocatalyst and decrease the recombination rate, also in the case of TiO_2 and α-Fe_2O_3 [41]. Specific surface area is also known to be a crucial parameter affecting the photocatalytic activity. The larger surface area provides more available active sites for redox reactions which can lead to higher photocatalytic activity. In the previous study performed by Lee *et. al.* [8] the lower surface area of Fe_2O_3/TiO_2 nanocomposite prepared by the impregnation method was observed to lead to lower activity. Although the sample was observed to have better charge transfer and lower recombination rate, the surface area had a dominant factor determining its photocatalytic activity. They further specified the used method to be the reason for the lower activity, not the addition of Fe_2O_3.

Different photocatalytic mechanisms for the combined system of TiO_2 and α-Fe_2O_3 have been proposed based on the aforementioned results. Generally, α-Fe_2O_3 has been reported to expand the light harvesting of TiO_2 to the visible light range and suppress the recombination rate of TiO_2. The formation of a heterojunction has be proposed to be the main feature behind the enhanced performance. Both type I and type II heterojunctions have been proposed to be formed [38, 39, 41]. However, only a few theoretical studies have been performed to complete and refine the results from experimental studies and further fully understand the mechanism behind the photocatalytic process in the combined system of TiO_2 and α-Fe_2O_3. In general, the understanding of the photocatalytic mechanism would promote creation of better and more efficient photocatalysts. The currently existing photocatalysts are not efficient enough for the practical applications. To achieve the sufficient efficiency many challenges related to their performance must be overcome.

1.4 Cluster photocatalysts

The research of nano-structured semiconductors as photocatalysts has been growing during past decades. Several published articles have reported superior photocatalytic performance of nano-structured catalysts. There is also the effect of the different types of nanostructures to the photocatalytic activity, whether for example the catalyst is in the form of nanoparticles or nanosheets [42]. In addition, studies have shown that photocatalytic activity may be improved by introducing a nano-structured material as cocatalyst [19]. Despite the successfulness of the nanophotocatalysts, challenges have also been observed in their use. One of the observed problems of nanoparticles is aggregation. Due to the dangling bonds and high surface energy the aggregation of nanoparticles tends to occur to be able to lower their energy. A reduced photocatalytic performance has been reported due to the aggregation of nanoparticles but the size and the structure of the aggregate seems to play an important role on that [43]. As the aggregate become a larger the generation of reactive oxygen species reduces. But smaller size aggregates could be considered as a candidate to enhance the performance of photocatalysts. A small aggregate is called a cluster.

Commonly, a cluster is considered as an aggregate of small and finite number of constituents that form an intermediate stage between an atom and a solid, based on its unique properties. It can be made of identical atoms which is called a homo-atomic cluster or, on

the other hand, it can composed of two or more elements which called then a hetero-atomic cluster. Hematite, α-Fe_2O_3 clusters are hetero-atomic with covalent bonding. The unique properties, such as electronic and magnetic properties, result from the fact that a substantial fraction of atoms of the cluster locate at the surface. The properties can be tuned by varying the size, shape and composition of the cluster. The addition or removal of even a single atom can significantly change the properties of the clusters, especially of the small, nanoscale clusters, as they are usually dominated by the quantum effects, and geometry effects which relate to the magic size of clusters. An illustrative example could be given of mercury. Mercury clusters as a function of sizes have been first studied both theoretically by Pastor *et. al.* [44]. Small mercury clusters are insulators due to the large band gap. Generally, band gap of clusters are larger than bulks that can be explained by smaller number of atoms and hence, the smaller number of overlapping orbitals. Thus the width of the bands decrease and the gap between valence and conduction band increases. However, increasing the cluster size the band gap decreases and at a specific cluster size mercury undergo a metal-insulator phase transition. This was experimentally confirmed by Kaiser and Rademann [45]. This also shows that as the size of the cluster increases, clusters starts to mimic the bulk material. Bulk mercury is well-known to be metallic. Besides, as size of a cluster increases, quantum effects become less prominent and eventually the classical theories can be used to describe clusters. However, how many atoms the cluster is required to contain to show bulk-behaviour is still an interesting and open research question.

A large number of surface atoms leads to high surface-to-volume ratio of clusters which has been observed to be a substantial parameter affecting the photocatalytic activity. The higher surface area provides more active sites for the photocatalytic reaction, increasing its rate. Moreover, due to the dangling bonds, surface atoms have a larger surface energy and thus, they are more unstable. These factors are primary reasons that clusters have high reactivity compared to bulk. It is interesting that even if the bulk state of an element is chemically inert, in small clusters it can become highly reactive. Gold is a good example of this [46]. The advantageous properties of clusters have attracted attention and the study of utilizing clusters in a photocatalysis has been grown. As in the case of nanoparticles, the agglomeration of the clusters is also a negative effect for the photocatalytic process. It usually leads to poor morphology and reduction in photocatalytic activity [47]. To control the growth of the cluster size and their agglomeration a support material, generally a semiconductor photocatalyst, such as TiO_2, is used for the stabilization of the clusters [40, 48]. In practice, this means that a cluster is adsorbed on the surface of a support material. So rather than investigating only the cluster, it can be considered as a cocatalyst of the support material. The study thus focuses on the combined system formed by the cluster and the support material and the investigation of the effects of the cluster to the photocatalytic properties of the support material. As already mentioned, pure photocatalysts usually have a poor photocatalytic performance, and the main goal of attaching the cluster to the support material is to enhance the photocatalytic performance of the support material.

1.5 Focus of the thesis

In this work, using density functional theory based calculations we study anatase TiO_2 (101) surface on which we attach α-Fe_2O_3 clusters. Transition metals, such as Fe, have tendency, when doped to TiO_2, to diffuse to the surface and form iron oxide clusters. This

emphasized us in the choice of hematite in a cluster form. We investigate two different cluster sizes in this thesis: the smallest and the second smallest α-Fe_2O_3 clusters. The aim of the theoretical studies is to gain better understanding of the photocatalytic mechanism in the created combined systems. Previously, Sun *et al.* have experimentally studied anatase TiO_2 surface on which they attached a Fe_2O_3 cluster. The photocatalytic activity of the created combined system was studied experimentally for the degradation of phenol [40]. They observed that a small cluster can enhance the photocatalytic performance of TiO_2 while a large one can hinder it. The increment of the concentration was also observed to lower the photocatalytic activity of TiO_2. The earlier DFT study of the particular combined system showed the formation of a type I heterojunction with straddling gap which was proposed to be responsible for the improved photocatalytic performance [41].

In addition to that, we study the effect of oxygen vacancy in the combined system of TiO_2 surface and the smallest α-Fe_2O_3 cluster. In the recently published report, the oxygen vacancy was found to be energetically less favourable than interstitial hydrogen vacancy at the TiO_2-Fe_2O_3 heterostructure [49] but more systematic study of the effect of oxygen vacancy on the photocatalytic mechanism was not performed. Besides, we found no other studies of the oxygen vacancy in the combined system of TiO_2 and Fe_2O_3. As a defect, oxygen vacancy can affect properties of photocatalysts and therefore we decided to investigate it. By introducing several different vacancy sites we tried to elucidate the favourable location of the vacancy and their effect on the photocatalytic mechanism compared to the defect-free combined system.

We began this thesis by introducing photocatalysis, hematite (α-Fe_2O_3) and its usage in photocatalytic applications. Section 2 is devoted to the theoretical formulation of density functional theory that forms the basis for the computational processing while the following Section 3 represents the basics of the simulation of solids and crystalline materials and the implementation of the density functional theory in practice. In Section 4 we introduce the details of the calculations that are used in this work. Sections 5, 6, 7 and 8 represent then the results obtained from the calculations. The final section summarizes the results and conclusions.

2 Computational method

Density functional theory (DFT) is a theoretical approach for solving correlated many-body problems. Instead of approximating the many-body wave function of N interacting electrons, as Hartree-Fock theory does, DFT expresses the many-body problem in terms of electron density. While the wave function is a function of $3N$ spatial variables and of N spin variables the electron density is only a function of three spatial variables, x, y and z, and thus independent of the number of electrons. This makes DFT computationally feasible also for large systems. It has become a widely used tool for the calculation of electronic structure of atoms, molecules and solids, and material properties in condensed matter physics. The aim of this chapter is to represent the theoretical background of density functional theory.

2.1 Many-body Shrödinger equation

In quantum mechanics a system is described by a wave function which is obtained by solving the Schrödinger equation. Because atoms consist of nuclei and electrons the locations of them both are needed for solving the Schrödinger equation. The problem can be simplified because of the different dynamics of electrons and nuclei. Nuclei are much heavier than electrons, and based on that fact the electronic and nuclear motion can be treated separately. This separation is known as Born-Oppenheimer approximation in which nuclei are held fixed in space, and electrons are moving inside the potential caused by nuclei and responding to changes in the nuclear positions immediately. The problem reduces to solving the Schrödinger equation for an N-electron system, and in the time-independent case, the Schrödinger equation is

$$\hat{H}\left|\Psi\right\rangle = E\left|\Psi\right\rangle, \tag{2.1}$$

where $\hat{H}$ is the Hamiltonian, $\left|\Psi\right\rangle = \left|\Psi(\vec{r}_1, \ldots, \vec{r}_N)\right\rangle$ is the N-electron wave function and E is the electronic energy of the system. More specifically, the Hamiltonian of a many-electron system consists of a kinetic energy operator $\hat{T}$ and potential operator $\hat{V}$. The potential includes the electron-electron interaction $\hat{V_{ee}}$ and the Coulomb interaction between electrons and nuclei $\hat{V_{\text{ext}}}$. Thus, the general form of the Hamiltonian is

$$\begin{aligned}\hat{H} &= \hat{T} + \hat{V}_{ee} + \hat{V}_{\text{ext}} \\ &= \sum_i^N -\frac{\hbar}{2m}\nabla_i^2 + \frac{1}{2}\sum_{i\neq j}\frac{e^2}{|\vec{r}_i - \vec{r}_j|} + \sum_i^N \frac{Z_k}{|\vec{r}_i - \vec{r}_k|}.\end{aligned} \tag{2.2}$$

Here Z_k are the nuclear charges.

Especially, the ground state of the system is of great interest [50]. The energy of the system, which is a functional of the wave function, is obtained as the expectation value of the Hamiltonian

$$E[\psi] = \left\langle\Psi\right|\hat{H}\left|\Psi\right\rangle. \tag{2.3}$$

The variational principle states that the minimization of the energy functional $E[\psi]$ with respect to the N-electron wave function gives the ground state wave function $\left|\Psi_0\right\rangle$ and the ground state energy E_0. In addition to $\left|\Psi_0\right\rangle$ and E_0, the principle can also be used to determine other ground state properties, such as the ground state electron density. The electron density $n(\vec{r})$, probability of finding an electron at a specific location, is obtained by

integrating the N-electron wave function $|\psi\rangle$. During the integration one electron is held in certain position and integration goes over all other positions. The formula of the electron density is

$$n(\vec{r}) = N \int d\vec{r}_2 \int d\vec{r}_3 \ldots \int d\vec{r}_N |\Psi(\vec{r}_1, \ldots, \vec{r}_N)|^2. \tag{2.4}$$

By integrating $n(\vec{r})$ over the space, one obtains the total number of electrons N,

$$N = \int n(\vec{r}) d\vec{r}. \tag{2.5}$$

2.2 Thomas-Fermi Model

Although the wave function is the central quantity to describe quantum mechanical systems, it is also the one that causes problems in solving the Shrödinger equation. The dependence on 3N spatial variables makes wave function very complicated, even within the Born-Oppenheimer approximation. Therefore, there exists no analytical solution for many-body problems. The Shrödinger equation has been managed to solve analytically only for a small number of electrons. Finding an exact solution for a three-body system is already a hard task, even computationally. As the number of electrons N increases the computational cost increases exponentially, and it becomes computationally impractical, if not impossible to perform such calculations.

Already in 1972 Thomas and Fermi [50] proposed the first attempt to calculate the total energy by replacing the wave function by electron density $n(\vec{r})$, a much simpler quantity that depends only on three spatial variables. Their work, known as Thomas-Fermi model, approaches electrons in a semi-classical way. Electron-electron and Coulomb interactions are treated classically but the kinetic energy of the electrons is treated quantum mechanically, and its expression based on the non-interacting homogeneous electron gas (HEG) model. The kinetic energy of the homogeneous electron gas is

$$T_{TF} = \frac{3}{10}(3\pi^2)^{2/3} \int n(\vec{r})^{5/3} d\vec{r}. \tag{2.6}$$

However, the approximations that are made in the derivation of the model are too crude. In addition, the model neglects the contributions of exchange and correlation effects to the total energy. Thus, it does not provide the accuracy needed in nowadays electronic structure calculations. But in the model, the total energy was written completely in terms of the electron density for the first time. This created the basis for the development of the density functional theory.

2.3 Hohenberg-Kohn theorem

Hohenberg-Kohn (HK) theorem form a theoretical basis for the formulation of density functional theory. The theorem states that the electron density can be considered as a basic variable, similarly as the wave function. All the observables of the system, such as energy, can be written as a functional of the electron density and are thus uniquely determined in terms of it. The theorem consists of two parts, known as the 1st and 2nd theorems, that formulate DFT as an exact theory of many-body systems [50].

The first HK theorem states that the wave function leads to unique electron density which further uniquely determines the external potential, besides an additive constant [50]. The proof of the theorem is based on utilizing the variational principle and finding the contradiction.

Assume that there exist two different external potentials, V_{ext} and V'_{ext} differing more than a constant from each other. These two different potentials will lead to two different Hamiltonians, $\hat{H}$ and $\hat{H}'$. By solving the Schrödinger equation of the Hamiltonians two different ground state wave functions, $|\psi\rangle$ and $|\psi'\rangle$, and ground state energies, E_0 and E'_0, are obtained.

However, let's assume that wave functions $|\psi\rangle$ and $|\psi'\rangle$ produce the same ground state electron density $n_0(\vec{r})$. If $|\psi'\rangle$ is taken as a trial function for $\hat{H}$, according to the variational principle we obtain

$$E_0 < \langle\psi'|\,\hat{H}\,|\psi'\rangle = \langle\psi'|\,\hat{H}'\,|\psi'\rangle + \langle\psi'|\,\hat{H}-\hat{H}'\,|\psi'\rangle = E'_0 + \langle\psi'|\,V_{\text{ext}} - V'_{\text{ext}}\,|\psi'\rangle\,. \tag{2.7}$$

Because $|\psi'\rangle$ is not a true ground state wave function of $\hat{H}$ the obtained energy will always be greater that the true ground state energy. Similarly for E'_0, if $|\psi\rangle$ is now used as a trial function,

$$E'_0 < \langle\psi|\,\hat{H}'\,|\psi\rangle = \langle\psi|\,\hat{H}\,|\psi\rangle + \langle\psi|\,\hat{H}'-\hat{H}\,|\psi\rangle = E_0 + \langle\psi|\,V'_{\text{ext}} - V_{\text{ext}}\,|\psi\rangle\,. \tag{2.8}$$

After adding these two equations, we get a clear contradiction,

$$E_0 + E'_0 < E'_0 + E_0. \tag{2.9}$$

In other words, $0 < 0$ which is impossible. This proves that the ground state electron density uniquely determines the external potential because there cannot exist two different V_{ext} that would yield the same electron density. In other words, there exists a unique mapping between $n(\vec{r})$ and $V_{\text{ext}}(\vec{r})$, i.e $n(\vec{r}) \Leftrightarrow V_{\text{ext}}(\vec{r})$.

In addition, the density also determines the number of electrons N (in Eq.(2.5)). Therefore, the Hamiltonian (Eq.(2.2)), which is defined by N and V_{ext}, and further the wave function are determined by the electron density [50]. Thus, the ground state electron density determines all ground state properties of the N-electron system. Based on this proof, the total energy can be written as a functional of the density, $E = E[n]$, and the equation (2.2) can be rewritten as

$$E[n] = T[n] + V_{ee}[n] + V_{\text{ext}}[n]. \tag{2.10}$$

The second HK theorem provides that the ground state energy is obtained by utilizing the variational principle. Energy functional, $E[n]$, gives the exact ground state energy when it reaches the global minimum. The electron density that minimizes the $E[n]$ functional corresponds to the exact ground state electron density $n_0(\vec{r})$. According to the first HK theorem, the ground state density $n_0(\vec{r})$ corresponds to the ground state wave function $|\psi_0\rangle$. A different wave function $|\psi\rangle$ cannot yield the same electron density as $|\psi_0\rangle$. The variational principle immediately states that

$$E_0 = \langle\psi_0|\,\hat{H}_0\,|\psi_0\rangle < \langle\psi|\,\hat{H}\,|\psi\rangle = E. \tag{2.11}$$

A different electron density than the ground state density will always give a higher energy than the ground state energy. This is valid for any external potential V_{ext}. The second

theorem is analogous to the variational principle of the wave function. By minimizing the energy functional with respect to the electron density $n(\vec{r})$, the total energy of the ground state is found. One should notice that during minimization the density must fulfill the equation (2.5).

It is important to notice that the represented HK theorem is the original one which applies under certain conditions. Firstly, based on the theorem DFT is a ground state theory [51]. It is formulated for ground state with constant number of electrons N. It does not apply to excited states in this form but there exist number of extensions for Kohn-Sham theory (introduced in the next Section), which enable the access to excited states and their properties. One of the approaches is the time-dependent density functional theory (TD-DFT) [50, 52].

Another observation is that the theorem is formulated for a non-degenerate ground state. However, degenerate ground states exists also and in those cases, the electron density does not uniquely determine the external potential any longer. But it has been proved later that the HK theorem still holds in the presence of degeneracy. In the case of a degenerate ground state, the ground state electron density uniquely determines the manifold of the degenerate states, and each of these degenerate states still uniquely determines the external potential [53]. Thus, the mapping $n(\vec{r}) \Leftrightarrow V_{\text{ext}}(\vec{r})$ proved by the 1st HK theorem is still valid.

Although the HK theorem proves the replacement of the wave function by the electron density and the existence of the total energy functional (2.10) it does not provide any method for finding such a functional. Kohn and Sham introduced their approach in 1965 [50] to find the universal energy functional which turned DFT into a practical electronic structure theory.

2.4 Self-consistent Kohn-Sham equations

Kohn and Sham (KS) proposed a replacement of the real and interacting system by a virtual system of non-interacting electrons which generates the same electron density as the original interacting system. The Kohn-Sham wave function of the non-interacting system is approximated by Slater determinant,

$$\Psi_{KS}(\vec{r}_1, \vec{r}_2, \cdots, \vec{r}_N) = \frac{1}{\sqrt{N!}} \begin{vmatrix} \chi_1^{KS}(1) & \chi_2^{KS}(1) & \cdots & \chi_N^{KS}(1) \\ \chi_1^{KS}(2) & \chi_2^{KS}(2) & \cdots & \chi_N^{KS}(2) \\ \vdots & \vdots & \ddots & \vdots \\ \chi_1^{KS}(N) & \chi_2^{KS}(N) & \cdots & \chi_N^{KS}(N) \end{vmatrix}, \tag{2.12}$$

where χ_n^{KS} are the KS one-electron orbitals. As the electrons are non-interacting in the virtual system, N Schrödinger equations can be written for the one-electron orbitals χ_n^{KS},

$$\hat{h}^{KS}\chi_n^{KS}(\vec{r}) = \left[-\frac{\hbar^2}{2m}\nabla^2 + \hat{V}_s(\vec{r})\right]\chi_n^{KS}(\vec{r}) = \epsilon_i \chi_n^{KS}(\vec{r}), \qquad n = 1, \ldots, N \tag{2.13}$$

with the effective single-particle Hamiltonian $\hat{h}^{KS}$ and potential $v_s(\vec{r})$. The total external potential affecting the virtual system is denoted by an effective potential $V_s(\vec{r}) = \sum_{n=1}^{N} v_s(\vec{r}_n)$. ϵ_i are the KS eigenvalues. The electron density for the non-interacting system is given by

$$n_s(\vec{r}) = \sum_{i=1}^{N} \left|\chi_n^{KS}(\vec{r})\right|^2, \tag{2.14}$$

which produces the true ground state density, $n_s(\vec{r}) = n(\vec{r})$. The basic idea is to construct the potential $V_s(\vec{r})$ in such a way that the produced electron density of KS orbitals equals to the density of the interacting system.

The total energy of the KS virtual system is

$$E[n] = \langle \Psi_{KS}[n] | \hat{T} + \hat{V}_{ee} + \hat{V}_{\text{ext}} | \Psi_{KS}[n] \rangle = T[n] + E_H[n] + E_{\text{ext}}[n]. \tag{2.15}$$

The potential energy functional is known explicitly and can be written in terms of ground state electron density,

$$E_{\text{ext}}[n] = \int V_{\text{ext}}(\vec{r}) n_0(\vec{r}) d\vec{r}. \tag{2.16}$$

The given V_{ext} is the external potential of the system of non-interacting electrons.

The kinetic energy functional is divided into two parts: $T[n] = T_s[n] + T_r[n]$. $T_s[n]$ is the kinetic energy of the non-interacting system and $T_r[n]$ is a remainder which is usually rather small. Therefore, it is often neglected and $T_s[n]$ is approximated to be the exact kinetic energy functional.

Because the equations (2.13) and (2.14) provide access to the KS orbitals χ_n^{KS} besides the density, the kinetic energy of the Thomas-Fermi Model can be improved and expressed in a well-defined form,

$$T_s[n] = -\frac{\hbar^2}{2m} \sum_i^N \left\langle \chi_n^{KS} \right| \nabla^2 \left| \chi_n^{KS} \right\rangle. \tag{2.17}$$

The classical electron-electron electrostatic interaction energy (Hartree energy) $E_H[n]$ is given by

$$E_H[n] = \frac{1}{2} \int \int \frac{n(\vec{r}) n(\vec{r}')}{|\vec{r} - \vec{r}'|} d\vec{r} d\vec{r}'. \tag{2.18}$$

from Thomas-Fermi model [50].

To correct the kinetic energy approximation and cover the effect beyond the non-interacting system, such as exchange and correlation effects, a exchange-correlation functional E_{xc} is introduced and defined by

$$E_{\text{xc}} = T[n] - T_s[n] + E_{ee}[n] + E_H[n] \tag{2.19}$$

where $T[n]$ and E_{ee} are the true kinetic energy and electron-electron energy functional of the real interacting system. However, the exact form of E_{xc} is unknown and has to be approximated.

Thus, the exact total energy functional (2.15) for the interacting system can be rewritten as

$$\begin{aligned} E[n] &= T_s[n] + E_H[n] + E_{\text{ext}}[n] + E_{\text{xc}} \\ &= T_s[n] + E_H[n] + \int V_{ext}(\vec{r}) n_0(\vec{r}) d\vec{r} + E_{\text{xc}} \end{aligned} \tag{2.20}$$

The ground state energy of the system is obtained by minimizing the above total energy equation with respect to the electron density. The variational equation of the total energy functional is

$$\frac{\delta E[n]}{\delta n(\vec{r})} = \frac{\delta T_s[n]}{\delta n(\vec{r})} + \frac{\delta E_H[n]}{\delta n(\vec{r})} + V_{\text{ext}}(\vec{r}) + \frac{\delta E_{\text{xc}}[n]}{\delta n(\vec{r})}, \tag{2.21}$$

from which we can derive the effective potential

$$V_s(\vec{r}) = V_H(\vec{r}) + V_{\text{ext}}(\vec{r}) + V_{\text{xc}}(\vec{r}) \tag{2.22}$$

with exchange-correlation potential

$$V_{\text{xc}}([n],\vec{r}) = \frac{\delta E_{\text{xc}}[n]}{\delta n(\vec{r})}. \tag{2.23}$$

If $V_s(\vec{r})$ satisfies the equation (2.22), the electron densities of the real and the virtual systems are the same. Thus, the ground state energy and density of the interacting system can be computed alternatively from the Kohn-Sham equations (2.13) and (2.14), instead of minimizing $E[n]$ directly.

Because V_{ext} depends on $n(\vec{r})$ and further on the KS orbitals χ_n^{KS} the KS equations have to be solved iteratively by self-consistent field (SCF). The procedure starts with an initial guess $n^{(0)}$ for the density. The one-electron Hamiltonian $\hat{h}^{KS}$ and further KS equations (2.13) are solved with $n^{(0)}$. A New set of KS orbitals is obtained which is then used to produce a new trial density according to Eq. (2.14). The particular cycle is repeated until the convergence criterion for the total energy is achieved.

2.5 Exchange correlation energy functional

As a theory, DFT is exact. However, as mentioned, the exchange-correlation functional, E_{xc}, needed for determining the exact total energy and electron density, is unknown and has to be approximated. Therefore, the accuracy and the quality of the predictions of DFT largely depends on the approximation to the E_{xc} energy functional. There exist several approximations for the functional. Two most used approximation, local density and generalized gradient approximations, are described below. In addition to them, we introduced meta-GGA functionals, and the SCAN functional, which are thought as extension of the generalized gradient approximation.

2.5.1 Local density approximation

The local density approximation (LDA) is the first and the simplest approximation to the exchange-correlation functional $E_{\text{xc}}[n]$ introduced by Kohn and Sham [50]. As in the Thomas-Fermi-model, it utilizes the homogeneous electron gas model.

In LDA the electron density of the system at each point in space is approximated to be locally homogeneous. Within this approximation the exchange-correlation functional is written as

$$E_{\text{XC}}^{\text{LDA}}[n] = \int n(\vec{r})\epsilon_{\text{XC}}^{\text{HEG}}(n(\vec{r}))d\vec{r} \tag{2.24}$$

where $\epsilon_{\text{XC}}^{\text{HEG}}$ is the exchange-correlation energy per electron in a homogeneous electron gas with the density n. $\epsilon_{\text{XC}}^{\text{HEG}}$ is obtained by summing the exchange $\epsilon_{\text{X}}^{\text{HEG}}$ and correlation $\epsilon_{\text{C}}^{\text{HEG}}$ parts. The exchange energy is known exactly [50]

$$\epsilon_{\text{X}}^{\text{HEG}} = -\frac{3}{4} \cdot \left(\frac{3}{\pi}\right)^{1/3} \int n(\vec{r})^{4/3} d\vec{r} \tag{2.25}$$

but correlation energy is not. However, very accurate approximation for it is obtained from quantum Monte Carlo simulations of Ceperley and Alder [51, 54].

LDA is formulated for unpolarized systems. More general expression for it is a local spin density approximation (LSDA) which takes spin-polarization into account. In LSDA the exchange-correlation functional is a functional of the spin up and spin down electron densities $n_\uparrow(\vec{r})$ and $n_\downarrow(\vec{r})$,

$$E_{\mathrm{XC}}^{\mathrm{LSDA}} = \int n(\vec{r})\epsilon_{\mathrm{XC}}^{\mathrm{HEG}}(n_\uparrow(\vec{r}), n_\downarrow(\vec{r}))d\vec{r}, \tag{2.26}$$

where

$$n(\vec{r}) = n_\downarrow(\vec{r}) + n_\uparrow(\vec{r}). \tag{2.27}$$

LDA works well for systems in which the electron density varies slowly, especially for metals which are rather uniform systems. Success of the LDA can be explained by systematic error cancellation of exchange and correlation energies and by introducing an exchange-correlation hole [50].

In spite of the reasonable good performance in certain cases, there exist also features in which the LDA is known to fail. The well-known problem of the LDA is the overestimation of the binding energy of the molecules and cohesive energy of the solids [51]. Although the geometry of the system, such as lattice constant and bond length, is generally well predicted for metals and insulators they are usually still underestimated a little due to the over-binding problem. The underestimation is not extremely large, usually within few percent from the experimental value [51]. Another problem with the LDA arises in the case of weakly bonded systems. The approximation takes hydrogen bonds poorly into account and Van der Waals bonds are completely missing in practice.

2.5.2 Generalized gradient approximation

More often, real systems have more inhomogeneous electron density. In those cases, the electron density varies more rapidly and the LDA is incapable to describe it with the needed accuracy. To improve the accuracy of E_{XC}, various generalized gradient approximation (GGA) functionals have been developed. While the LDA depends only on the scalar density at each point, to describe the higher variations of the electron density the GGA includes a gradient of the density, $\nabla n(\vec{r})$, in the definition of the exchange-correlation functional. The generalized form of such a functional is

$$E_{\mathrm{XC}}^{\mathrm{GGA}} = \int n(\vec{r})\epsilon_{\mathrm{X}}^{\mathrm{HEG}}(n(\vec{r}))F_{\mathrm{XC}}(n(\vec{r}),\nabla n(\vec{r}))d\vec{r} \tag{2.28}$$

where F_{XC} is the exchange enhancement factor and $\epsilon_{\mathrm{X}}^{\mathrm{HEG}}$ is the exchange energy of homogeneous electron gas defined in equation (2.25). Numerous forms for F_{XC} exist [50] among which one of the most commonly used GGA functional is the Perdew-Burke-Ernzerhof (PBE) [55].

The PBE exchange-correlation functional is a sum of exchange and correlation functionals. In spin polarized case the form of the PBE exchange part is written as

$$E_{\mathrm{C}}^{\mathrm{PBE}}[n_\uparrow, n_\downarrow] = \int n[\epsilon_{\mathrm{XC}}^{\mathrm{HEG}}(r_s, \zeta) + H(r_s, \zeta, t)]d\vec{r} \tag{2.29}$$

where r_s is the local Wigner-Seitz radius and ζ is the spin polarization. t is a dimensionless density gradient given by

$$t = \frac{|\nabla n|}{2\phi k_s n} \tag{2.30}$$

that depends on the Thomas-Fermi screening wave number k_s and the spin-scaling factor

$$\phi = \frac{[(1+\zeta)^{2/3} + (1-\zeta)^{2/3}]}{2}. \tag{2.31}$$

The function H is a gradient contribution that is desired to satisfy three conditions. In the slowly varying limit, $t \to 0$, H is given by its second order gradient expansion

$$H \to \frac{e^2}{a_0}\beta\phi^3 t^2, \tag{2.32}$$

where $\beta = 0.066725$, while in the rapidly varying limit, $t \to \infty$,

$$H \to -\epsilon_{\mathrm{C}}^{\mathrm{HEG}}, \tag{2.33}$$

thus making the correlation energy vanish. In high density limit, the correlation energy scales to a constant and cancels the logarithmic singularity of $\epsilon_{\mathrm{C}}^{\mathrm{HEG}}$. In this limit,

$$H \to \frac{e^2}{a_0}\gamma\phi^3 \ln t^2, \tag{2.34}$$

where $\gamma = 0.031091$. All the three limits are satisfied by

$$H = \frac{e^2}{a_0}\gamma\phi^3 \ln\left(1 + \frac{\beta}{\gamma}t^2\frac{1+At^2}{1+At^2+A^2t^4}\right) \tag{2.35}$$

with function A,

$$A = \frac{\beta}{\gamma}\left[e^{\frac{-\epsilon_{\mathrm{C}}^{\mathrm{HEG}}}{\gamma\phi^3\frac{e^2}{a_0}}} - 1\right]^{-1}, \tag{2.36}$$

which is the final form of H in the PBE correlation function. [55]

With other four conditions the PBE exhange functional is constructed and defined by

$$E_{\mathrm{X}}^{\mathrm{PBE}}[n_\uparrow, n_\downarrow] = \int n\epsilon_{\mathrm{XC}}^{\mathrm{HEG}}(n)F_X(s)d\vec{r} \tag{2.37}$$

where the enhancement factor is

$$F_{\mathrm{XC}}^{\mathrm{PBE}}(s) = 1 + \kappa - \frac{\kappa}{1+\mu s^2/\kappa} \tag{2.38}$$

where $\kappa = 0.804$ [56], $\mu = \beta(\pi^2/3)$ and s is the dimensionless density gradient

$$s = \frac{|\nabla n(\vec{r})}{2k_F n(\vec{r})}. \tag{2.39}$$

One can see that when $F_{\mathrm{xc}}^{\mathrm{PBE}}$ approaches to 1 the GGA functional returns to LDA. As the name of F_{xc} implies the factor tells the enhanced exchange energy over the LDA. [55]

Compared to the LDA, in most cases the GGA improves geometries and binding energies [51]. Also hydrogen bonds are better accounted for GGA than in LDA but van der Waals bonds are still not reproduced. This is due to the semilocality of the GGA functionals. The GGA has been developed further and the made progress has led to meta-GGA functionals [57] that are coming next in Jacob's ladder after the GGA [58]. The meta-GGA goes beyond the GGA as it introduces an additional non-local parameter to approximate the exchange-correlation functional.

2.5.3 Meta-GGA

While the GGA includes the electron density and its first derivative in the exchange functional, the proposed meta-GGA functionals [59] try to improve the approximation of the E_{xc} by introducing a second derivative to the formulation of the functional. The general form of the meta-GGA functional is

$$E_{\mathrm{XC}}^{\mathrm{meta-GGA}}[n] = \int n(\vec{r})\epsilon_{\mathrm{XC}}(n(\vec{r}), \nabla n(\vec{r}), \tau(\vec{r}))d\vec{r} \tag{2.40}$$

where $n(\vec{r})$ is the electron density (2.14) and $\nabla n(\vec{r})$ is its gradient. A new parameter $\tau(\vec{r})$ is the non-interacting kinetic energy density of the occupied orbitals. In general, the kinetic energy density has the form of

$$\tau(\vec{r}) = \frac{1}{2}\sum_i |\psi_i(\vec{r})|^2 \tag{2.41}$$

but for orbitals of the KS system the expression is written as [57]

$$\tau(\vec{r}) = -\frac{1}{2}\sum_n \chi_n^{KS}(\vec{r})\nabla^2\chi_n^{KS}(\vec{r}). \tag{2.42}$$

The second derivative is added as a Laplacian into the meta-GGA formulation within DFT. The kinetic energy density is a non-local variable and thus, could provide more accurate results for electron densities of electrons around which there exists more localized exchange-correlation hole [50, 59]. Because the kinetic energy density is an additional input it increases the computational cost slightly.

Many meta-GGA functionals, for example TPSS [60], have been developed but a strongly constrained and appropriately normed (SCAN) functional [59] is the only one that satisfies the complete set of 17 known exact constraints that the functional is desired to satisfy and the exact DFT must fulfill. In addition, SCAN functional is appropriately normed. In the SCAN functional the exchange energy part brings the τ dependence. In the spin polarized case the exchange energy is [59]

$$E_{\mathrm{X}}[n] = \int n(\vec{r})\epsilon_{\mathrm{X}}^{\mathrm{HEG}}(n(\vec{r}))F_{\mathrm{X}}(s,\alpha)d\vec{r}, \tag{2.43}$$

where $\epsilon_{\mathrm{X}}^{\mathrm{HEG}}$ is the exchange energy of the homogeneous electron gas (Eq. (2.25)). $F_{\mathrm{X}}(s,\alpha)$ is the enhancement factor, similar to that of the PBE functional has, that depends on density gradient

$$s = \frac{|\nabla n|}{2(3\pi^2)^{1/3}n^{4/3}} \tag{2.44}$$

and in addition the variable

$$\alpha = \frac{\tau - \tau^w}{\tau^{\mathrm{HEG}}} > 0. \tag{2.45}$$

This α depends on the kinetic energy density τ. $\tau^w = |\nabla n|^2/8n$ is the single orbital limit of τ and

$$\tau^{\mathrm{HEG}} = \frac{3}{10}(3\pi^2)^{2/3} n^{5/3} \tag{2.46}$$

is the homogeneous density limit [59]. The SCAN functional has been tested for many systems and previous studies have shown it may provide improvement for example for the DFT results of semiconductors [61] and transition metals, such as iron oxide [62].

2.6 DFT+U

Although the GGA provides improvement to the LDA and generally yields better results, there is no systematic way to improve the exchange-correlation functional. Even though the gradient of the electron density are considered in addition to scalar density it has also its limitations to describe the systems.

Both the LDA and the GGA functionals are known to underestimate the band gap of semiconductors and insulators [64]. HK theorem stated DFT to be a ground state theory. Moreover, the eigenvalues of the KS equations have no physical meaning. After all, the eigenvalues are calculated for the virtual system, not for the real system, and therefore they fail in the description of the band gap. Both functionals are also known to fail in the description of strongly correlated materials, such as Mott insulators [65]. DFT tends to over-delocalize valence electrons due to the self-interaction error. The error appears because the self-interaction in the Coulomb part and that in the exchange part do not cancel each other completely. However, in transition metals the d and f states tend to be localized and more strongly interacting which is problematic for DFT. Their band gaps are generally underestimated but sometimes the LDA and the GGA functionals can predict even an incorrect metallic behaviour for them. There exist several methods to correct the error such as self-interaction correction (SIC), hybrid functionals and DFT+U method [50]. We represent the last mentioned method, DFT+U. Before getting into the topic we briefly introduce the Hubbard model.

The Hubbard model is one of the models to describe the strong Coulomb repulsion between localized electrons. The Hamiltonian of the Hubbard model in one dimensional case is [66]

$$\hat{H}_U = \sum_{\vec{R},\vec{R}',\sigma} t_{\vec{R},\vec{R}'} \hat{c}^\dagger_{\vec{R},\sigma} \hat{c}_{\vec{R}',\sigma} + U \sum_{\vec{R}} \hat{n}_{\vec{R},\uparrow} \hat{n}_{\vec{R},\downarrow}, \tag{2.47}$$

where $c^\dagger_{\vec{R}}$ and $c_{\vec{R}'}$ are creation and annihilation operators, and $n_{\vec{R},\sigma}$ is the number of electrons with spin σ in the orbital at site $\vec{R}$.

The first term in (2.47) is the kinetic energy, which describes the tunneling, the so called hopping process, between adjacent lattice sites. The kinetic energy is parameterized by the matrix element $t_{\vec{R},\vec{R}'} \equiv t$ which describes the hopping amplitude. The second term, the Coulomb potential, takes into account the on-site repulsion interaction. The particular Coulomb potential is described by Hubbard parameter U the magnitude of which tells the strength of the on-site repulsion which is multiplied by the sum of the product of occupation

numbers of atomic state on the same site. If two electrons occupying the same orbital have opposite spins the total energy is increased by on-site repulsion energy U.

The Hubbard model is used as an inspiration to the formulation of DFT+U. DFT+U takes the Hubbard term from the Hubbard model as a correction and adds it to the Hamiltonian of DFT to treat the on-site repulsion between localized electrons. The corrected approximation depends on which exchange-correlation functional is used and is usually labelled as LDA+U or GGA+U. In practice, the strength of the on-site interaction is described by two parameters: the on-site Coulomb term U and on-site exchange term J in DFT.

The total energy functional of DFT+U with an electron-electron interaction correction from Hubbard model has a form of [67]

$$\begin{aligned} E^{\mathrm{DFT+U}} &= E^{\mathrm{DFT}} + E_U \\ &= E^{\mathrm{DFT}} + E_{\mathrm{Hubbard}} + E_{dc}. \end{aligned} \tag{2.48}$$

The energy E^{DFT} is the total energy of standard DFT and the term E_U is the Hubbard correction consisting of two terms: E_{Hubbard} is the on-site Hubbard-like interaction energy term and E_{dc} known as a double counting term which is needed to subtract the double counted interactions contained in both E^{DFT} and E_{Hubbard}.

The rotationally invariant formulation introduced by Liechtenstein *et al.* [68] gives general expressions for E_{Hubbard} and E_{dc}. The Hubbard interaction is

$$\begin{aligned} E_{\mathrm{Hubbard}}[\{n^{\vec{R}}_{mm'}\}] =& \frac{1}{2} \sum_{\{m\},\sigma,\vec{R}} \{\langle mm''|\, V_{ee}\, |m'm'''\rangle\, n^{\vec{R}\sigma}_{mm'} n^{\vec{R}-\sigma}_{m''m'''} \\ &+ (\langle mm''|\, V_{ee}\, |m'm'''\rangle - \langle mm''|\, V_{ee}\, |m'''m'\rangle) n^{\vec{R}\sigma}_{mm'} n^{\vec{R}\sigma}_{m''m'''}\}, \end{aligned} \tag{2.49}$$

where $n^{\vec{R}\sigma}_{mm'}$ is the occupation matrix on site $\vec{R}$,

$$n^{\sigma}_{mm'} = \sum_{n\vec{k}} f^{\sigma}_{n\vec{k}}\, \langle \psi^{\sigma}_{n\vec{k}}|\, P_{mm'}\, |\psi^{\sigma}_{n\vec{k}}\rangle\,. \tag{2.50}$$

$\psi^{\sigma}_{n\vec{k}}$ are the Kohn-Sham orbitals χ^{KS} corresponding to the states $(n,\vec{k})$ with spin σ and $f_{n\vec{k}}$ is the corresponding occupation number. $P_{mm'}$ is the projector operator on the localized orbitals. The V_{ee} integral represents the electron-electron interaction and it can be represented in terms of spherical harmonics Y_{kq} and Slater integrals F^k,

$$\langle mm''|\, V_{ee}\, |m'm'''\rangle = \sum_{k=0}^{2l} a_k(m,m',m'',m''') F^k, \tag{2.51}$$

where

$$a_k(m,m',m'',m''') = \frac{4\pi}{2k+1} \sum_{q=-k}^{k} \langle lm|\, Y_{kq}\, |lm'\rangle\, \langle lm''|\, Y^*_{kq}\, |lm'''\rangle\,. \tag{2.52}$$

The quantum number l is the angular moment of localized electrons. The double counting term has a following form,

$$E_{dc}[\{n^{\vec{R}}\}] = \sum_{\vec{R}} \frac{U}{2} n^{\vec{R}}(n^{\vec{R}}-1) - \sum_{\vec{R}} \frac{J}{2}[n^{\vec{R}\uparrow}(n^{\vec{R}\uparrow}-1) + n^{\vec{R}\downarrow}(n^{\vec{R}\downarrow}-1), \tag{2.53}$$

where $n^{\vec{R}} = n^{\vec{R}\uparrow} + n^{\vec{R}\downarrow}$ and $n^{\vec{R}\sigma} = \mathrm{Tr}(n^{\vec{R}\sigma}_{mm'})$.

For d electrons only integrals F^0, F^2 and F^4 remain while for f electrons also F^6 [67]. U and J can be calculated using the above integral and thus, E_{Hubbard} can be expressed as a function of U and J,

$$U = \frac{1}{(2l+1)^2} \sum_{m,m'} \langle mm' | \, V_{ee} \, | mm' \rangle = F^0 \tag{2.54}$$

and

$$J = \frac{1}{2l(2l+1)} \sum_{m \neq m', m'} \langle mm' | \, V_{ee} \, | mm' \rangle = \frac{F^2 + F^4}{14}. \tag{2.55}$$

In Liechtenstein's formulation, parameters U and J are implemented separately. To simplify the U approach, in the scheme of Dudarev *et al.* [69] only the difference $U - J$ plays a crucial role. It is taken as an effective U_{eff} parameter that accounts for the on-site interaction. In Dudarev's approach the Hubbard correction is given by

$$\begin{aligned} E_U[\{n^{\vec{R}\sigma}_{mm'}\}] &= E_{\mathrm{Hubbard}}[\{n^{\vec{R}}_{mm'}\}] + E_{dc}[\{n^{\vec{R}}\}] \\ &= \frac{U_{eff}}{2} \sum_{\vec{R}} \left(\sum_{m,\sigma} n^{\sigma}_{mm} + \sum_{m,m',\sigma} n^{\sigma}_{mm'} n^{\sigma}_{m'm} \right), \end{aligned} \tag{2.56}$$

where $U_{eff} = U - J$. By diagonalising the occupation matrices the final form of the Hubbard correction is obtained,

$$E_U[\{n^{\vec{R}\sigma}_{mm'}\}] = \frac{U_{eff}}{2} \sum_{\vec{R},\sigma} \sum_{m} \lambda^{\vec{R},\sigma}_{m} (1 - \lambda^{\vec{R},\sigma}_{m}) \tag{2.57}$$

where $\lambda^{\vec{R},\sigma}_{m}$ are the eigenvalues of the diagonalized occupation matrix $n^{\vec{R}\sigma}_{mm'}$.

3 Practical implementation

3.1 Simulating crystalline materials

3.1.1 Crystal structure

Ideal crystalline materials are solids whose atomic structure is composed of atoms or molecules arranged in patterns forming a periodically repeating object. This is referred to as a basis. To form a crystal an infinite group of discrete points $\vec{R}$ in space i.e. a lattice has to be placed to the basis. The particular group of points is defined as [70]

$$\vec{R} = n_1\vec{a}_1 + n_2\vec{a}_2 + n_3\vec{a}_3, \tag{3.1}$$

where $\vec{a}_i$ are primitive vectors that determine the unit cell and n_i are integers. A group of points that fulfills the definition (3.1) is called Bravais lattice. In it the lattice, in any direction, looks exactly the same from every point of the Bravais lattice and thus, the crystal structure is symmetric with respect to any translation operations. The translation operation is generally defined by an operator $\hat{T}_{\vec{R}}$ that moves an arbitrary function $f(\vec{r})$ by the Bravais lattice vector,

$$\hat{T}_{\vec{R}} f(\vec{r}) = f(\vec{r} + \vec{R}). \tag{3.2}$$

The Bravais lattice has an infinite number of atoms and we can move in it from one site to another by translation operations. Of course in real life, crystals are finite. In computer simulations it is impractical to deal with the whole system as the number of atoms scales as $\mathcal{O}(10^{23})$. To make it more practical, a large and finite system can be reduced to a smaller part of it by introducing a periodic boundary condition. Usually, the study is restricted inside the unit cell of the crystal. In simulation it is called a simulation cell. By replicating the simulation cell we get an infinite number of the unit cells, called periodic images. The periodic images have the same dynamics and number and positions of the atoms. The crystal can be thought of as the same unit cell repeated over and over in all directions. If an atom goes out of the simulation cell, its periodic image is reintroduced immediately on the opposite side of the cell so there is always the same number of atoms in the simulation cell. This is visualized in Figure 2.

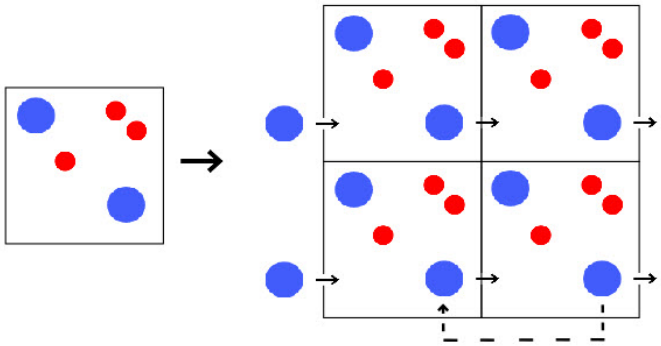

Figure 2: Visualization of the periodic boundary condition in two dimensions. The unit cell on the left is chosen to model the crystal which is then replicated in all directions. The periodic boundary condition between periodic images, seen on the right, ensures that if a blue atom crosses the boundary its periodic image appear on the opposite side of the cell.

3.1.2 Reciprocal lattice

Instead of operating in real space, by Fourier transferring the Bravais lattice the reciprocal lattice is obtained in reciprocal space. It is defined as a periodic set of wave vectors $\vec{K}$ which is called reciprocal lattice vector and are given by [70]

$$\vec{K} = m_1\vec{b}_1 + m_2\vec{b}_2 + m_3\vec{b}_3, \quad m_i \in \mathbb{Z}. \tag{3.3}$$

These vectors map points in the reciprocal space. The $\vec{b}_i$ are the primitive vectors of the reciprocal lattice defined as follows, [70]

$$\vec{b}_1 = 2\pi\frac{\vec{a}_2 \times \vec{a}_3}{\vec{a}_1 \cdot (\vec{a}_2 \times \vec{a}_3)}, \quad \vec{b}_2 = 2\pi\frac{\vec{a}_3 \times \vec{a}_1}{\vec{a}_1 \cdot (\vec{a}_2 \times \vec{a}_3)}, \quad \vec{b}_3 = 2\pi\frac{\vec{a}_1 \times \vec{a}_2}{\vec{a}_1 \cdot (\vec{a}_2 \times \vec{a}_3)}. \tag{3.4}$$

The denominator $\vec{a}_1 \cdot (\vec{a}_2 \times \vec{a}_3)$ gives the volume of the unit cell in real space.

As the Bravais lattice is invariant under translations the properties of the crystal, such as electron density, can be described by periodic functions. Let us take a periodic function $f(\vec{r})$ with period of $\vec{R}$. Thus, $f(\vec{r} + \vec{u}) = f(\vec{r})$. The periodic function can be expanded in Fourier series,

$$f(\vec{r}) = \sum_i f_i e^{i\vec{G}\cdot\vec{r}}, \tag{3.5}$$

where $\vec{G}$ is a vector in Fourier space, or in other words in reciprocal space, and f_i are the Fourier coefficients. Only the vectors $\vec{G}$ that are consistent with the periodicity of the Bravais lattice are included in the Fourier series. The periodicity $f(\vec{r}+\vec{u}) = f(\vec{r}+\vec{R}) = f(\vec{r})$ can now be expressed in terms of the Fourier series (3.5)

$$\begin{aligned} \sum_i f_i e^{i\vec{G}\cdot(\vec{r}+\vec{R})} &= \sum_i f_i e^{i\vec{G}\cdot\vec{r}} \\ \Rightarrow e^{i\vec{G}\cdot\vec{R}} &= 1, \end{aligned} \tag{3.6}$$

which holds when

$$\vec{G} \cdot \vec{R} = 2\pi l, \quad l \in \mathbb{Z}. \tag{3.7}$$

As for the vector $\vec{G}$ to belong to the reciprocal lattice it must fulfill the requirement (3.7). The vectors $\vec{G}$ that fulfill the above requirement form a set of reciprocal lattice points $\vec{K}$ that maps the points in the reciprocal lattice and the particular set of vectors $\vec{K}$ is called reciprocal lattice. The reciprocal lattice has the same periodicity as the Bravais lattice in real space. From the requirement (3.7) it follows that the primitive reciprocal lattice vectors $\vec{b}_i$ have the property

$$\vec{b}_i \cdot \vec{a}_j = 2\pi\delta_{ij}, \quad \delta_{ij} = \begin{cases} 1, & \text{if } i = j, \\ 0, & \text{if } i \neq j. \end{cases} \tag{3.8}$$

In the reciprocal space a Brillouin zone is defined as an unit cell of the reciprocal lattice. More precisely, the Brillouin zone is a Wigner-Seitz cell of the reciprocal lattice point which is a volume that encloses a set of points that are closer to the origin than to any other point. This is also called the first Brillouin zone [70]. The Brillouin zone can be constructed by enclosing the points by Bragg planes. From that we get an alternative definition for the 1st Brillouin zone: it is a set of points that can be reached from the origin without crossing

any Bragg planes. The nth Brillouin zone of the reciprocal lattice can be then defined as a set of points that can be reached from the origin by crossing $n-1$ Bragg planes. The Brillouin zones are needed to understand quantum mechanical, delocalized electrons whose eigenstates and eigenvalues are functions of wave vector $\vec{k}$ in reciprocal space, instead of position $\vec{r}$.

3.1.3 Bloch theorem

The electrons of the atoms do not move freely in crystals but in periodic potential $U(\vec{r})$ of nuclei. The Schrödinger equation of the non-interacting electron in a periodic potential is

$$\left[-\frac{\hbar^2}{2m}\nabla^2 + U(\vec{r})\right]\psi(\vec{r})_i = \epsilon_i\psi(\vec{r})_i, \quad i = 1,\ldots,N \tag{3.9}$$

with periodic property if the potential,

$$U(\vec{r}+\vec{R}) = U(\vec{r}), \tag{3.10}$$

where $\vec{R}$ is the Bravais lattice vector. Thus, the Hamiltonian is also periodic, $\hat{H}(\vec{r}+\vec{R}) = \hat{H}(\vec{r})$. Felix Bloch proposed a theorem that specifies the form of the wave function in a periodic potential [70]. According to the theorem the solutions of the Schrödinger equation (3.9) have the general form

$$\psi(\vec{r}) = e^{i\vec{k}\cdot\vec{r}}u(\vec{r}), \tag{3.11}$$

where $\vec{k}$ is the wave vector and $u(\vec{r})$ is the periodic Bloch function.

In order to specify the crystal system completely, all the operators commuting with the Hamiltonian of the system are desired to find. In a periodic potential only the translation operator $\hat{T}_{\vec{R}}$ (3.2) commutes with it,

$$\begin{aligned}\hat{T}_{\vec{R}}\hat{H}(\vec{r})\psi(\vec{r}) = \hat{H}(\vec{r}+\vec{R})\psi(\vec{r}+\vec{R}) = \hat{H}(\vec{r}+\vec{R})\psi(\vec{r}) = \hat{H}(\vec{r})\hat{T}_{\vec{R}}\psi(\vec{r})\\ \Rightarrow \hat{T}_{\vec{R}}\hat{H} = \hat{H}\hat{T}_{\vec{R}},\end{aligned} \tag{3.12}$$

where we used results form equations (3.2) and (3.10). Therefore, only two quantum numbers are needed to specify the states ψ of the system: band index n and Bloch's wave vector $\vec{k}$ for the Hamiltonian and for the translation operator. Because the Hamiltonian and $\hat{T}_{\vec{R}}$ commute they have common eigenstates,

$$\hat{H}\psi_{n\vec{k}}(\vec{r}) = \epsilon_i\psi_{n\vec{k}}(\vec{r}), \tag{3.13}$$

$$\hat{T}_{\vec{R}}\psi_{n\vec{k}}(\vec{r}) = \lambda_{\vec{R}}\psi_{n\vec{k}}(\vec{r}), \tag{3.14}$$

where $\lambda_{\vec{R}}$ are the eigenvalues of the translation operator $\hat{T}_{\vec{R}}$.

In addition to the Hamiltonian, the translation operator $\hat{T}_{\vec{R}}$ commutes with another translation operator $\hat{T}'_{\vec{R}}$,

$$\begin{aligned}\hat{T}_{\vec{R}'}\hat{T}_{\vec{R}}\psi(\vec{r}) = \hat{T}_{\vec{R}'}\psi(\vec{r}+\vec{R}) = \psi(\vec{r}+\vec{R}+\vec{R}')\\ = \psi(\vec{r}+\vec{R}'+\vec{R}) = \hat{T}_{\vec{R}}\psi(\vec{r}+\vec{R}') = \hat{T}_{\vec{R}}\hat{T}_{\vec{R}'}\psi(\vec{r}),\end{aligned} \tag{3.15}$$

and thus,

$$\hat{T}_{\vec{R}'}\hat{T}_{\vec{R}}\psi = \hat{T}_{\vec{R}}\hat{T}_{\vec{R}'} = \hat{T}_{\vec{R}+\vec{R}'}. \tag{3.16}$$

It follows that

$$\lambda_{\vec{R}}\lambda_{\vec{R}'} = \lambda_{(\vec{R}+\vec{R}')} \tag{3.17}$$

which is true when

$$\lambda_{\vec{R}} = e^{i\vec{k}\cdot\vec{R}}. \tag{3.18}$$

So that the equation (3.14) gets its final form [70]

$$\hat{T}_{\vec{R}}\psi_{n\vec{k}}(\vec{r}) = e^{i\vec{k}\cdot\vec{R}}\psi_{n\vec{k}}(\vec{r}) \tag{3.19}$$

which is the Bloch theorem.

Alternative forms for the Bloch theorem exist and one of those can be written as

$$\psi_{n\vec{k}}(\vec{r}+\vec{R}) = e^{i\vec{k}\cdot\vec{R}}\psi_{n\vec{k}}(\vec{r}) \tag{3.20}$$

using equations (3.2), (3.14) and (3.18). It states that in a periodic potential the wave functions of electrons differ from each other only by a periodic phase factor $e^{i\vec{k}\cdot\vec{R}}$. If we consider a function $u_{n\vec{k}} = e^{-i\vec{k}\cdot\vec{r}}$ which has the periodic property $u(\vec{r}+\vec{R}) = u(\vec{r})$ we end up the second and general form of the Bloch theorem [70]

$$\psi_{n\vec{k}}(\vec{r}) = e^{i\vec{k}\cdot\vec{r}}u_{n\vec{k}}(\vec{r}) \tag{3.21}$$

which is already given in equation (3.11).

The boundary condition was introduced that a large system such as a crystal can be described by a large amount of identical unit cells. That restricts the allowed wave vector $\vec{k}$ values of the solution. Let us assume that the crystal is formed by $M = M_1M_2M_3$ unit cells. Applying the periodic boundary condition we obtain the general form for the allowed wave vectors [70]

$$\vec{k} = \sum_{i=1}^{3}\frac{m_i}{M_i}\vec{b}_i, \tag{3.22}$$

where $\vec{b}_i$ are primitive reciprocal lattice vectors, m_i are integers for which $0 < m_i < M_i$, and M_i is the total number of lattice points along direction i. We notice that the allowed wave vectors have the same form as the reciprocal lattice vectors $\vec{K}$ (3.3) so that the wave vectors which deviate by the reciprocal lattice vector from each other are equivalent. Thus, they have the same eigenvalue because the equation (3.18) became $e^{i\vec{K}\cdot\vec{R}} = 1$ where we use the requirement (3.7) between Bravais and reciprocal lattice vector. Applying $e^{i\vec{K}\cdot\vec{R}} = 1$ to (3.20) we also obtain that the wave functions are the same.

As a conclusion the eigenstates and eigenvalues are periodic in a periodic potential. The Bloch theorem provides a significant simplification to the simulation of crystals. Instead of having to consider the whole crystal that is modelled by a large number of unit cells, we can reduce our infinite problem inside one unit cell in periodic crystals. The Schrödiger equation (3.9) is needed to be solved explicitly only in this particular unit cell. The solutions then recur periodically from one unit cell to another. In the reciprocal space eigenstates and eigenvalues are computed in the 1st Brillouin zone which are then the same in second, third and further in nth Brillouin zone.

3.1.4 Supercell approach

The Bloch theorem was derived for an ideal crystal without imperfections at 0 K. However, at finite temperature crystals are not perfect and always contain a finite number of imperfections, such as defects and impurities. They brake the periodicity of the system and the Bloch theorem no longer holds. The problem can be overcome by introducing a supercell approach [71].

A supercell can be thought as a unit cell that creates an artificial periodicity with periodic boundary condition property. In the case of point defects, such as vacancies, a supercell is constructed so that it consists of a piece of crystal in which a defect is located (Fig. 3a). The particular supercell is chosen for the unit cell of a system. A part of the crystal restricted inside the supercell should be large enough to avoid correlations between periodic images of defects. The defect in the supercell is repeated periodically in the crystal when the supercell is replicated throughout the crystal.

The supercell approach can also be applied to surfaces and isolated molecules. The supercell is constructed similarly as in the case of defects but because the molecules may have no periodicity and surfaces are periodic only in two directions, a vacuum region is needed to be introduced in a supercell. For surfaces a slab approach is used in which a slab consisting of a finite number of layers is placed inside a supercell. On top of the slab there exisst a vacuum region and the layer in the interface of the vacuum is the surface. Figure 3b) visualizes the situation. The slab should be thick enough that the layers below the surface have a bulk-behaviour. Similarly, one can place an isolated molecule inside the supercell where the rest is vacuum. The vacuum region in the supercell should also be thick enough that there is no correlation between the supercell and its periodic images.

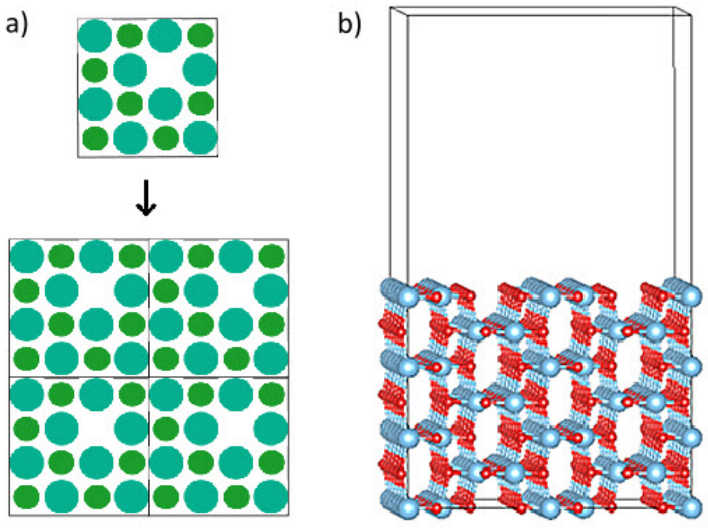

Figure 3: a) A point defect in a crystal made up of green and turquoise atoms. One green atom has been removed i.e. there is vacancy in the crystal. A supercell whose boundaries are shown with the box consists of a piece of crystal which is used to model the whole crystal. The vacancy repeats in each supercell periodically. Investigating surfaces a vacuum region is introduced in a supercell. A supercell with (100) surface of anatase TiO_2 is shown in b).

3.2 Plane wave basis set

Basis set is a set of basis functions which are used to describe the molecular orbitals in order to compute the energy of the system. Within DFT framework the corresponding molecular orbitals are KS orbitals χ_n^{KS}. The KS orbitals are constructed as a linear combination of the basis functions

$$\chi_n^{KS}(\vec{r}) = \sum_i c_{ni}\phi_i(\vec{r}). \tag{3.23}$$

Atomic orbitals centered on atoms are a typical choice for basis functions but in calculations of condensed matter in which the systems are usually periodic the plane wave basis set is more natural choice.

According to Bloch's theorem, the wave function of the periodic system can be expressed as a combination of a plane wave part and a periodic part. If the KS potential fulfills the translational invariance requirement, $V_s(\vec{r}+\vec{R}) = V_s(\vec{r})$, the KS orbitals can be written as

$$\chi_{n\vec{k}}^{KS}(\vec{r}) = e^{i\vec{k}\cdot r}u_{nk}(\vec{r}). \tag{3.24}$$

Plane waves are naturally periodic and therefore an excellent choice for basis set to describe the periodic part $u_{n\vec{k}}$. The plane wave basis functions of the KS orbitals are given by

$$\phi_i(\vec{r}) = \frac{1}{\sqrt{\Omega}}e^{i\vec{K}\cdot\vec{r}}, \tag{3.25}$$

where $1/\sqrt{\Omega}$ is the normalization factor and $\vec{K}$ is the reciprocal lattice vector, and thus the periodic part obtains the form [50]

$$u_{n\vec{k}}(\vec{r}) = \frac{1}{\sqrt{\Omega}}\sum_K c_{n\vec{K}}\, e^{i\vec{K}\cdot\vec{r}}. \tag{3.26}$$

By combining equations (3.24) and (3.26) we obtain the KS one-electron orbitals as an infinite sum of plane waves

$$\chi_{n\vec{k}}^{KS}(\vec{r}) = \frac{1}{\sqrt{\Omega}}\sum_{\vec{K}} c_{n(\vec{k}+\vec{K})}e^{i(\vec{k}+\vec{K})\cdot\vec{r}}, \tag{3.27}$$

where $c_{n(\vec{k}+\vec{K})}$ are the coefficients of the plane waves. This is the plane wave expansion that can be used to describe the Kohn-Sham one-electron orbitals.

KS equations (2.13) in a plane wave basis are written as

$$\sum_{\vec{K}}\left[\frac{\hbar^2}{2m}|\vec{k}+\vec{K}|^2\delta_{\vec{K}\,\vec{K}'} + \frac{1}{\sqrt{\Omega}}V_s(\vec{K}-\vec{K}')\right]\chi_{n\vec{k}}^{KS}(\vec{k}-\vec{K}) = \epsilon_{n\vec{k}}\chi_{n\vec{k}}^{KS}(\vec{k}-\vec{K}) \tag{3.28}$$

The Kronecker delta $\delta_{\vec{K}\,\vec{K}'}$ ensures the orthogonality of the plane waves.

3.3 Energy cutoff

To get exact results, an infinite basis set is needed to describe the wave function at each k-point. But computationally that is impossible and that is why the truncation of the plane

wave basis set (3.27) is necessary. Larger basis set provide more accurate results but also increase the computational cost. To choose the appropriate finite plane wave basis set for calculations, the balance between accuracy and efficiency has to be found by performing convergence tests.

The finite size of the plane wave basis set is defined by the energy cutoff. It determines the highest kinetic energy of all the basis functions and thus, the number of basis functions. The first term in Eq. (3.28) is the kinetic energy part. The kinetic energy cutoff is defined as

$$E_{cut} \geq \frac{\hbar^2}{2m} \left| \vec{k} - \vec{K} \right|^2 . \tag{3.29}$$

Plane waves with kinetic energy of smaller or equal to E_{cut} are only utilized as basis functions and used to form the finite basis set. The convergence with respect to the energy cutoff is tested by performing calculations by varying energy cutoff value. The initial value of energy cutoff is usually set to few hundred electronvolts and then gradually increased. This provides a systematic convergence. The value of the energy cutoff is increased until the desired convergence is reached.

3.4 K-point sampling

The properties of the system, i.e. the expectation value of an operator $\hat{A}$, such as the Hamiltonian, is obtained by integrating over occupied bands in the 1st Brillouin zone,

$$\langle \hat{A} \rangle = \frac{1}{V_K} \sum_n \int_{V_K} A_n(\vec{k}) f(\epsilon_n(\vec{k})) d\vec{k}, \tag{3.30}$$

where $A_n(\vec{k})$ is a matrix element $\langle \psi_n(\vec{k}) | \hat{A} | \psi_n(\vec{k}) \rangle$, V_K is the volume of the 1st Brillouin zone and f is the occupation number from the Fermi-Dirac distribution that takes the eigenvalues of the wave function $|\psi_n(\vec{k})\rangle$ as variables. However, the unknown analytical form of the integral causes problems. Therefore, the integral has to solve numerically. For that the integral is discretized by k-point sampling and the integral of the Brillouin zone is evaluated by a weighted sum over the selected k-point sampling

$$\langle \hat{A} \rangle = \sum_{n,\vec{k}} w_{\vec{k}} A_n(\vec{k}) f(\epsilon_n(\vec{k})). \tag{3.31}$$

A finite number of k-points is chosen and distributed to the Brillouin zone. The larger k-point sampling, the more accurate results but again, also the higher computational cost. Therefore, the convergence of the k-point sampling is also important to check to maximize the accuracy and minimize the computational cost. To reduce the number of k-points further the symmetry of the Brillouin zone of the system is also exploited. The convergence test is performed in the same way as for the energy cutoff.

In our work, the k-point sampling was set according to the Monkhorst-Pack scheme [72]. The integral is approximated by equally spaced sampling in the first Brillouin zone. As an input the Monkhorst-Pack k-point generator takes three subdivisions N_x, N_y and N_z along the reciprocal lattice vectors. A $(N_x \times N_y \times N_z)$ gives the size of the k-space. The k-points are then given as a following sum [72]

$$\vec{k} = \sum_{i=1}^{3} \frac{2n_i - N_i - 1}{2N_i} \vec{b}_i, \tag{3.32}$$

where $\vec{b}_i$ are reciprocal lattice vectors and $n_i = 1, 2, \ldots, N_i$.

The approximation of the integral of the Brillouin zone may be improved by the tetrahedron method with the Blöchl correction [73]. It is one of the smearing methods that are mathematical tools to improve the conditioning of the problem and thereby improve the convergence of the calculations. The tetrahedron method divides the 1st Brillouin zone into tetrahedra. It requires at least 4 k-points to sample the 1st Brillouin zone. The eigenvalues and the matrix elements in Eq. (3.30) for k-points are calculated at the corners of each tetrahedron while interpolated linearly inside the tetrahedron. That enables the calculation of the integral. However, the interpolation method is the main source of error due to the linear approach. The positive curvature of the matrix element is overestimated but regions of negative curvature are underestimated. Blöchl introduced a correction to integration weights to correct the integrataion over the Brillouin zone.

The tetrahedron method is applicable for insulators and semiconductors [73] but the non-variationality with respect to the partial occupancies causes problems in the case of metals. Because for insulators and semiconductors partial occupancies are either filled or empty, the forces and stresses will be correctly calculated. However, in metals there are partially filled bands and the Fermi surface becomes more fuzzy at finite temperatures. Therefore, calculated forces and stress tensors are usually wrong. To find the Fermi surface a part of the unoccupied bands near the Fermi surface need to be included in the calculations. That can be done by employing another smearing method called Gaussian smearing method [74]. A Gaussian function is used as a smooth operator to smear the bands in energy. More k-points will be effectively on the Fermi surface. The Gaussian smearing function is given by [74]

$$f(\epsilon_{n,\vec{k}}) = \frac{1}{2}\left[1 - \mathrm{erf}\left(\frac{\epsilon_{n,\vec{k}} - \mu}{\sigma}\right)\right]. \tag{3.33}$$

where erf(x) is the standard error function, μ is the chemical potential and $\sigma = k_B T$ is the smearing parameter that determines the width of the smearing. Due to the Gaussian smearing the total energy is no longer variational and therefore, it is more useful to replace the total energy by a generalized free energy

$$F = E - \sum_{n,\vec{k}} w_{\vec{k}} \sigma S(f_{n,\vec{k}}), \tag{3.34}$$

where S is the entropy correction contributing to the free energy. σ does not have any physical meaning. As said, it is just a mathematical tool to improve the numerical solving. It also leaves the physical meaning of the free energy unclear. The physical total energy is obtained by extrapolation for $\sigma \to 0$ from finite temperature [74],

$$E(\sigma \to 0) = E_0 = \frac{1}{2}(F + E). \tag{3.35}$$

The Gaussian smearing method works also for insulators and semiconductors and is the safest option if there is not enough information on the investigated system.

3.5 Pseudopotential

To simplify calculations of materials even more the concept of pseudopotential is introduced [50]. The behaviour of core and valence electrons differs from each other. Valence electrons in

an outermost shell of an atom participate chemical reactions, bond forming and excitations while core electrons, that are tightly bonded and thus highly localized around their nuclei, do not. They are almost independent from the chemical environment. All-electron wave function has a characteristic oscillation in the core region due to the requirement of the orthogonality between core and valence states. Many plane waves i.e. larger E_{cut} (Eq. (3.29)) is needed to describe those fast wiggles of the core wave function. Taking into account both, core and valence electrons may still be too expensive computationally when using a plane wave basis set.

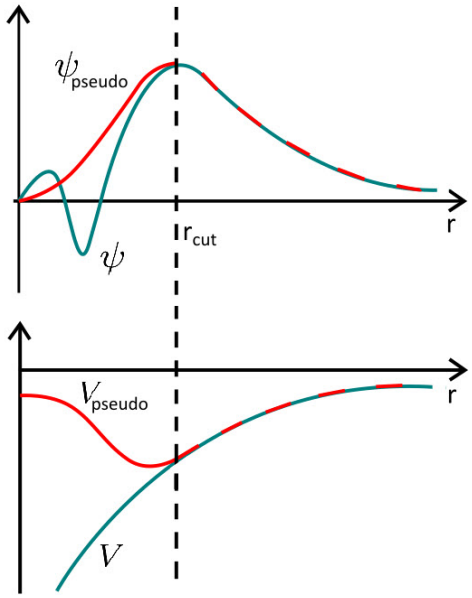

Figure 4: Pseudopotential approximating the effect of the core region resulting in the wave function without radial nodes. Outside of the radius r_{cut} the psedopotential yields the same results as the all-electron potential i.e. $V = V_{pseudo}$ and $\psi = \psi_{pseudo}$. The all-electron wave function and potential are shown in blue line, and pseudo wave function and pseudopotential in red line.

To reduce the basis set size, the core electrons and the strong Coulomb potential of the nuclei are replaced by a smoother and weaker effective potential, called pseudopotential. The approach treats them according to the frozen core approximation while valence electrons affected by the pseudopotential are treated explicitly. Beyond a certain cutoff radius r_{cut} form the nucleus, the pseudopotnetial and the corresponding pseudo wave function should be identical to the true potential and all-electron wave function (Fig. 4). There are many families of pseudopotentials, such as norm-conserving pseudopotentials [76] and ultrasoft pseudopotentials [77].

When the pseudopotential method is used the effective potential can be represented with fewer Fourier coefficients than the true potential [50]. This makes the plane wave basis set computationally more feasible. The drawback of this method, because the core electrons are incorrectly described, is the loss of information from the core region.

However, there exist all-electron methods, such as augmented wave method (APW) [78], that include core electrons in the calculations using the muffin-tin approximation. The space is divided into two regions around each nucleus: core sphere (muffin tin) and interstitial

for which different basis sets are employed. Radial solutions to the Shrödinger equation and spherical harmonics are used in core spheres and plane waves in interstitial regions. APW can be improved by linearization that eliminates the energy dependence of the radial solutions. This method is known as linear augmented plane wave method (LAPW) [78, 79].

3.6 Projector augmented wave method

Projector augmented wave (PAW) method [80] is an all-electron method which is an extension of the pseudopotential and the LAPW method. The basic idea behind the PAW method is to transform the true wave function into smooth and computationally more convenient wave function by using a linear transformation.

The linear transformation $\mathcal{T}$ is an operation that transforms a smooth pseudo wave function $|\tilde{\psi}_n\rangle$ into an all-electron wave function $|\psi_n\rangle$,

$$|\psi_n\rangle = \mathcal{T}\,|\tilde{\psi}_n\rangle\,, \tag{3.36}$$

where n is the band index. In DFT framework, all-electron wave functions $|\psi_n\rangle$ correspond to the Kohn-Sham one-electron orbitals $\left|\chi_n^{KS}(\vec{r})\right\rangle$ introduced in chapter 2.4. Operator $\mathcal{T}$ modifies the pseudo wave function in all regions around the nuclei. Because the pseudo wave function is already smooth beyond a radius r_{cut} the linear transformation is defined as [80]

$$\mathcal{T} = 1 + \sum_R \hat{\mathcal{T}}_R \tag{3.37}$$

where $\hat{\mathcal{T}}_R$ are the atom-centered contributions that act only within an augmentation i.e. core spheres around each atom R.

Inside the augmentation sphere, $|\vec{r}-\vec{R}| < r_{cut}$, the all-electron wave function is expanded into complete partial wave basis set $|\varphi_m\rangle$ for which a corresponding smooth auxiliary wave function

$$|\varphi_m\rangle = (1 + \hat{\mathcal{T}}_R)\,|\tilde{\varphi}_m\rangle \tag{3.38}$$

is obtained by utilizing equation (3.37). Outside of the augmentation sphere, $r > r_{cut}$, $|\varphi_m\rangle = |\tilde{\varphi}_m\rangle$.

The pseudo wave function can be now represented in terms of a partial wave basis set

$$|\tilde{\psi}_n\rangle = \sum_m c_{nm}\,|\tilde{\varphi}_m\rangle\,. \tag{3.39}$$

Since $|\varphi_m\rangle = \mathcal{T}_R\,|\tilde{\varphi}_m\rangle$, the corresponding all-electron wave function is

$$|\psi_n\rangle = \mathcal{T}\,|\tilde{\psi}_n\rangle = \sum_m c_{nm}\,|\varphi_m\rangle\,. \tag{3.40}$$

The coefficients c_{nm} are identical in equations (3.39) and (3.40). Due to the linearity of the transformation $\mathcal{T}$ the coefficients must be linear functionals of the pseudo wave function. Expressed as an inner product the coefficients are

$$c_{nm} = \langle \tilde{p}_m|\tilde{\psi}_n\rangle\,, \tag{3.41}$$

where $|\tilde{p}_m\rangle$ are smooth projector functions that satisfy the condition

$$\sum_m |\tilde{\varphi}_m\rangle \langle\tilde{p}_m| = 1. \tag{3.42}$$

This further implies the orthogonality between projector functions and smooth partial waves

$$\langle\tilde{\varphi}_m|\tilde{p}_{m'}\rangle = \delta_{m,m'} \tag{3.43}$$

inside the augmentation spheres. [80]

Using the completeness relation (3.42) the linear transformation can be written as

$$\mathcal{T} = 1 + \sum_m (|\varphi_m\rangle - |\tilde{\varphi}_m\rangle) \langle\tilde{p}_m| \tag{3.44}$$

and, by utilizing the above result, the all-electron wave function as

$$\begin{aligned} |\psi_n\rangle &= |\tilde{\psi}_n\rangle + \sum_{n,m} (|\varphi_m\rangle - |\tilde{\varphi}_m\rangle) \langle\tilde{p}_m|\tilde{\psi}_n\rangle \\ &= |\tilde{\psi}_n\rangle + \sum_{n,m} |\varphi_m\rangle \langle\tilde{p}_m|\tilde{\psi}_n\rangle - \sum_{n,m} |\tilde{\varphi}_m\rangle \langle\tilde{p}_m|\tilde{\psi}_n\rangle \\ &= |\tilde{\psi}_n\rangle + |\psi_n'\rangle + |\tilde{\psi}_n'\rangle . \end{aligned} \tag{3.45}$$

The transformation thus consists of three components: pseudo plane wave part ($|\tilde{\psi}_n\rangle$), all-electron on-site part ($|\psi_n'\rangle$) and pseudo on-site part ($|\tilde{\psi}_n'\rangle$).

To calculate expectation values of pseudo wave functions, a transformed operator called pseudo operator [80]

$$\begin{aligned} \tilde{A} &= \mathcal{T}^\dagger \hat{A} \mathcal{T} \\ &= \hat{A} + \sum_{m,l} |\tilde{p}_m\rangle \left(\langle\varphi_m| \hat{A} |\varphi_l\rangle - \langle\tilde{\varphi}_m| \hat{A} |\tilde{\varphi}_l\rangle \right) \langle\tilde{p}_l| \end{aligned} \tag{3.46}$$

is needed. Utilizing the above equation the electron density gets the form

$$n(\vec{r}) = \tilde{n}(\vec{r}) + n'(\vec{r}) - \tilde{n}'(\vec{r}), \tag{3.47}$$

where $\tilde{n}(\vec{r})$ is the pseudo electron density and $n'(\vec{r})$ and $\tilde{n}'(\vec{r})$ are the all-electron and pseudo onsite electron densities, respectively. The electron densities are defined as [80]

$$\begin{aligned} \tilde{n}(\vec{r}) &= \sum_n f_n \langle\tilde{\psi}_n|\vec{r}\rangle \langle\vec{r}|\tilde{\psi}_n\rangle , \\ n'(\vec{r}) &= \sum_{n,i,j} f_n \langle\tilde{\psi}_n|\tilde{p}_i\rangle \langle\varphi_i|\vec{r}\rangle \langle\vec{r}|\varphi_j\rangle \langle\tilde{p}_j|\tilde{\psi}_n\rangle \end{aligned}$$

and

$$\tilde{n}'(\vec{r}) = \sum_{n,i,j} f_n \langle\tilde{\psi}_n|\tilde{p}_i\rangle \langle\tilde{\varphi}_i|\vec{r}\rangle \langle\vec{r}|\tilde{\varphi}_j\rangle \langle\tilde{p}_j|\tilde{\psi}_n\rangle$$

where f_n is the occupation of the state.

The transformed eigenvalue equation of the pseudo wave functions is

$$\tilde{H}\,|\tilde{\psi}_n\rangle = \mathcal{T}\dagger\hat{H}\mathcal{T}\,|\tilde{\psi}_n\rangle = E_n\mathcal{T}\dagger\mathcal{T}. \tag{3.48}$$

Since the total energy is a functional of the electron density, similarly as the electron density the total energy functional

$$E[n] = \sum_n f_n\,\langle\psi_n|-\frac{1}{2}\nabla^2\,|\psi_n\rangle+\frac{1}{2}\int\int\frac{(n+n^Z)(n+n^Z)}{|\vec{r}-\vec{r}'|}d\vec{r}d\vec{r}'+\int n(\vec{r})\epsilon_{XC}(n(\vec{r}))d\vec{r}, \tag{3.49}$$

where n^Z is the point charge of the nucleus, can be split into three terms,

$$E = \tilde{E} + E' - \tilde{E}'. \tag{3.50}$$

The plane wave part, $\tilde{E}$, is evaluated on a regular grid in real or Fourier space while atom-centered contributions E' and $\tilde{E}'$ are evaluated on a radial grid. [80]

Because the norm of the pseudo wave functions is not the same as all-electron wave functions localized in PAW sphere a compensation electron density is introduced to treat the long-range electrostatic interaction and correct multipole moments of the all-electron electron density [80]. The compensation electron density is defined as

$$\rho = \sum_R \rho_R, \tag{3.51}$$

where

$$\rho_R(\vec{r}) = \sum_L g_{RL}(\vec{r})Q_{RL} \tag{3.52}$$

is a sum of one center terms expressed in terms of generalized Gaussians

$$g_{RL}(\vec{r}) = C_l|r-R|^l Y_{lm}(r-R)e^{(|r-R|/r_c)^2} \tag{3.53}$$

and multipole moments

$$Q_{RL} = \int |r-R|^l[n'_R(\vec{r}) + n^Z_R(\vec{r}) - \tilde{n}'_R(\vec{r})]Y^*_{lm}(r-R). \tag{3.54}$$

Compensation electron density is added to the pseudo electron density $\tilde{n}'$. Similarly, a compensation electron density ρ' is added to the pseudo on-site electron density $\tilde{n}'$.

Index R describes a nuclear site and parameter C_l is the normalization constant which is determined so that its multiple moment is unity [80]. Y_L is a spherical harmonic function with quantum numbers l and m, $L = (l,m)$, and r_c is the decay length inside which the compensation electron density is localized and decays to zero when approaching r_c. Outside of the decay length ρ is zero.

Due to the decaying within core spheres a large plane wave cut off is usually needed for pseudo electron density. But as in the pseudopotential method, the problem can be overcome by introducing the effective compensation electron density ρ' which produces the

same multipole moment as ρ with g'_{RL} with larger decay length r'_c. The electrostatic energy, the second term in (3.49), can be rewritten as [80]

$$\frac{1}{2}\int\int\frac{(\tilde{n}+\rho)(\tilde{n}+\rho)}{|\vec{r}-\vec{r}'|}d\vec{r}d\vec{r}' = \frac{1}{2}\int\int\frac{(\tilde{n}+\rho')(\tilde{n}+\rho')}{|\vec{r}-\vec{r}'|}d\vec{r}\,d\vec{r}' + \int\tilde{n}(\vec{r})v(\vec{r})d\vec{r} + \sum_{R,R'}U_{R,R'}, \tag{3.55}$$

where $v(\vec{r})$ is an arbitrary potential localized in core spheres. The first and second terms in (3.55) can be evaluated in reciprocal space but the third, short-ranged pair potential

$$U_{R,R'} = \frac{1}{2}\int\int\frac{\rho_R(\vec{r})\rho_R(\vec{r}') - \rho'_R(\vec{r})\rho'_R(\vec{r}')}{|r-r'|}d\vec{r}d\vec{r}' \tag{3.56}$$

between two atoms can be evaluated analytically [80].

4 Details of calculations

All the spin-polarized density functional theory calculations were performed using Vienna Ab initio Simulation Package (VASP) [81, 82]. The spin-polarized DFT is needed due to magnetism originating from hematite. Based on the Bloch's theorem we are allowed to reduce the problem of infinite system inside a single unit cell. The exchange-correlation potential was described by the generalized gradient approximation (GGA) parameterized by Perdew-Burke-Ernzerhof (PBE) functional [55]. It is known that GGA does not accurately describe the d and f electrons of the system and therefore, the Hubbard correction according to Dudarev *et al.* [69] is added to the calculations to describe the on-site Coulomb interaction between localized electrons and correct the electronic structure. The Projector augmented wave (PAW) [80] method is employed to describe the electron-ion potential. VASP uses plane wave basis sets with a chosen energy cutoff to expand the wave function of the valence state electrons. The atomic species: iron, titanium and oxygen, are described by 8 ($3d^64s^2$), 4 ($3d^24s^2$) and 6 ($2s^22p^4$) valence electrons, respectively. The first Brillouin zone of the unit cells were sampled by k-point sampling according to the Monkhorst-Pack scheme [72]. In relaxation steps the convergence for energy is chosen as 10^{-6} eV between two steps and the atomic relaxation is performed until the forces on the ions are less than 0.001 eV $Å^{-1}$. For the construction and the visualization of the investigated structures we used the VESTA (visualization for electronic and structural analysis) program [83] and for the analysis of computed observables we utilized the VASPKIT toolkit [84].

The following subsections briefly introduce the main step in DFT calculations, the relaxation, and the main quantities we computed to investigate the phenomena in the modelled systems.

4.1 Structural relaxation

A DFT calculation is started by optimizing a simulated structure. In the relaxation stage the equilibrium geometry of the structure with the lowest energy is obtained. It requires the optimization of the ionic positions and the crystal unit cell which requires the calculation of the forces between atoms. The forces are minimized following the Hellmann-Feynman theorem [50, 85, 86] by specifying tolerance criteria.

The force on an atom is obtained from the first derivative of the total energy E with respect to the position $\vec{R}_I$ of the nucleus,

$$\vec{F}_I = -\frac{\partial E}{\partial \vec{R}_I}. \tag{4.1}$$

The Hellmann-Feynman theorem states that the particular energy derivative can be calculated by evaluating the expectation value of the total energy with respect to any parameter λ, such as position, and the Hamiltonian is derived from that. Taking the derivative of the expectation value $E = \langle\psi|\,\hat{H}\,|\psi\rangle$ with respect to position, the expression for the Hellmann-Feynman forces within DFT framework are written as [50]

$$\vec{F}_I = \frac{\partial E}{\partial \vec{R}_I} = -\langle\psi|\,\frac{\partial \hat{H}}{\partial \vec{R}_I}\,|\psi\rangle - \frac{\partial E_{II}}{\partial \vec{R}_I}. \tag{4.2}$$

The first term is the general Hellmann-Feynman theorem which gives the forces as expectation values of the gradient of the electronic Hamiltonian in the ground state $|\psi\rangle$. E_{II},

the classical ion-ion interaction energy, is the second term that depends explicitly upon the position. Using the equation (2.20) the forces become

$$\vec{F}_I = -\int \frac{\partial V_{\text{ext}}(\vec{r})}{\partial \vec{R}_I} n(\vec{r}) d\vec{r} - \frac{\partial E_{II}}{\partial \vec{R}_I}, \tag{4.3}$$

where $V_{\text{ext}}(\vec{r})$ is the potential of the KS system which corresponds to the pseudopotential that is used in calculations.

Optimizing the size and shape of the unit cell of the periodic system the equilibrium lattice parameters of the system are determined. This requires the calculation of stresses in the system. The stress described by the stress tensor $\sigma_{\alpha\beta}$ is defined as the derivative of the total energy with respect to the strain tensor $\epsilon_{\alpha\beta}$ per unit volume, [50]

$$\sigma_{\alpha\beta} = \frac{1}{\Omega} \frac{\partial E}{\partial \epsilon_{\alpha\beta}} \tag{4.4}$$

where Ω is the volume of the unit cell, and α and β are indices of Cartesian components. Changes in lattice vectors $\vec{a}_i$ are described in terms of the strain tensor by $\vec{a}'_i = (I + \epsilon_{\alpha\beta})\vec{a}_i$ where I is the unit tensor. Applying the Hellmann-Feynman-theorem with the lattice parameter as the λ parameter, the stress tensor can be written as

$$\sigma_{\alpha\beta} = -\langle\psi| \frac{\partial \hat{H}}{\partial \vec{a}'_i} |\psi\rangle . \tag{4.5}$$

For bulk materials the ionic positions as well as the unit cell, its shape and volume, are optimized. However, if simulating surfaces or single molecules, only the ionic positions are optimized. The Figure 3b) visualizes the supercell approach used for surfaces. If the shape and the volume of the supercell would be optimized the vacuum region in the supercell would be eliminated immediately. Therefore, the shape and the volume of the supercell are fixed during the optimization of the ionic positions. As the relaxation stage has finished successfully, observables can be computed for the optimized system.

4.2 Work function

The work function is characteristic of a surface which is the minimum energy required to ionize an electron from it. As a surface property it is also a relevant measure when investigating photocatalysts. Mathematically, work function is formulated as a difference between the vacuum potential E_{vacuum} and the Fermi energy E_F of the system,

$$W = E_{\text{vacuum}} - E_F. \tag{4.6}$$

We included only the electrostatic potential in the Hamiltonian when calculating work functions, meaning the exchange-correlation potential is not accounted for. This is because it can give unphysical values in the vacuum region being a functional of electron density.

Being a property of a surface the work function is affected by changes occurring on the surface. One major factor that can change the work function of a surface is the adsorption of an adsorbent on it. An adsorbent can act as electropositive or electronegative either donating electrons to the surface or accepting them from the surface. An electropositive adsorbent decreases the work function while an electronegative adsorbent increases it. This allows us to identify the interaction between the surface and the adsorbent.

4.3 Density of states

The density of states (DOS) of a system is calculated by performing a non-self-consistent calculation for the relaxed structure. Density of states tells the number of states available in the energy range of $E - dE$. At the energy E the total DOS is defined as

$$D(E) = \frac{1}{V} \sum_{i}^{N} \delta(E - \epsilon_i(\vec{k})) \tag{4.7}$$

where ϵ_i are the eigenvalues of the KS orbitals. The total DOS can be projected on to the individual orbitals of the elements of the system to investigate their contribution to the total DOS. The computed partial density of states (PDOS) provides the information about the contributions of different orbitals.

The DOS is sampled by discrete eigenvalue points but a smearing method is used to broaden the eigenvalues and make the DOS smooth and continuous distribution. In Figure 5 an example of the influence of the Gaussian smearing to the eigenvalues is given. However, non-smooth points that are called van Hove singularities appear in DOS. The singularities occur at the wavevectors at which there is a critical point in the electronic band structure. At those wavevectors, the integrand in DOS diverges and a non-smooth feature arises.

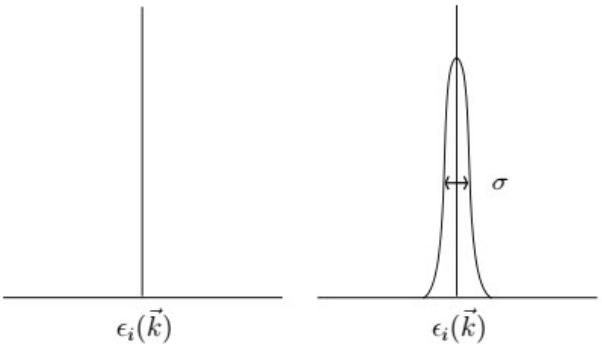

Figure 5: Gaussian smearing of a KS eigenvalue by width of σ.

4.4 Spin and charge density differences

The electron density $n(\vec{r})$ introduced in Chapter 2.4 is the total electron density which is the sum of electron densities of spin-up $n_\uparrow(\vec{r})$ and spin-down $n_\downarrow(\vec{r})$ electrons (Eq. (2.27)). Multiplying the electron density by elementary charge e the charge density ρ is obtained. In contrast, the difference of the $n_\uparrow(\vec{r})$ and $n_\downarrow(\vec{r})$ gives the spin density $s(\vec{r})$. If the spin density is differing from zero, then $n_\uparrow(\vec{r}) \neq n_\downarrow(\vec{r})$ and a spin polarization appears in the system. The DOS can reveal the spin polarization, having antisymmetric components of spin-up and spin-down states.

In this thesis we have modelled the combined system of the TiO_2 surface and the α-Fe_2O_3 cluster. The surface and the cluster form an interface and to get information on charge transfer phenomena, the charge distribution in the system is analysed by charge density difference. The charge density difference is calculated by

$$\Delta\rho(\vec{r}) = \rho_{AB}(\vec{r}) - \rho_A(\vec{r}) - \rho_B(\vec{r}) \tag{4.8}$$

where $\rho_{AB}(\vec{r})$ is the total charge density of the combined system, and $\rho_A(\vec{r})$ and $\rho_B(\vec{r})$ are the total charge densities of the subsystems A and B with atoms in exactly the same positions as they occupy in the combined system. Correspondingly, to elucidate magnetic properties, we can calculate the spin density difference,

$$\Delta s(\vec{r}) = s_{AB}(\vec{r}) - s_A(\vec{r}) - s_B(\vec{r}) \tag{4.9}$$

where $s_{AB}(\vec{r})$, $s_A(\vec{r})$ and $s_B(\vec{r})$ are the total spin densities of the combined system, and the subsystem A and B. Again, the atoms of the subsystems locate exactly at the same sites as in the combined system. The isosurface plots of the charge and spin density differences obtained by VESTA reveal how the charge and spin density distributes and provides the visualization that is needed to elucidate the charge transfer and magnetic phenomena occurring in the system.

4.5 Bader charge analysis

DFT calculations yield the total electron density of systems but no information on how it is partitioned among the atoms in the system. However, in 1981 Richard Bader proposed a way to divide a system into subsystems which based only on the electron density [87]. The space is divided in subsystems, such as atoms by partitioning the electron density according to the zero-flux surfaces on which the normal component of the electron density gradient is zero,

$$\nabla n(\vec{r}) \cdot \hat{n} = 0, \tag{4.10}$$

where $\hat{n}$ is the unit vector normal to the surface, or according to the surfaces on which the gradient of $n(\vec{r})$ reaches it minimum. The surfaces separate the charge density volumes, called Bader volumes, around each charge density maximum. The maxima are usually centered at atoms while zero or minimum gradients occur between atoms. Thus, the proposal provides the separation of individual atoms of systems.

By integrating the electron density over Bader volume the Bader charge of an atom is calculated that can be analysed by Bader charge analysis for which the Henkelman's group provides computational code [88, 89]. The Bader charge is known as a measure of electron occupation on an atom while Bader volume provides information on the localization of the Bader charge around atoms. The Bader net atomic charges ρ_{BNAC}, that quantify the charge transfer between atoms, are calculated from the formula,

$$\rho_{\mathrm{BNAC}} = \rho_{\mathrm{ve}} - \rho_{\mathrm{BC}}, \tag{4.11}$$

where ρ_{ve} is the number of valence electron which is 8 for iron, 4 for titanium and 6 for oxygen in this thesis, and ρ_{BC} is the Bader charge of the atom. The analysis provides quantitative measure of local charge states in the system. With the charge density difference plot the Bader charges are used to investigate the possible charge transfer mechanism in the systems.

5 Precalculations for bulk α-Fe_2O_3

At very first, we simulated bulk hematite. α-Fe_2O_3 was modelled using the hexagonal representation for the unit cell [18, 24]. The total number of atoms in the unit cell was 30: 12 iron and 18 oxygen atoms (Fig. 1a)). The convergence tests were performed for the structure to find an optimal k-point sampling and energy cutoff. After that the structure of bulk α-Fe_2O_3 was optimized using the converged values for the parameters.

5.1 Convergence tests

Before the actual calculations the convergence of the total energy with respect to k-point sampling and energy cutoff were tested to ensure the accuracy of the results but at the same time the reasonable computational cost.

The convergence of k-point sampling was tested first. The uniform mesh of k-points was spaced around the Γ-point by Monkhorst-Pack scheme [72]. The total energy of the unit cell was calculated with six different k-point sampling without shifting: $2 \times 2 \times 1$, $3 \times 3 \times 1$, $4 \times 4 \times 1$, $5 \times 5 \times 1$, $4 \times 4 \times 2$ and $5 \times 5 \times 2$. At this point the energy cutoff was set to 550 eV [24]. The results are shown in Fig 6. Based on the convergence test, the k-grid of $4 \times 4 \times 1$, which corresponds to 10 irreducible k-points in the first Brillouin zone, was found to provide the lowest energy for the bulk α-Fe_2O_3 so this k-point sampling was chosen.

The calculation did not finish successfully with k-grid of $4 \times 4 \times 2$. Therefore, it cannot be included in the results and that is the reason why it has been omitted from the graph. It was concluded that the symmetry of the lattice of the α-Fe_2O_3 is incompatible with this particular k-point sampling.

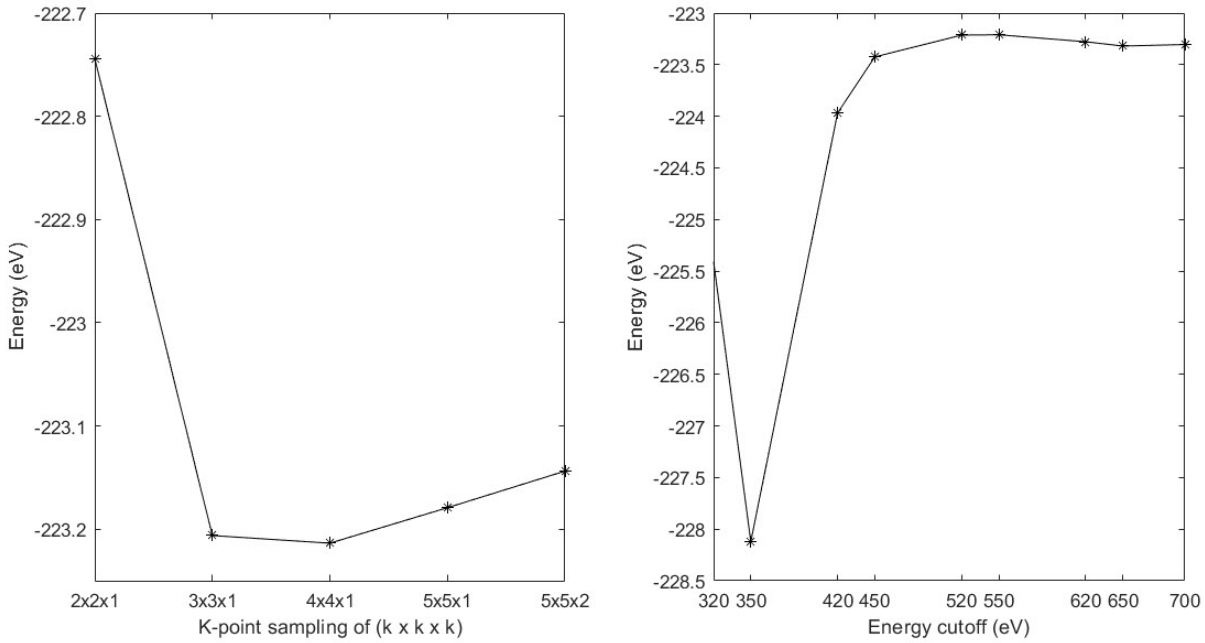

Figure 6: Convergence of total energy of the bulk Fe_2O_3 with respect to k-point sampling (on the left) and energy cutoff (on the right).

The convergence of total energy with respect to energy cutoff with the chosen k-point

sampling, $4 \times 4 \times 1$, was tested. The energy cutoff was varied in a range of 320 eV and 700 eV. The results are shown in Figure 6 b. It was found that the sufficient value for energy cutoff is 650 eV. Therefore this value was chosen for the rest of the calculations. The converged k-point sampling $4 \times 4 \times 1$ was chosen to be used for the following calculations for the bulk hematite. For a different system the k-point sampling needs to be changed.

5.2 Computational details

The geometry of the bulk α-Fe_2O_3 is relaxed using the chosen converged values of the k-point sampling, $4 \times 4 \times 1$, around the Γ-point and energy cutoff, 650 eV. The Gaussian smearing with $\sigma = 0.05$ eV was used. The full relaxation for the bulk structure was performed to obtain the optimized structure with the lowest energy. The exchange-correlation energy was described by generalized gradient approximation. As known, standard DFT with the GGA functional does not correctly describe the localized 3d electrons of α-Fe_2O_3 [24]. To obtain more realistic electronic structure, the Hubbard correction was introduced in DFT studies as GGA+U according to the Dudarev approach [69]. In previous studies the Hubbard correction has been chosen to be around 4 eV for hematite which is reported to produce the correct electronic structure. We performed the calculations with the two different values of $U_{\text{eff}} = 3.8$ eV [17] ($U = 3.8$ eV and $J = 0$ eV) and $U_{\text{eff}} = 4$ eV [24, 90] ($U = 4.0$ eV and $J = 0$ eV). The atomic relaxation is performed until the forces on the ions are less than 0.001 eV Å^{-1}.

The density of states (DOS) was calculated for the optimized bulk structure within both the GGA and the GGA+U approximations. For the DOS of the bulk hematite the Blöchl tetrahedron smearing method [73] was used as it is known to be a semiconductor. The Fermi energy was set to zero in the DOS plots.

5.3 Bulk α-Fe_2O_3

The unit cell of the bulk α-Fe_2O_3 was relaxed within the GGA approximation. The cell parameters of the optimized unit cell of the bulk were found to be $a = b = 4.780$ Å and $c = 13.323$ Å. Parameters are in good agreement with the experimental values of $a = b = 5.035$ Å and $c = 13.747$ Å [18]. On the other hand, the magnetization of 0.952 μ_{B} is not comparable to the experimental value of 4.9 μ_{B} [29].

The total DOS of bulk α-Fe_2O_3 near the Fermi level is shown in Figure 7. The DOS indicates metallic nature for α-Fe_2O_3. There is no band gap observed between the valence band and the conduction band. However, α-Fe_2O_3 is known to be a semiconductor, having a charge transfer insulating nature [17, 22]. It can be deduced that the GGA predicts incorrect results for α-Fe_2O_3. The band gap and the magnetic moment are clearly underestimated.

To correct the electronic structure of the bulk α-Fe_2O_3 the Hubbard correction was introduced. As previously, the structure of the bulk was optimized within the GGA+U approximation. For $U_{\text{eff}} = 3.8$ eV the optimized cell parameters were $a = 5.1247$ Å and $c = 13.8767$ Å and the predicted magnetic moment was 4.315 μ_{B}. For $U_{\text{eff}} = 4$ eV the cell parameters were $a = 5.1231$ Å and $c = 13.8705$ Å and the magnetic moment was 4.328 μ_{B}. Compared to the GGA calculation, the GGA+U yielded the cell parameters that are closer to the experimental values [18], and in addition, the obtained magnetic moment has now a good agreement with the experimental one [29] in both cases. Of the Hubbard corrections,

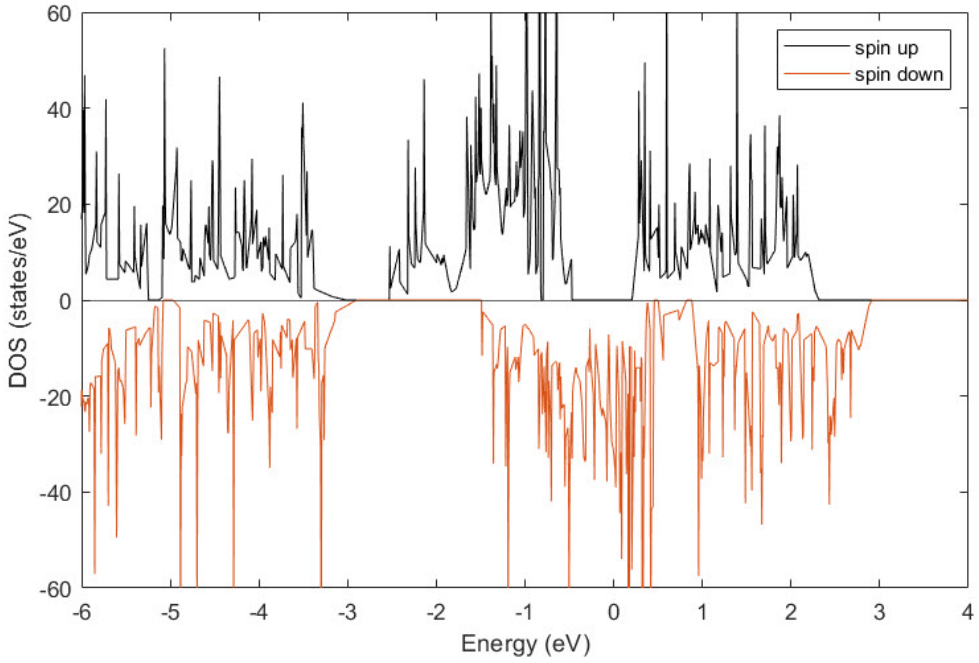

Figure 7: Density of states of bulk α-Fe_2O_3 using the GGA functional.

the value of 4 eV seems to yield slightly more accurate results.

The GGA+U computed total DOSs are shown in Figure 8. The $U_{\text{eff}} = 3.8$ eV gave a band gap of around 1.1 eV indicating that α-Fe_2O_3 is a semiconductor, as it should be (Fig. 8a)). However, the predicted band gap is still underestimated. In addition, the quality of the DOS is not especially good but it is rather spiky. To improve the quality of the DOS in the calculation with $U_{\text{eff}} = 4$ eV, the k-point sampling and the width of the smearing were increased from $4 \times 4 \times 1$ to $8 \times 8 \times 3$ and from 0.05 to 0.1 eV. In addition, the energy range and the number of intervals on which the energy range is divided and in which the DOS is evaluated were increased. The computed DOS with the Hubbard correction of $U_{\text{eff}} = 4$ eV is shown in Figure 8b). The changes were observed to improve the quality of the DOS significantly. Essentially, hematite was correctly predicted to be a semiconductor although the band gap energy of 1.16 eV was still underestimated.

As said, both computed DOSs predict correctly hematite to be semiconductor. Below the energy value of -6 eV the DOS is dominated by the Fe 3d spin up states but approaching the Fermi level, valence band edge, the DOS is mainly composed by the oxygen 2p states with a smaller contribution of Fe 3d states. The conduction band is characterized by Fe 3d spin down states, indicating hematite to have a nature of p-d charge transfer insulator, agreeing with previous experimental [22, 23] and theoretical studies [17, 24]. Approximately beyond 5 eV a more symmetric character exists in the conduction band. The DOS reveals the existence of unpaired electrons. Asymmetric spin up and down components are observed which shows a parallel orientation for the magnetic moments of iron atoms. The obtained DOSs are comparable with the previous studies [17, 30, 31]. The GGA+U with $U_{\text{eff}} = 4.0$ eV predicted the band gap of around 1.16 eV which is in better agreement with the experimental results [19, 20]. It, nonetheless, underestimates the band gap energy, being still essentially a ground state theory. The predicted band gap does not correspond experimentally determined gaps so that the quantitative comparison is not fair in our case.

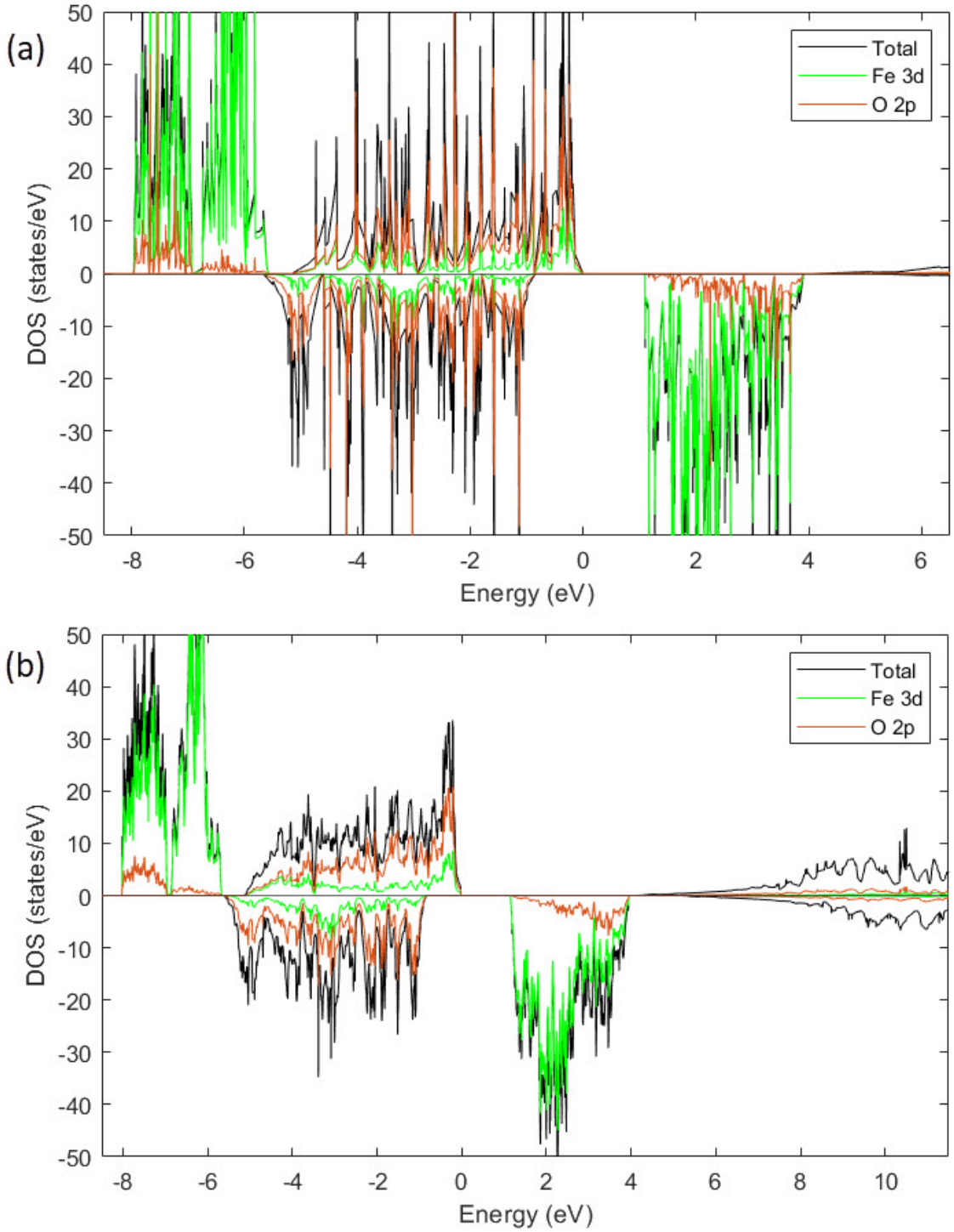

Figure 8: Density of states computed within the GGA+U with a) $U_{\text{eff}} = 3.8$ eV and b) $U_{\text{eff}} = 4$ eV for the bulk α-Fe_2O_3.

Since $U_{\text{eff}} = 4$ eV gave more accurate results for the lattice parameters, for the magnetic moments and for the electronic structure compared with the previous studies, we chose that value for the Hubbard correction for α-Fe_2O_3 to be used for the rest of the calculations.

α-Fe_2O_3 is known to be a magnetic system and therefore magnetism cannot be ignored. Hematite is known to have four different magnetic configurations, three anti-ferromagnetic (AFM) states and one ferromagnetic (FM) state, and in addition, there exists also a non-magnetic (NM) configuration [90]. Several studies have investigated the configurations and the most stable magnetic ordering has been found to be the AFM ++− configuration [17, 90]. In our calculation the magnetic moment of each Fe atom was predicted to be 4.328 μ_B resulting in a non-zero total magnetic moment. This indicates a ferromagnetic configuration for the α-Fe_2O_3 which is also upheld by the asymmetric DOS of it. Compared to the previous results [17, 30, 31] the calculated DOS in Figure 8b) has a good agreement with them. According to previous studies the magnetic moment of around 4.3 μ_B would be characteristic of a FM state [17, 90]. In any case, each magnetic configuration of α-Fe_2O_3 shows almost the same magnetic moment which are comparable to the experimental value.

6 Absorption of Fe_2O_3 cluster on TiO_2 surface

Although TiO_2 has been recognized to be an excellent photocatalyst for many applications, the drawbacks, such as large band gap and high recombination rate, limit its performance. It has been observed that the photocatalytic properties of TiO_2 surface can be enhanced by coupling it with a smaller band gap semiconductor, α-Fe_2O_3, which has a favourable band gap of 2.0 eV. It is widely recognized that the cocatalyst modifies the electronic structure of the photocatalyst and thus it can promote the visible light harvesting of the photocatalyst and decrease the recombination rate. In addition, previous papers have reported the formation of a heterojunction between TiO_2 and Fe_2O_3 which can enhance the photocatalytic performance [36, 37, 39]. The formation of both type I and type II heterojunctions have been reported depending on the system investigated. A type II heterojunction or Z-scheme heterojunction with staggered gap is generally more efficient than a type I heterojunction as it is capable of providing the spatial separation of electron-hole pairs into different locations [91]. This could also lead to higher charge transfer capacity.

We chose anatase phase for the TiO_2 surface. The previous studies have shown that anatase phase of TiO_2 exhibits generally higher photocatalytic activities than the other phases, rutile and brookite [92, 93]. The surface structure of the photocatalyst plays also an essential role in photocatalytic performance because the photocatalytic reaction occurs mainly on the catalyst surface. The (101) face of anatase is thermodynamically the most stable surface with the lowest formation energy [94] and it has similarly shown a superior photocatalytic performance compared to the other faces [95, 96].

α-Fe_2O_3 semiconductor was considered as a cluster. From now on, hematite is referred simply to Fe_2O_3, and the Fe_2O_3 cluster is denoted as $(Fe_2O_3)_n$. We first introduced the smallest size of hematite cluster: $(Fe_2O_3)_1$ with $n = 1$ which was attached on the anatase TiO_2 surface. The TiO_2 surface with Fe_2O_3 cluster was studied previously by Sun *et al.* for the degradation of phenol [40]. They observed that small Fe_2O_3 clusters and low Fe_2O_3 concentration can enhance the photocatalytic performance of TiO_2 while a large cluster size and larger concentration can hinder it. The DFT study of the particular system indicated the formation of type I heterojunction which was proposed to be the primary factor due to which the activity of the system was enhanced [41]. The structural, and electronic properties and charge transfer as well as magnetic properties of the created cluster-surface system were investigated for better understanding of the photocatalytic properties.

6.1 Computational details

We started to model the free hematite cluster. The $(Fe_2O_3)_1$ cluster was placed in a cubic simulation box with a side length of 20 Å. We ensured that there was enough space in all directions between the cluster in the simulation box and iits periodic images to prevent correlation. Due to the fact that the cluster does not have periodicity the Bloch theorem does not apply. Therefore, only one k-point, the Γ point, with k-point sampling of $1 \times 1 \times 1$ was included in the calculation.

Before the anatase TiO_2 surface, we checked the bulk state of it. We used a tetragonal unit cell containing 4 Ti and 8 O atoms (12 in total). Hubbard correction was employed for titanium because, similarly as Fe, it has localized d-electrons. Several U values are reported for the bulk TiO_2 and therefore, we tested the four different values (3.0, 4.5, 6.0 and 7.5

eV) to see the effect of the correction. For the bulk-TiO_2 k-point sampling of $9 \times 9 \times 4$ was used.

Next, we moved to simulate the anatase TiO_2 (101) surface using the supercell approach in which a slab, consisting of 4 layers, was enclosed in a supercell with the length of the lattice vectors of 10.32 Å, 15.25 Å and 35.68 Å in the x, y and z directions. The total number of atoms was 192: 64 titanium and 128 oxygen atoms. The rest of the supercell was vacuum whose thickness was around 20 Å. K-point sampling of $3 \times 2 \times 1$ was set.

The cluster-surface system was created by placing the $(Fe_2O_3)_1$ cluster on the surface of anatase. The combined system was denoted as $(Fe_2O_3)_1/TiO_2$. Similarly, calculation was performed for the cluster-surface system using the k-point sampling of $3 \times 2 \times 1$. The binding energy of the $(Fe_2O_3)_1$ cluster on the anatase (101) surface was computed from the formula

$$E_{\text{Bind}} = E((Fe_2O_3)_1/TiO_2) - E(TiO_2) - E((Fe_2O_3)_1), \tag{6.1}$$

where $E((Fe_2O_3)_1/TiO_2)$ is the total energy of the cluster-surface system and $E(TiO_2)$ and $E((Fe_2O_3)_1)$ are the total energies corresponding to the pristine anatase surface and the free $(Fe_2O_3)_1$ cluster, respectively.

The calculations were performed within both the GGA and the GGA+U. The Gaussian smearing with the width of 0.05 eV was employed to the calculations. The results from the GGA calculations were generally used to predict the geometries of the systems because it described it surprisingly well. Besides, we used the energies from the GGA for energy comparison, for example to calculate binding energies and work functions. The value of the total energy is generally not meaningful but the total energy difference between different systems is usually considered. The GGA+U, that takes the on-site Coulomb interaction between localized electrons into account, was used to predict the electronic properties as well as and magnetic properties of the systems investigated.

In addition, the recently developed exchange-correlation functional of DFT, the SCAN functional, was used to approximate the exchange and correlation effects. However, the SCAN functional caused several problems in the relaxation of the combined system of the TiO_2 surface and the Fe_2O_3 cluster. We did not obtain reasonable results for it and therefore we only present the SCAN results for TiO_2, for both the bulk and pristine surface. The other parameters were kept the same as in the GGA and the GGA+U calculations. The calculations were performed to see how the results compare between the GGA and the GGA+U, and the meta-GGA.

6.2 $(Fe_2O_3)_1$ cluster

We started by the simulation of the $(Fe_2O_3)_1$ cluster. The optimized structures and the labels of selected atoms are shown in Figure 9. The predicted structure agrees with the previously reported one [41]. The Fe-O bonds lengths obtained from the GGA and the GGA+U calculations were $1.65 - 1.87$ Å and $1.64 - 1.86$ Å, respectively. Two main differences between the structures were observed: the GGA+U predicted a longer distance of 2.55 Å between Fe atoms while the GGA predicted it to be 2.28 Å. Besides, the bond lengths of Fe2-O2 and Fe2-O3 were predicted to be shorter and Fe1-O2 and Fe1-O3 to be longer by the GGA+U. The GGA predicted contrariwise results. Related to the magnetic properties, the GGA predicted the local magnetic moments of Fe1 and Fe2 to be -1.83 μ_B and 3.00 μ_B, respectively. Opposite but unequal magnetic moments in magnitude imply

the $(Fe_2O_3)_1$ cluster to be ferrimagnetic. After applying the Hubbard correction, the result showed parallel arrangement of the magnetic moments of Fe atoms. The values of the magnetic moments were 3.629 μ_B for Fe1 and 3.396 μ_B for Fe2. The oxygen atoms have a small positive magnetic moment. It implies a small transfer of the magnetization from Fe atoms to O atoms. The magnetic moment of O3 was found to be 0.225 μ_B while it was 0.136 μ_B for O1 and O2.

The calculated DOS of the cluster is in Figure 10. It reveals discrete energy levels which is to be expected for the small cluster containing only five atoms. Even though that the cluster contains only five atoms, the DOS of it resembles somewhat the DOS of bulk α-Fe_2O_3 (Fig. 8b)). The partial DOSs of Fe and O atoms overlap, indicating 3d and 2p orbital hybridization. The DOS also upholds the parallel and large magnetic moments of Fe atoms, having an asymmetric spin splitting. The parallel arrangement of the Fe atoms in the $(Fe_2O_3)_1$ cluster has also been reported previously using DFT and hybrid functionals [97].

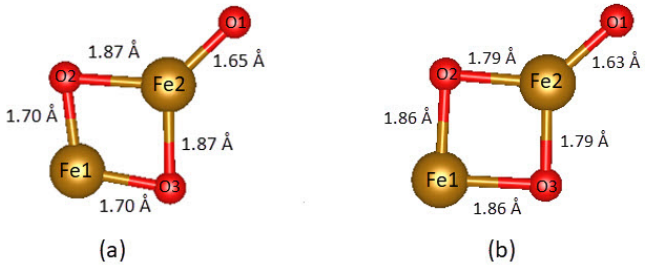

Figure 9: Optimized structure of the $(Fe_2O_3)_1$ cluster within a) the GGA and b) the GGA+U. The bond distances (Fe-O) are provided in Å. Iron atoms, labelled as Fe1 and Fe2, are marked as brown and oxygen atoms as red here and elsewhere.

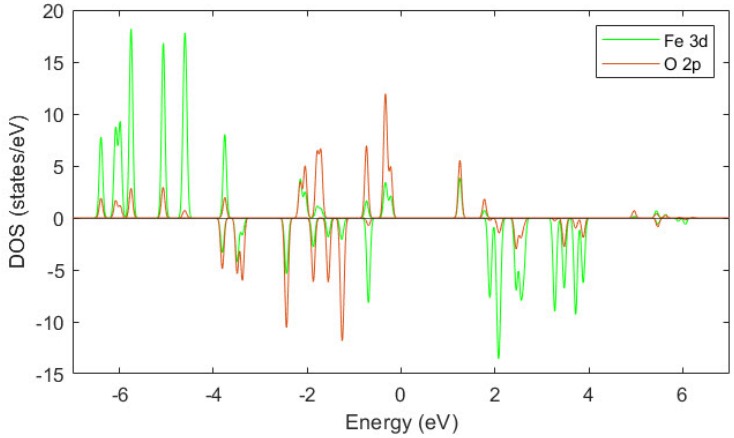

Figure 10: Partial density of states of Fe 3d orbitals and O 2p orbitals of the $(Fe_2O_3)_1$ cluster within the GGA+U. The Fermi level is set to zero here and in the rest of the DOSs.

6.3 Anatase-TiO_2

6.3.1 Bulk

We proceed to simulate the bulk TiO_2. The tetragonal unit cell of anatase is shown in Figure 11a). The unit cell was optimized within the GGA which yielded the lattice parameters $a = 3.81$ Å and $c = 9.75$ Å which are close to the experimentally determined values of $a = 3.78$ Å and $c = 9.51$ Å [98]. The calculated DOS of the bulk-TiO_2 is shown in Figure 11b). In this case the DOS is symmetric, showing correctly TiO_2 to be non-magnetic. The valence band is dominated by the O 2p states with a small admixture of Ti 3d states but the CB is mostly composed of Ti 3d states. Due to the fact that the Ti 3d and O 2p orbitals overlap with each other it indicates covalent nature for the bond between Ti and O atoms. The appearing shoulder feature in the conduction band edge is characteristic of anatase phase of TiO_2. However, similarly as in the case of hematite, the GGA also fails to predict the band gap of TiO_2, which was found to be 1.7 eV. This is due to the localized d-electrons of titanium. Bulk anatase has been found to have a band gap of 3.0-3.3 eV [8, 37, 41]. Therefore, we also applied the Hubbard correction to titanium in order to improve its electronic structure.

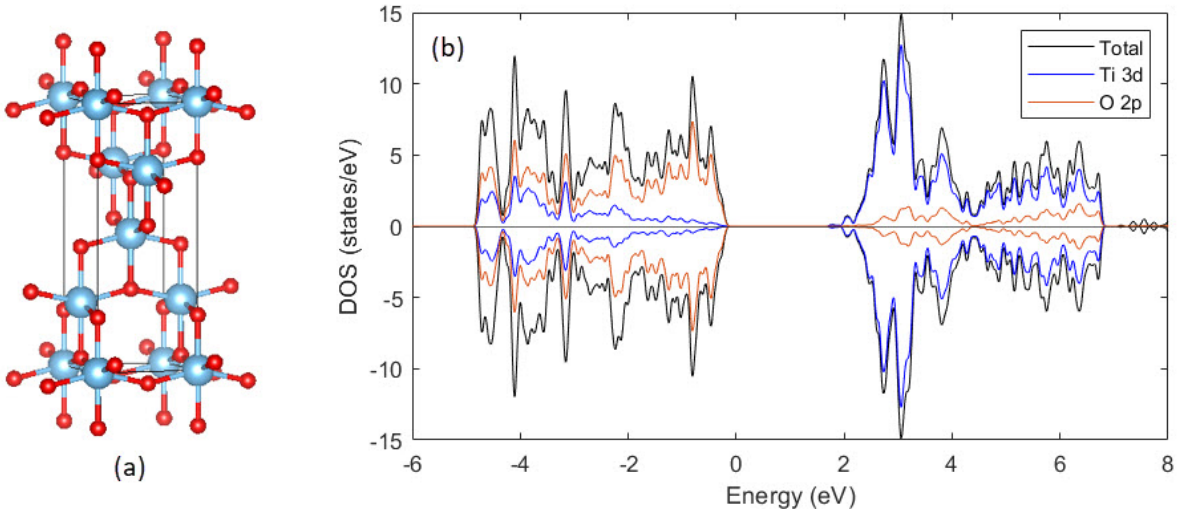

Figure 11: a) Unit cell and b) computed total DOS (black line) and partial DOSs of Ti 3d-states and O 2p-states (blue and red lines) of the bulk anatase TiO_2 surface. Titanium atoms are marked as blue and oxygen atoms here and elsewhere.

Several different U values were tested for TiO_2: 3.0, 4.5, 6.0 and 7.5 eV. In Table 1 are summarized the obtained lattice parameters and the band gap energy of each case and Figure 12 shows the computed DOSs. The band gap is improved by a larger U value. However, especially the shape of the conduction band of TiO_2 changes and the shoulder feature in the conduction band edge seems to gradually disappear. The Hubbard correction does not only affect the electronic structure but also the geometry. When U is increased the unit cell of TiO_2 expands. The lattice parameters become larger gradually. Thus, a larger Hubbard correction provides more realistic band gap but leads to a larger structural deviation. This is also noticed previously [99]. Although the band gap is still underestimated the Hubbard correction improves the description of TiO_2.

	a (Å)	c (Å)	E_g (eV)
U=3.0	3.88	9.71	2.1
U=4.5	3.91	9.73	2.3
U=6.0	3.94	9.78	2.6
U=7.5	3.97	9.81	2.9

Table 1: Lattice parameters and band gap energy E_g of bulk-TiO_2 calculated in different U values (eV).

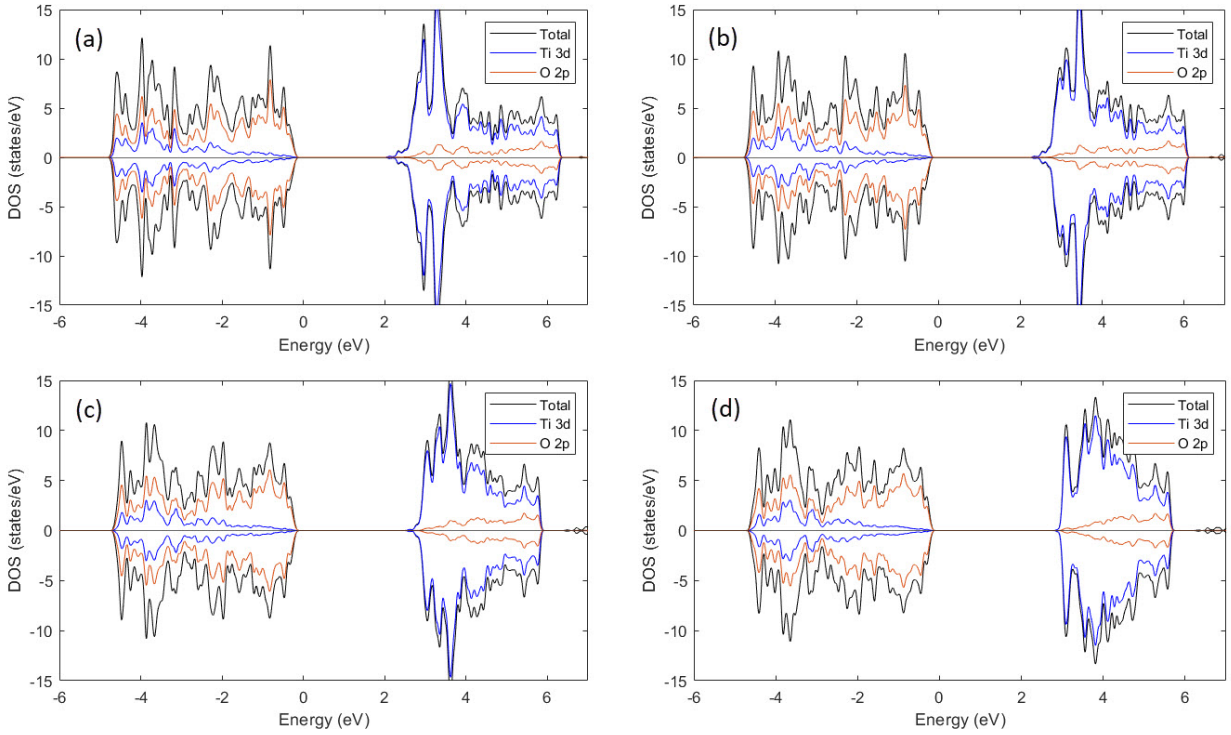

Figure 12: Density of states of the bulk-TiO_2 with a) $U = 3.0$ eV, b) $U = 4.5$ eV, c) $U = 6.0$ eV and d) $U = 7.5$ eV.

6.3.2 (101) Surface

We construct a pristine anatase TiO_2 (101) surface inside a supercell (Fig. 13a)). We chose a U value of 4.5 eV [100] for the surface. The particular value also improved the band gap of bulk-TiO_2 nicely and did not cause too significant deviation in the lattice parameters. The obtained DOS of the surface is shown in Figure 13b). The band gap energy was predicted to be approximately 2.5 eV. The valence band maximum (VBM) and the conduction band minimum (CBM) were -0.05 eV and 2.44 eV, respectively. The results have a good agreement with previous studies [41, 101]. The band gap energy is in the visible light region which indicates that the photoactivation of anatase surface could be achieved by visible light radiation with wavelength up to 500 nm. The particular wavelength corresponds to a light between blue and green colors. Due to the dangling bonds the surface band gap is generally smaller than the bulk band gap.

The work function of the pristine surface was calculated from Equation (4.6) and it was found to be 7.23 eV. Compared to the reported values our work function appears to be

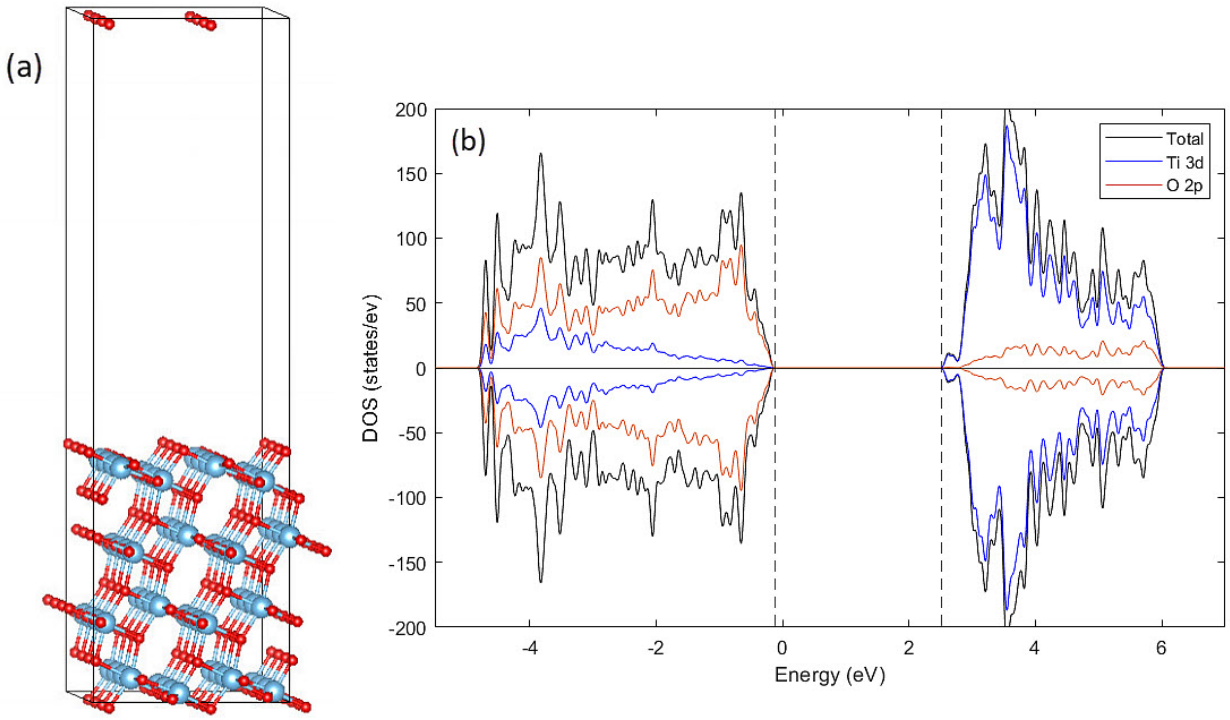

Figure 13: a) Supercell of anatase TiO_2 (101) surface. b) Computed total DOS (black line) and partial DOSs of Ti 3d-states and O 2p-states (blue and red lines) of the anatase TiO_2 surface. The oxygen atoms at the top of the supercell are periodic images.

relatively high [102]. Interestingly it differs from value calculated for the bulk. For the bulk TiO_2 we obtained the work function of 4.67 eV which in turn is comparable with the reported values.

6.3.3 TiO_2 and SCAN functional

After the GGA and the GGA+U calculations we switched and approximate the exchange-correlation functional by the SCAN functional, and simulate both the bulk TiO_2 and TiO_2 surface once again. We started with the bulk TiO_2 whose unit cell was visualized in Figure 11a). The lattice parameters were found to be $a = 3.78$ Å and $c = 9.67$ Å. These are in good agreement with the experimental results [98] and actually, they are closer to the experimental values than predicted by the GGA. It seems that the SCAN describes the geometry of the TiO_2 more accurately. The lattice parameter c is slightly overestimated but the parameter a corresponds to the experimentally determined value.

Besides, we calculated the density of states of both the bulk TiO_2 and the TiO_2 surface. They are shown in Figure 14. The DOS of the bulk TiO_2 predicted by the SCAN is very similar to the DOS predicted by the GGA (Fig. 11b)). However, the SCAN manages to describe the band gap considerably better than the GGA. We found the band gap of 2.2 eV. The U values of 3.0 eV and 4.5 eV yielded almost the same band gap than the SCAN functional (Table 1). The band gap is underestimated onward by the SCAN but compared to both the GGA and the GGA+U it succeeds better in the description of it. If taken the lattice parameters into account we could say that overall the SCAN is superior to the GGA

and the GGA+U in the case of the bulk TiO_2.

Conversely, in the case of the TiO_2 surface it seems that the GGA+U gives more realistic electronic structure for it (Fig. 13b) and Fig. 14b)). Firstly, the conduction band predicted by the SCAN differs from the prediction of the GGA+U. The characteristic shoulder feature is visible in the conduction band edge but SCAN predicts smaller amount of Ti states to be available in conducting. There exists also asymmetric feature in the top of the conduction band. Otherwise the DOS is symmetric. In spite of it, the TiO_2 was also correctly predicted to be non-magnetic by the SCAN. Secondly, the SCAN predicts smaller band gap of 2.3 eV for the TiO_2 surface. Generally, the surface band gap of TiO_2 is predicted to be around to 2.5 eV [41, 101]. If reflected to this the band gap of 2.3 eV is still a relatively good result. Nevertheless, the GGA+U seems to work slightly better in the case of the TiO_2 surface than the SCAN. It is better agreement with the previous studies.

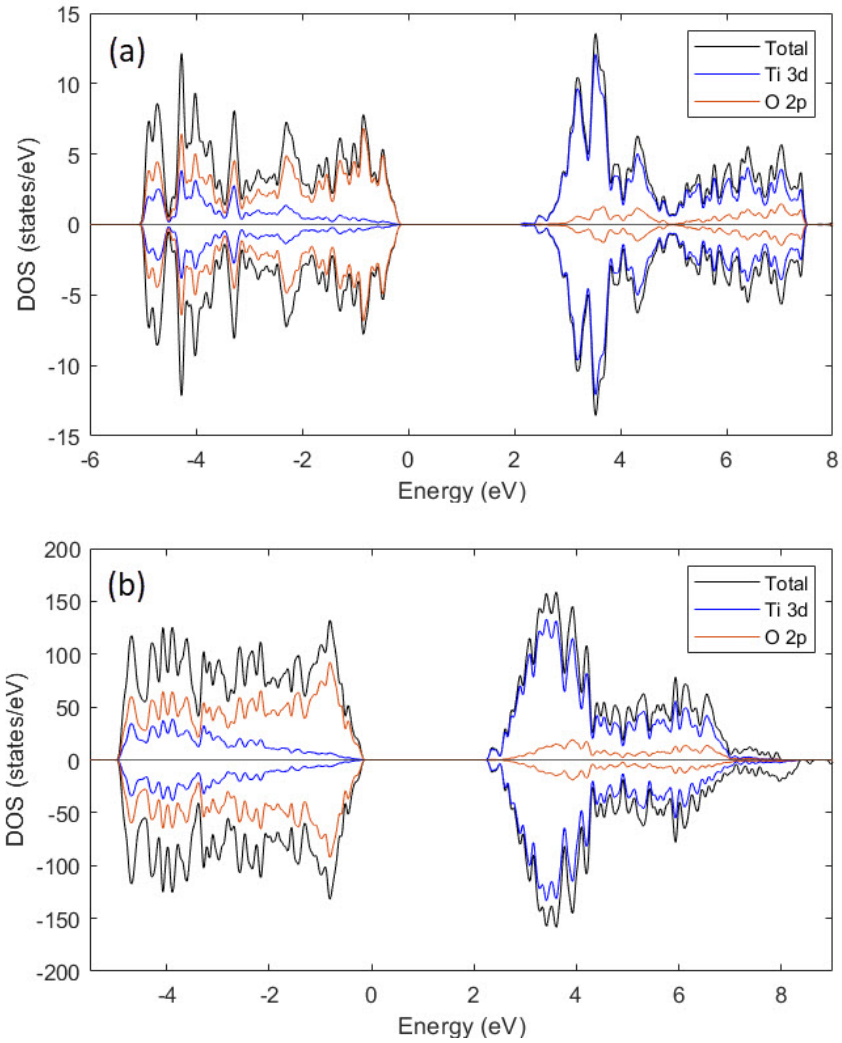

Figure 14: Computed total DOS (black line) and partial DOSs of Ti 3d states and O 2p states (blue and red lines) of a) the bulk anatase TiO_2 and b) pristine TiO_2 surface using the SCAN functional.

6.4 Cluster-surface system

The model of anatase TiO_2 surface with $(Fe_2O_3)_1$ cluster on the surface was implemented. The $(Fe_2O_3)_1$ cluster was placed on the surface of relaxed anatase in the supercell (Fig. 15a)) and the geometry of the combined system was optimized. The optimized structure of $(Fe_2O_3)_1/TiO_2$ is shown in Figure 15b). The labels of the selected atoms are also shown in the same figure. The cluster appears to be tightly bonded to the TiO_2 surface. Iron prefers to form bonds with oxygen at the surface to receive a half-filled configuration. The Fe1 atom is bonded to the O6 oxygen atom while the Fe2 atom is bonded to two, O4 and O5, oxygen atoms at the surface. The bond length for the Fe1-O6 bond was 2.04 Å. Fe3-O4 and Fe2-O5 bonds had the same length of 2.12 Å. Figure 15d) shows that the Fe atoms are arranged in line with each other along the x direction. O1, O2 and O3 oxygen atoms of the cluster form bridges between Fe atoms. O1 and O2 form two bridges almost horizontally and O3 in the direction of the xz-plane. The O3 atom is at the top of the pyramid-like structure of the cluster. When viewed along the y-axis, the outer shape of the cluster looks like a triangle (Fig. 15c)). If viewed from the top of the supercell the shape of kite was formed by Fe1, Fe2, O1 and O2 at the edges. The bond lengths were 1.88 Å for Fe1-O1 and Fe1-O2, 2.14 Å for Fe2-O1 and Fe2-O2, 1.99 Å for Fe1-O3 and 1.84 Å for Fe2-O3. In addition to Fe atoms, the O1 and O2 oxygen atoms formed bonds to the TiO_2 surface. They are bonded to Ti1 and Ti2 atoms with the same bond length of 1.94 Å. In total the $(Fe_2O_3)_1$ cluster was bonded to five atoms at the surface, resulting a coordination number of five for the cluster. Due to the absorption of the cluster the TiO_2 surface was slightly disordered. The cluster shifts few nearest Ti atoms at the top layer toward it. At the same time the oxygen atom right below the cluster (between Ti1 and Ti2 atoms) was shifted farther from it.

The binding energy of the $(Fe_2O_3)_1$ cluster to the surface was calculated according to Equation (6.1) and it was found to be -2.28 eV. Negative binding energy shows that the interaction between the TiO_2 surface and the Fe_2O_3 cluster is exothermic and thus energetically favourable. Thus, the cluster could spontaneously form bonds with the TiO_2 surface. The visualization revealed that the cluster remained stable (as a cluster) at the surface and essentially, the created combined system remained stable. Further, we calculated the work function to obtain more information on the interaction between the surface and the cluster. The adsorption of the cluster decreases the work function of the TiO_2 surface to 6.70 eV (from 7.23 eV). The change is not relatively large, approximately -0.5 eV, but it implies the cluster to act as an electropositive adsorbent in this case.

After optimizing the structure of the $(Fe_2O_3)_1/TiO_2$ we calculated its electronic structure. The DOS of the $(Fe_2O_3)_1/TiO_2$ is shown in Figure 16a). The PDOSs of Ti, Fe and O are shown in Figure 16b). The cluster did not change the overall DOS of the pristine TiO_2 surface. However, despite the low concentration and the small size of the Fe_2O_3 cluster, it still causes relatively notable changes in the total electronic structure. Looking at the Fe states, in the VB a larger portion of them have a spin up alignment. Especially below and at the bottom of the VB of TiO_2 a couple of large spin up peaks have been observed. One clear spin down peak is observed near the VB edge arising from the Fe2 atom. In the conduction band the majority of Fe states have a spin down alignment. The asymmetric spin splitting indicates a ferromagnetic ordering for the magnetic moments of Fe atoms and the appearance of spin polarization in the combined system due to the absorption of the Fe_2O_3 cluster (Fig. 16b, ii). A small overlapping of the Ti, Fe and O states (Fig. 16b))

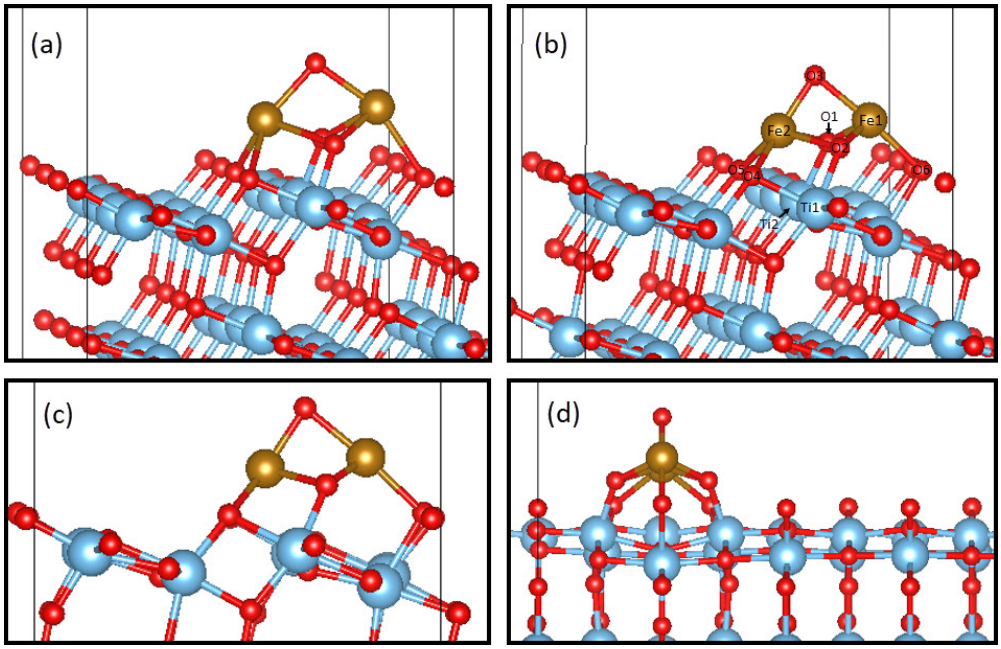

Figure 15: a) Initial structure of the $(Fe_2O_3)_1$ cluster on TiO_2 (101) surface placed inside the supercell. The cluster-surface system was created by attaching the $(Fe_2O_3)_1$ cluster was on the TiO_2 surface. The optimized structure of $(Fe_2O_3)_1/TiO_2$ is in b). In c) and d) the optimized structure is visualized along the y and x directions, respectively. The oxygen atoms at the top of the supercell are periodic images.

indicates a covalent character of the newly formed bonds.

The most interesting changes to the DOS appear in the band gap. Newly formed Fe 3d states with spin down alignment are observed just below the CB of TiO_2. These kind of states are generally called as shallow impurity states. Most of the impurity states close to VB of TiO_2 lie below the Fermi level (0 eV), thus being occupied. Small amount of localized and unoccupied impurity states with spin up alignment are induced at 0.45 eV, dominated by the Fe_2O_3-derived oxygen states. These states are located in the middle of the band gap of the $(Fe_2O_3)_1/TiO_2$. Instead of being shallow states these localized states might fall more probably into category of deep states, that exists further away form the VB and the CB edges.

Due to the generated impurity states the VB of Fe_2O_3 lies above the VB of TiO_2 and the CB of Fe_2O_3 below the CB of TiO_2 which could indicate the formation of a type I heterojunction with a straddling gap between TiO_2 and Fe_2O_3 [91]. This is in agreement with previously reported theoretical DFT studies [41, 49] and the performed experimental study also corroborates the formation of the particular heterojunction [103]. Generally, this allows electrons to be transferred from the CB of TiO_2 to the CB of Fe_2O_3 while holes can migrate from the VB of TiO_2 to the VB of Fe_2O_3. The newly formed states shifted the overall DOS of TiO_2 lower in energy. The VBM and the CBM of TiO_2 were found to be -0.75 eV and 1.92 eV, respectively, after the absorption of the $(Fe_2O_3)_1$ cluster. This does not change the band gap energy of TiO_2 but it is still 2.5 eV. Resulting from the impurity states the band gap of the total system, $(Fe_2O_3)_1/TiO_2$, is reduced manifestly. Thus, the interaction with the Fe_2O_3 cluster can help to expand the photoresponse of TiO_2 to cover

even larger portion of solar radiation. For comparison, the energy gap between the VB and the CB of Fe_2O_3 is around 1.35 eV, and the energy gap between the VB of Fe_2O_3 and the localized deep states is only approximately 0.5 eV.

To study further the interaction between TiO_2 and Fe_2O_3, the charge density difference (CDD) and the Bader charge analysis, and spin density difference (SDD) were calculated in order to understand charge transfer and charge distribution, and the magnetic phenomena in the system. In the charge density difference plot the yellow refers to charge accumulation and cyan refers to charge depletion while in the spin density difference plot the orange is for spin up polarization and turquoise for spin down polarization. We set the isosurface value to 0.005 e/Å. For the interpretation of the results from the Bader charge analysis we needed the knowledge that a negative Bader net atomic charge refers to electron gain and oppositely, positive charge to electron loss. The isosurface in CDD and SDD plots is more a point of view of both charge and spin densities, and therefore, Bader net atomic charges and magnetic moments are more quantitative measures.

The charge density difference and the Bader net atomic charges of selected atoms of the $(Fe_2O_3)_1$/ TiO_2 are shown in Figure 17. The CDD plot revealed that the main charge redistribution occurs at the cluster but also to a certain degree at the top of the surface and at the first sublayer. The oxygen atoms both in the Fe_2O_3 cluster and some at the TiO_2 surface are surrounded by yellow charge accumulation regions, implying oxygen generally to receive electrons in the system due to its electronegative nature. This is supported by the negative Bader charges of oxygen atoms. Iron atoms, on the other hand, are acting as electron donors, indicated by the blue isosurface around them and the positive Bader net atomic charges. Fe1 loses slightly larger amount of charge than Fe2. The relation of Bader charges and oxidation states is still somewhat debated and there is no clear justification how the Bader charge and the oxidation state are connected. However, the Bader net atomic charge of over 1.50 *e* could correspond a +3 oxidation state for iron [104]. In addition to Fe, atoms the CDD showed charge depletion regions at the top of the Ti atoms. Generally, Ti atoms in the system are acting as a electron donors, and the Bader net atomic charge of both Ti1 and Ti2 atoms was 2.06 *e*. It is suggested that the Bader net atomic charges of around 2.0 *e* could indicate the oxidation state of Ti being +4 or less [104].

In any case, redistribution of charge density was observed to occur in the combined system, and the adsorption of the cluster actually causes an appearance of net charge transfer of 0.32 *e* from the cluster to the surface. The main portion of the charge is transferred to the top layer of the surface, approximately 0.28 *e*. The direction is marked to Figure 17a) with a black arrow. The non-zero net charge transfer implies the interaction of TiO_2 and Fe_2O_3 to have ionic characteristic. Overall, the cluster is donating electrons for the TiO_2 surface and simultaneously the majority of holes are accumulating to the cluster which shows the electropositive nature for the $(Fe_2O_3)_1$ cluster. This was upheld by the work function. The adsorption of the cluster decreased the work function of the TiO_2 surface which is typical for an electropositive adsorbent.

If we consider TiO_2 and Fe_2O_3 separately, both being semiconductors, they can be excited and electron-hole pairs can be created. The band gap of TiO_2 being still 2.5 eV in the combined system only the shortest visible light wavelengths can excite electrons from the VB to the CB of TiO_2. Fe_2O_3 in turn can be activated more easily because of the smaller band gap between the VB and the CB of it. The Fe states in the CB edge lie below the CB of TiO_2, and therefore Fe can act as a trap for the photogenerated electrons from the VB of

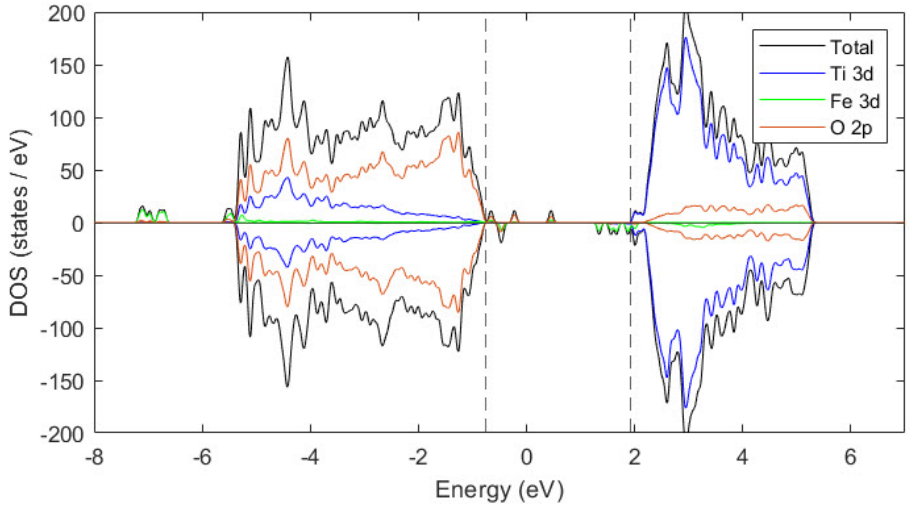

(a)

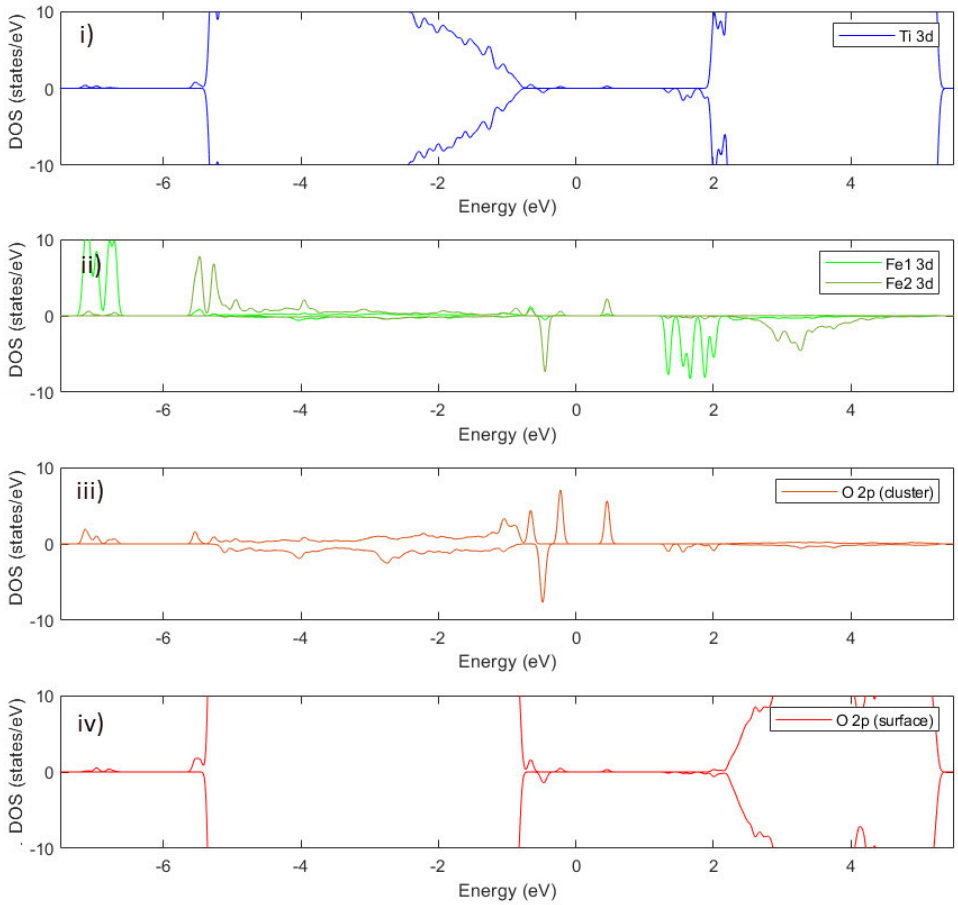

(b)

Figure 16: a) Density of states of the cluster-surface system. The total DOS is denoted by black line while partial DOSs of O 2p-states, Ti 3d-states and Fe 3d-states are represented as red, blue and green lines, respectively. Two dashed lines at -0.75 eV and 1.92 indicate the VBM and the CBM positions of TiO_2. b) The Partial DOSs of i) Ti states, ii) both Fe1 an Fe2 states and O 2p-states derived from iii) the Fe_2O_{31} cluster and from iv) the TiO_2 surface.

TiO_2. However, less electron excitations may be expected to occur form the VB of TiO_2 to its CB due to the larger band gap and therefore, there are fewer electrons to be trapped. On the other hand, Fe states can trap the excited electrons from the CB of TiO_2. However, if Fe traps an electron it loses its half-filled configuration $3d^5$ and become relatively unstable. Therefore, it tends to donate the electron and return to the half-filled configuration. Due to this the electrons from the CB of Fe_2O_3 could migrate to the CB of TiO_2. Simultaneously, the photogenerated holes are left to the VB of Fe_2O_3 while the electrons are accumulated to the CB of TiO_2. This could explain the observed direction of the charge transfer and the electropositive nature of the Fe_2O_3 cluster in the combined system. This would increase the n-type conductivity of TiO_2 and possibly the reduction ability of TiO_2. The oxidation reactions in turn take place most likely in the VB of Fe_2O_3.

The localized impurity states in the middle of the band gap of the $(Fe_2O_3)_1/TiO_2$ could act as a recombination center for the photogenerated electrons and holes. Deep states generally act as a recombination center because they can trap both electrons and holes from the VB and the CB, respectively. Alternatively it could enable another kind of recombination mechanism, for example so called Shockley-Read-Hall process in which the conduction band electron first relax to a deep state and after that to the valence band where the recombination then takes place [91]. Enabling the recombination of electrons and holes these states can affect negatively to the photocatalytic performance of the combined system. Fe_2O_3 has been proposed to become a recombination center at high dopant concentrations, leading to a reduction in photocatalytic performance [36]. Sun *et al.* made the same observation in their study of TiO_2 surface with Fe_2O_3 clusters [40].

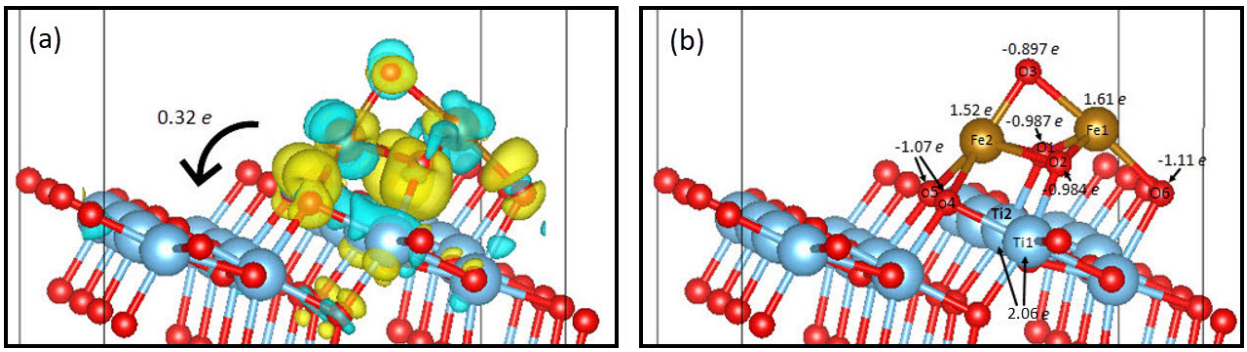

Figure 17: a) Charge density difference plot of the $(Fe_2O_3)_1/TiO_2$. The direction of the net charge transfer is indicated with a black arrow from the cluster to the surface. The Bader net atomic charges of selected atoms in the $(Fe_2O_3)/TiO_{21}$ are shown in b).

The directionality of charge density and accumulation of it in the newly formed bond between the surface and the cluster shows also the covalent bonding between the two systems. Because no nodes are observed, Fe1-O6, Fe2-O4 and Fe4-O5 bonds appear to be sigma bonds. The sigma bonds are most probably formed also between Ti1 and O2, and Ti2-O1. Due to the higher electronegativity, oxygen is pulling electrons stronger toward itself, and the expended yellow isosurface around O1 and O2 toward bond regions shows this.

The spin density difference plot of $(Fe_2O_3)_1/TiO_2$ is shown in Figure 18a). The spin density experiences also local changes. Fe atoms are mainly surrounded by the orange isosurface, indicating parallel magnetic moments for Fe atoms. The isosurface not having a shape of sphere shows the magnetic moments to be canted which also shows the net

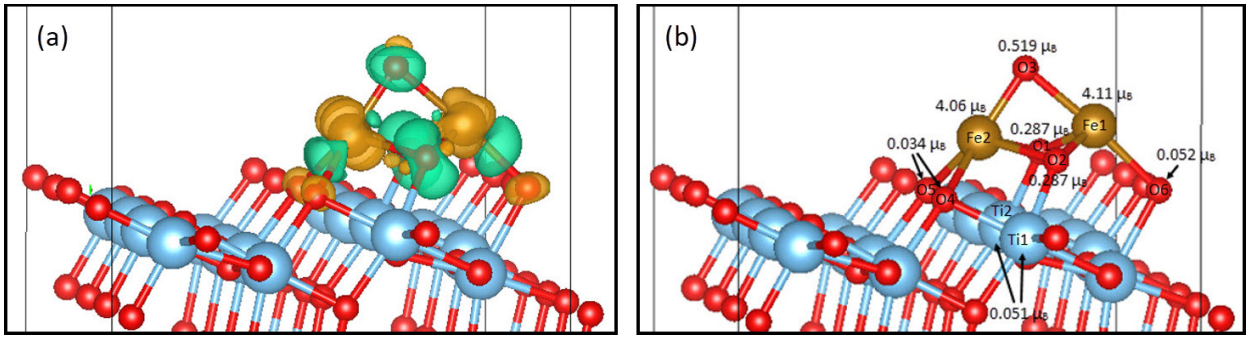

Figure 18: a) Spin density difference plot of the $(Fe_2O_3)_1/TiO_2$ and b) magnetic moments of selected atoms in the system.

magnetization to be non-zero in the system. The magnetic moments of Fe atoms were indeed found to be parallel with magnitude of 4.11 μ_B and 4.06 μ_B for the Fe1 and Fe2, respectively. Interestingly, the magnetic moments were almost as large as 4.328 μ_B which was predicted for Fe atom in a bulk α-Fe_2O_3. Already the asymmetric DOS (Fig. 16a)) revealed the cluster-surface system to be ferromagnetic due to Fe atoms. The magnetic moment of around 4 μ_B could correspond the half-filled Fe configuration $3d^5$ [105].

The ferromagnetic coupling of Fe atoms could be due to the superexchange phenomena [70] induced by the observed charge transfer. Fe_2O_3 was described as a charge transfer insulator and the charge transfer by hopping model [22]. The Fe atoms are connected to each other by three bridging O atoms and besides, they are bonded to O atoms at the surface. The Fe1-O1-Fe2 and Fe1-O2-Fe2 angles are 80° and Fe1-O3-Fe2 is 84° which are close to 90°. A bond angle approximately 90° predicts ferromagnetic coupling for the Fe cations. Fe 3d and O 2p orbitals can overlap with occupied or unoccupied ones. In the SDD plot O1 and O2 and O3 are mainly surrounded by blue isosurface, indicating more excess spin down polarization. The Pauli exclusion principle requires then the spins of Fe to be oriented parallel, resulting in a ferromagnetic coupling [106]. The overlap of the orbitals allows the charge transfer and also the transfer of magnetization. There could exist some magnetic coupling and therefore, the nearest atoms of iron receives a small positive magnetic moments.

Indeed, a small amount of magnetization was observed to be transferred to the nearby atoms of Fe, also to the surface atoms. The atoms at the TiO_2 surface to which the cluster is bonded to receive around or less than 0.050 μ_B while the O atoms of the cluster gain a positive magnetic moment of 0.287μ_B and 0.519 μ_B for O1 and O2, and for O3, respectively. We also observed localized blue isosurface in the middle of the newly formed bonds of Fe1-O6, Fe2-O4 and Fe2-O5. These excess spin down densities are originating from the cluster and correspond most probably to the impurity states observed in the CB edge in the DOS (Fig. 16a)). The amount of spin polarization spread around the rest of the atoms of TiO_2 is negligible.

The results showed that adsorbed $(Fe_2O_3)_1$ cluster remains stable on the TiO_2 surface and energetically favourable interaction between the subsystems. The coordination number of five indicated the cluster to be relatively tightly bonded to the surface. As was proposed in the previous study [41] the obtained results supported the formation of type I heterojunction between the two subsystems, TiO_2 and Fe_2O_3. The impurity state above the VB and

below the CB of TiO_2 reduce the the band gap of TiO_2 and expand the photoresponse of TiO_2. This can enhance the photocatalytic activity of TiO_2. The Bader charge analysis revealed a notable charge transfer occurring between TiO_2 and Fe_2O_3 which can affect the photocatalytic activity. The results indicate iron to act as electron donor in the combined system. Thus, the electrons appear to accumulate to the CB of TiO_2. In turn, the majority of holes are left to the VB of Fe_2O_3. It is possible that Fe acts as a electron trapper at some level in the system but overall, the electrons are accumulating to the CB of TiO_2. This is a contrary result to the studies of Sun *et. al.* [40] and Moniz *et. al.* [41]. Nevertheless, based on our results the electrons and holes accumulate to different subsystems which could lower the recombination rate by enhancing the charge separation. The existence of possible recombination center in the middle of the band gap of the combined system which can cause a reduction in the photocatalytic performance. Both the charge and spin densities experienced changes after combining the subsystems. Fe atoms are coupling ferromagnetically and Fe also induces spins on the nearby atoms of it, most likely due to the observed charge transfer.

7 Oxygen vacancy in the cluster-surface system

After simulating the defect-free $(Fe_2O_3)_1/TiO_2$ we studied the effect of oxygen vacancy in this system. The presence of oxygen vacancy in TiO_2 is known to provide effective excess charge for the system. Loss of one neutral oxygen atom provides two excess electrons that can reduce the oxidation state of Ti atoms, thus resulting Ti^{3+} species to charge compensate the system. The vacancy site itself has an effective positive charge. The electronic structure calculations have revealed localized Ti^{3+} states in the band gap region of TiO_2 as a result of oxygen vacancy [107, 108]. Due to the formation of localized states Li *et al.* observed the shift of Fermi level toward the conduction band and expansion of the photoresponse of TiO_2 into the visible light region due to the narrowing the band gap [107]. Oxygen vacancy is generally argued to improve the photocatalytic properties of TiO_2 by improving visible light response and charge transport and facilitating the charge separation of electrons and holes [109, 110]. However, introduction of oxygen vacancy may make it challenging to elucidate the primary reason for the improved photocatalytic performance [111].

At the surface of anatase TiO_2 oxygen atom has two coordination environments: twofold and threefold. Remove of either kind of oxygen atom changes the electronic structure of defect-free TiO_2 surface. The oxygen vacancy could provide more reactive sites for the photocatalytic reactions. However, the studies performed have suggested anatase to have inherently relatively low surface oxygen vacancy concentration. The subsurface vacancy has been found to be more stable in anatase [112, 113] which could explain the low surface vacancy concentration. Dangling bonds at the surface could also influence on the stability of the oxygen vacancy. In contrast, in rutile the surface oxygen vacancy has a lower formation energy.

In a recently published report, the interface of α-Fe_2O_3 (0001) and anatase TiO_2 was investigated [49]. The oxygen vacancy was found to be generally energetically less favourable than hydrogen defect at the TiO_2-Fe_2O_3 heterostructure. However, a more systematic study of the effect of oxygen vacancy to the photocatalytic mechanism of TiO_2-Fe_2O_3 heterostructure was not performed. We reduced one oxygen atom from the optimized $(Fe_2O_3)_1/TiO_2$ structure and tried to elucidate the effect of it to the combined system. It is possible to remove an oxygen atom from the TiO_2 surface or from the attached Fe_2O_3 cluster. Studying both, we try to elucidate whether the oxygen vacancy could be advantageous in order to improve the photocatalytic properties of TiO_2 and find a more preferable subsystem for the removing of an oxygen atom.

7.1 Computational details

We created an oxygen vacancy in the defect-free $(Fe_2O_3)_1/TiO_2$. We performed the follow-up calculations within the simulation supercell and with the computational parameters described in Section 6.1. The vacancy was located either in the TiO_2 or in the Fe_2O_3 cluster. The formation energy of the combined system with an oxygen vacancy is calculated using the following equation,

$$E_b = E((Fe_2O_3)_1/TiO_2\text{-}O_{vac}) - E((Fe_2O_3)_1/TiO_2) + \frac{1}{2}E(O). \quad (7.1)$$

$E(TiO_2/(Fe_2O_3)_1\text{-}O_{vac})$ is the total energy of the reduced system where O_{vac} specifies the created oxygen vacancy and $E(O)$ is the chemical potential of O that is half of the total

energy of an isolated oxygen molecule O_2. The value of the third term is thus -3.4257 eV. The formation energies are used to estimate the likelihood of the formation of the created oxygen vacancies. The isosurface value in the CDD and the SDD plot of the $(Fe_2O_3)_2/TiO_2$ was set to 0.005 $e/$Å. To be able to compare the CDD and the SDD plots of different systems we need to use the same isosurface value. Therefore, we also used the value of 0.005 $e/$Å for the isosurface in the following CDD and SDD plots.

7.2 Oxygen vacancy in the anatase surface

Several different oxygen vacancy sites locating in TiO_2 were created. In the first calculation the oxygen vacancy was located at the surface of anatase TiO_2. A twofold-coordinated oxygen atom was removed close to the cluster (Fig. 19a)) and it was labelled as O_v. The reduced cluster-surface system was relaxed within the GGA and the formation energy of the oxygen vacancy was calculated from Equation (7.1). It was found to be 3.41 eV. The positive value shows the creation of the oxygen vacancy to be endothermic and requires energy.

Because the formation energy of the surface oxygen vacancy was relatively high, larger than the band gap energy of bulk TiO_2, we also decided to create a subsurface oxygen vacancy on the first sublayer. Three different locations were chosen for the oxygen vacancy: one under the cluster and two farther away from it (Fig. 19b), c) and d)). The subsurface oxygen vacancies were labelled as O_{sv1}, O_{sv2} and O_{sv3}. Here the letter s denotes the subsurface.

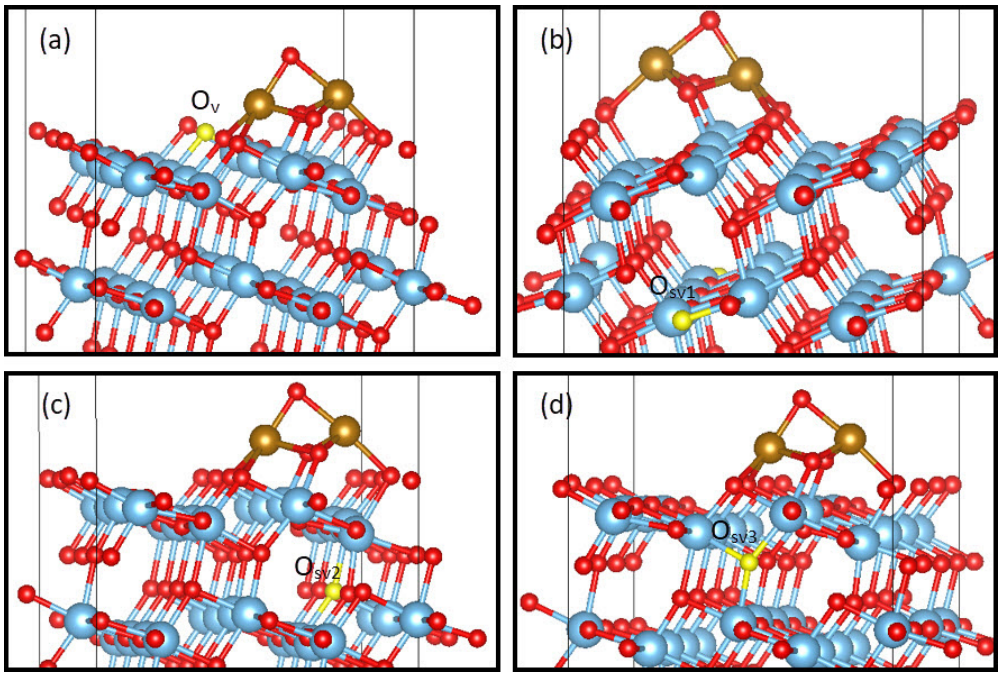

Figure 19: Locations of the surface and the subsurface oxygen vacancies in the $(Fe_2O_3)_1/TiO_2$ system. The created oxygen vacancy sites are coloured yellow.

The formation energies of all these four oxygen vacancies are tabulated in Table 2. Of the subsurface oxygen vacancies the most stable one is the O_{sv3} vacancy, with the lowest

formation energy of 2.71 eV. The subsurface vacancy site at the anatase surface seems to be more favourable in the $(Fe_2O_3)_1/TiO_2$ system. The formation energies are generally smaller compared to the surface oxygen vacancy O_v. Previous studies had also shown the oxygen vacancy to be more stable at the subsurface site in pristine anatase (101) surface [112, 113]. In addition, the formation energy of the subsurface vacancy site seems to depend on the distance from the Fe_2O_3 cluster at the TiO_2 surface. The O_{sv3} was the most stable oxygen vacancy, locating in the first sublayer closest to the cluster, right under the cluster. The other two subsurface vacancies O_{sv1} and O_{sv2}, of which O_{sv1} is the nearest and O_{sv2} is next nearest, were located farther from the cluster. The formation energy seems to be the lower the closer the subsurface oxygen vacancy site is to the cluster. The energy difference between the formation energies of O_{sv1} and O_{sv3} is almost 1 eV which is a relatively significant difference. Similar observation has been done previously by Hoh *et al.* when studying oxygen vacancies in α-Fe_2O_3(0001) surface with Au cluster on it [114]. Their results indicated the Au region at the surface to more stable against the reduction of oxygen atom. Correspondingly, the $(Fe_2O_3)_1$ cluster could stabilize the surface region under and close to it, thus reducing the formation energy of oxygen vacancy.

For comparison we simulated the same oxygen vacancy sites in the TiO_2 without the Fe_2O_3 cluster. The formation energies of each vacancy were over 5 eV (Table 2) and almost the same for each vacancy in the pristine TiO_2. From this we can conclude that the Fe_2O_3 cluster clearly reduces the formation energies of the oxygen vacancies in TiO_2, which is also generally observed [114, 115], and gives rise to the dependence of formation energies on the distance of a vacancy from the cluster on the surface.

Vacancy	E_{form} in the $(Fe_2O_3)_1/TiO_2$ (eV)	E_{form} in the TiO_2 (eV)
O_v	3.41	5.47
O_{sv1}	3.50	5.46
O_{sv2}	3.12	5.12
O_{sv3}	2.71	5.46

Table 2: The formation energies of the oxygen vacancy at the surface and different subsurface sites a) in the cluster-surface system and b) in the pristine TiO_2.

We chose to take the surface vacancy site, $(Fe_2O_3)_1/TiO_2$-O_v, and the most stable subsurface vacancy site, $(Fe_2O_3)_1/TiO_2$-O_{sv3}, for the further investigation to elucidate the effect of oxygen vacancy sites more.

7.2.1 Surface oxygen vacancy

The relaxed structure of the $(Fe_2O_3)_1/TiO_2$-O_v is shown in Figure 20. Th labels of the selected atoms are shown in Figure 20a). The presence of the oxygen vacancy changes the structure of the $(Fe_2O_3)_1$ cluster. The O3 atom at the top of the cluster still forms a bridge between Fe atoms. The Fe1-O3 and Fe2-O3 bond distances were 1.85 Å and 1.82 Å, respectively. However, O1 and O2 atoms form no longer bridges between the Fe atoms. They have moved below the Fe1, farther away from the Fe2 atom, shifting the Fe1 atom farther from the surface, in the direction of the z-axis (Fig. 20b) and c)). Therefore, the Fe1 atom is not directly bonded to the TiO_2 surface. Despite the changes, the Fe atoms remained in line with respect to each other in the direction of the x-axis (Fig.20c)). Fe1-O1

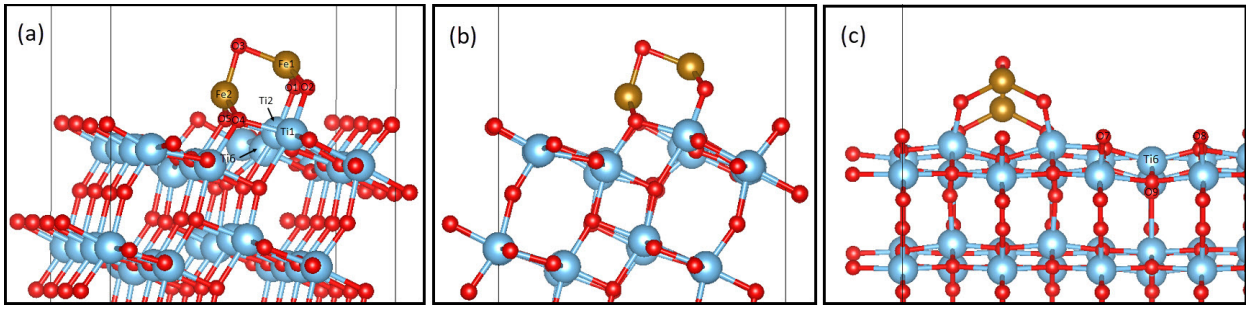

Figure 20: Optimized structure with the labels of the selected atoms of the $(Fe_2O_3)_1/TiO_2$-O_v is represented in a). b) and c) visualize the structure of the system along the y and x directions, respectively.

and Fe1-O2 bond lengths were 1.86 Å and 1.85 Å, respectively. The O1 and O2 are still bonded to Ti2 and Ti1 atoms at the surface with the bond length of 1.96 Å. Similarly, the Fe2 atom is bonded to O4 and O5 atoms with the same bond length of 1.80 Å. Again, distortion can be seen at the TiO_2 surface. The cluster pulls the Ti1 and Ti2 and a few nearest Ti atoms closer to itself and in addition, the oxygen vacancy shifts the neighbouring Ti atoms away from the vacancy site while the neighbouring oxygen atoms move slightly closer to the vacancy site. Similar changes have been observed in the studies of oxygen vacancies at the TiO_2 surfaces [100, 112]. Nevertheless, more lattice distortion is observed in this case due to the oxygen vacancy.

The calculated DOS of the $(Fe_2O_3)_1/TiO_2$-O_v is shown in Figure 21a. Again, the overall DOS of TiO_2 remains pretty much the same. However, it has been shifted downward in energy. The VBM of TiO_2 shifted from -0.76 eV to -0.96 eV and the CBM from 1.92 eV to 1.5 eV compared to the defect-free $(Fe_2O_3)_1/TiO_2$. The band gap of TiO_2 is still remaining around 2.5 eV. Localized state are no longer observed in the middle of the band gap. The impurity states are generated only at the VB and the CB edges which decrease the band gap energy of the combined system to 1.45 eV. This is slightly larger than that of the defect-free $(Fe_2O_3)_1/TiO_2$. However, it is still enough the system to cover all the visible light wavelengths. The oxygen vacancy does not change the band alignment of Fe_2O_3 and TiO_2. The CB of Fe_2O_3 lies below the CB of TiO_2 and the VB of Fe_2O_3 above the VB of TiO_2, therefore retaining the possible type I heterojunction between the subsystems.

In the VB edge, we observed the extended Fe_2O_3-derived states above the VB of TiO_2 but still below the Fermi level. Therefore, these states are occupied. With the sufficient energy the excitation can occur from both the VB of TiO_2 and Fe_2O_3. We also observed a large and localized Ti 3d peak at -0.57 eV, separated from the VB of TiO_2. This is arising from the Ti atom next to the oxygen vacancy site and the Fe_2O_3 cluster, labelled as Ti6 (Fig. 20a)). The oxygen peaks observed at the same energy region in Figure 21b, iv) are arising from the neighbouring oxygen atoms (O7, O8 and O9) of the Ti6 (Fig. 20c)). This Ti peak could correspond to the occupied polaron-like bound states localized on a single Ti site. Polaron is defined as a localized electronic states coupled with a strong lattice distortion. For example point-defects, like oxygen vacancies, are known to result in polarons in TiO_2 [108]. Localizing on Ti site next to the vacancy site indicates the polaron acts as an electron polaron which are identified as the reduction of a Ti^{4+} and existence of Ti^{3+} species in TiO_2 [107]. Below the CB of TiO_2 there are, once again, only unoccupied iron 3d states with

the spin down polarization available. Compared to the $(Fe_2O_3)_1/TiO_2$, the amount of these states is notably smaller. By introducing an oxygen vacancy some of the Fe 3d states seem to become occupied, indicating Fe and thus the $(Fe_2O_3)_1$ cluster to gain some amount of electrons.

The total DOS of the $(Fe_2O_3)_1/TiO_2$-O_v remains asymmetric due to iron. In the valence band a larger portion of the states have a spin up alignment but in the CB the iron states have spin down alignment (Fig. 21b, i)). This gives rise to ferromagnetism in the system, and further half-metallic behaviour for iron because only the spin down channel of it is available for conduction. If the top of the VB of TiO_2 is looked at closely one can see that it is not completely symmetric. It could indicate a larger induced magnetization in TiO_2 due to the introduced oxygen vacancy.

The CDD plot and the Bader net atomic charges of selected atoms of the $(Fe_2O_3)_1/TiO_2$-O_v are shown in Figure 22a). It is interesting that in the presence of the surface oxygen vacancy, according to Bader charge analysis, the direction of the net charge transfer changes, occurring from the surface to the cluster. Besides the direction of the charge transfer changed, also the amount of it reduced significantly. It was observed to be only 0.12 e (Fig. 22a)), approximately three times smaller than in the defect-free $(Fe_2O_3)_1/TiO_2$. The changes from the -0.32 e to 0.12 e is though relatively significant.

The Bader net atomic charges of Fe atoms have both become less positive. The charges change from 1.61 e to 1.52 e and from 1.52 e to 1.30 e for Fe1 and Fe2, respectively. In the CDD plot, Fe atoms are not just surrounded by the blue isosurface but also yellow isosurface. The Bader net atomic charge of Fe2 decreases more than of Fe1 which is supported by the CDD plot in which more yellow isosurface around Fe2 is observed. Therefore, Fe2 could be more likely in the 2+ oxidation state while Fe1 could be in 3+ oxidation state [104]. In addition, the oxygen atoms of the Fe_2O_3 cluster (O1, O2 and O3) has a slighly more negative Bader net atomic charges. If we compare the CDD plot to the SDD plot in Figure 23a) we find the following: where there is charge gain observed around Fe, the SDD plot reveals the excess spin down polarization in the same regions. The electrons Fe receives they most probably occupy the available spin down states in the CB which were observed less in the presence of the surface oxygen vacancy. Nonetheless, these indicates Fe_2O_3 truly gain electrons in this case.

The magnetic moment of Fe1 is still over 4 μ_B but for Fe2 it is 3.77 μ_B. SDD plot also shows that there is more turquoise but also orange isosurface around Fe2 while Fe1 is mainly surrounded by orange isosurface. When the Fe2 receives one electron, it has only four unpaired electrons in the 3d orbital which corresponds the +2 oxidation state. Due to the less amount of unpaired electrons, compared to the half-filled configuration, also the magnetic moment reduces. Magnetic moment of around 3.7 mu_B could indeed uphold the +2 oxidation state for the Fe2 [105].

The angle Fe1-O3-Fe2 is found to be 89° i.e. almost 90° and it could still convey the superexchange interaction and the ferromagnetic ordering of magnetic moments of iron [106]. However, the localized spin up isosurface is observed between the iron atoms in the SDD plot. Also in the CDD we can see how the yellow isosurface of Fe1 is directed toward the Fe2 and vice versa. Using a smaller isosurface value the isosurfaces connects between the iron atoms. In addition to superexchange interaction another process called double-exchange [117] can contribute to the magnetic coupling. In that case the extra electrons can hop from Fe2 to Fe1 but that requires the spins of electrons to be parallel. Therefore, some of

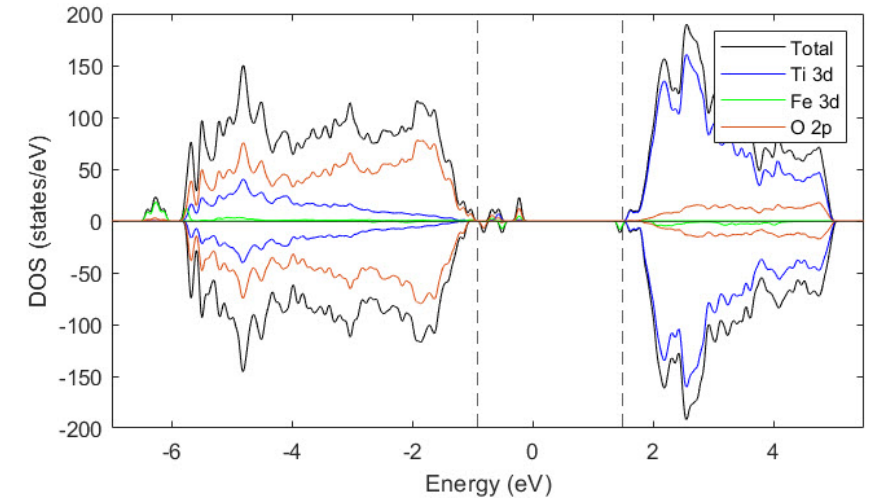

(a)

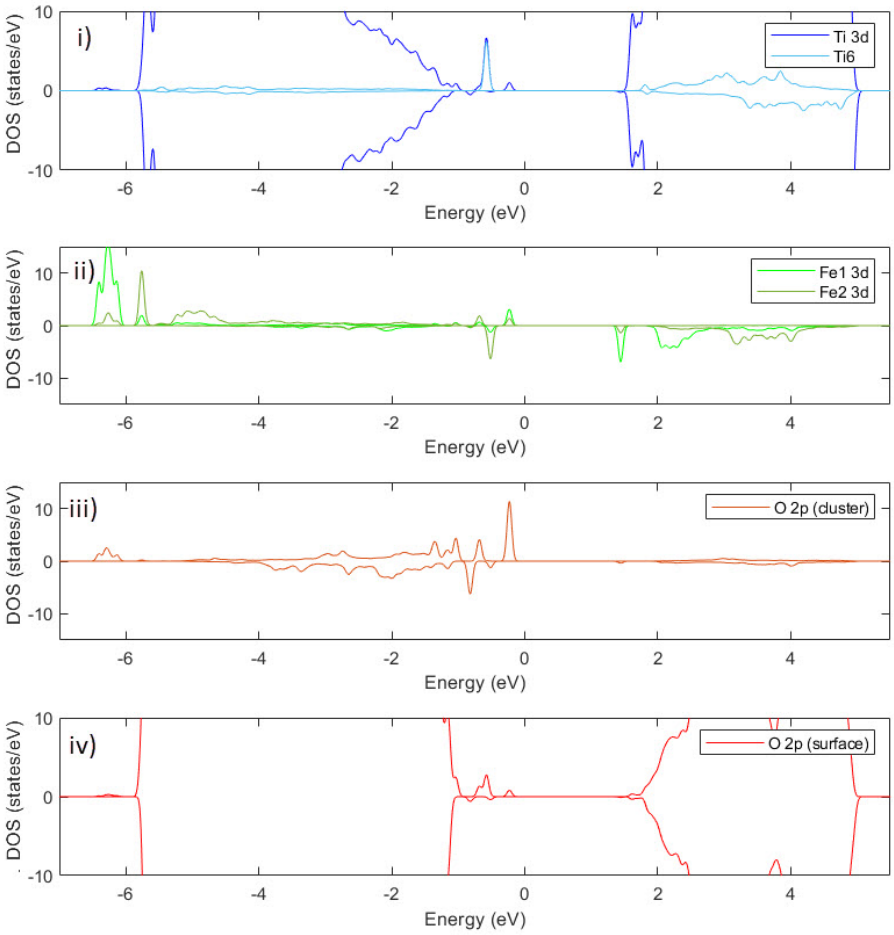

(b)

Figure 21: a) Overall density of states of the cluster-surface system in the presence of the surface oxygen vacancy O_v. The VBM and the CBM are indicated by dashed lines at -0.75 eV and 1.92 eV. b) The Partial DOSs of i) Ti states, ii) both Fe1 an Fe2 states and O 2p-states derived from iii) the Fe_2O_{31} cluster and from iv) the TiO_2 surface.

the electrons are delocalized between the iron atoms in the SDD. This hopping process is only possible between cations with different oxidation states, like between Fe^{2+} and Fe^{3+}. It could be a more prominent process than the superexchange in this case where the Fe atoms can have different oxidation states.

The Bader net atomic charges of Ti1 and Ti2 remain unchanged but that is not the case for Ti6 next to them. Without the oxygen vacancy its charge was 2.04 e but in the presence of oxygen vacancy it has decreased to 1.79 e. It could uphold the formation of electron polaron on the Ti6 site and the existence of Ti^{3+} species [104]. In addition to the notable decreased Bader net atomic charge Ti6 also gain a notable amount of magnetization, almost 1 μ_B. Both the charge and spin density of the total system revealed a localized charge and spin on the Ti6 site, respectively. However, the isosurface was observed on the Ti6 site neither in the charge nor spin density difference plots. This implies that this localized charge is redistributed in the system.

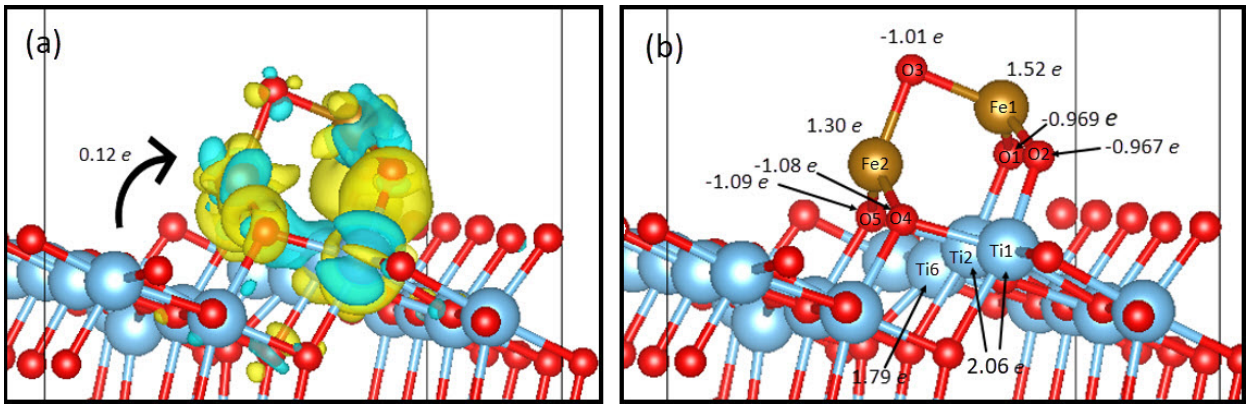

Figure 22: Charge density difference of the ($Fe_2O_{31}TiO_2$-O_v is a). In b) the Bader net atomic charges of selected atoms are shown.

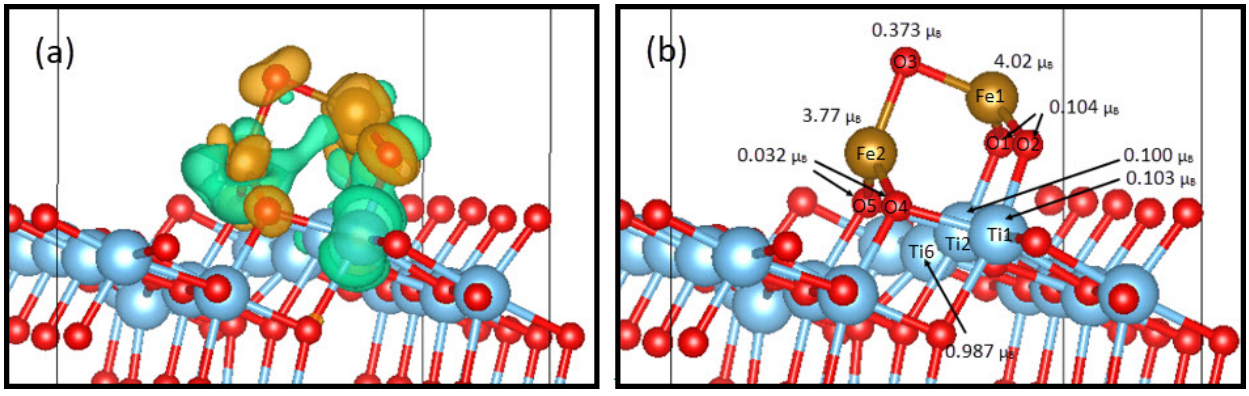

Figure 23: Spin density difference of the $(Fe_2O_3)_1TiO_2$-O_v with isosurface value of 0.005 e/Å is shown in a) and the magnetic moment of selected atoms in b).

In total the $(Fe_2O_3)_1$ cluster gained an amount of electrons while in TiO_2 the majority charge carriers are holes. The surface oxygen vacancy leave behind an effective excess charge which can change the concentration gradient and the direction of the charge transfer. It is still unclear what could be the primary charge transfer mechanism and is the surface

oxygen vacancy advantageous in order to improve the photocatalytic performance of TiO_2. The density of states revealed the possible type I heterojunction between the subsystems. Both the VB and the CB of the TiO_2 were altered by the impurity states. Compared to the defect-free combined system the band gap of it increased a little in the presence of surface oxygen vacancy. It still covers all the visible light wavelengths and is clearly narrower than of pristine TiO_2 surface. Therefore, we could conclude that the changed charge transfer properties are playing important role in the determination of the photocatalytic performance in this particular system.

7.2.2 The most stable subsurface vacancy

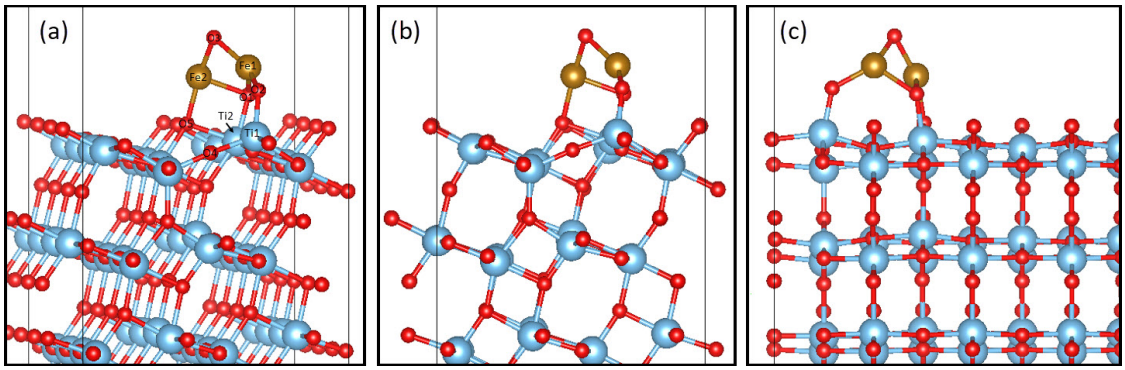

Figure 24: Relaxed structure of the cluster-surface system with the subsurface vacancy O_{sv3} from different side views, in b) along the y-axis and in c) along the x-axis. The labels of the selected atoms are shown in a).

The optimized structure of the $(Fe_2O_3)_1/TiO_2$-O_{sv3} and the selected and labelled atoms are shown in Figure 24. The most stable subsurface oxygen vacancy changes the geometry of the cluster drastically, although this could be expected because the particular vacancy was located just under the cluster. The cluster is only bonded to three atoms at the surface and its shape is curved. It looks concave when viewed from the vacancy site. It seems that the cluster may try to form a partial roof above the vacancy site. The vacancy shifted the Fe2 atom farther away due to which the Fe atoms are no longer in line in the direction of the x-axis (Fig. 24c)). Similarly as in the $(Fe_2O_3)_1/TiO_2$-O_v, the O1 and O2 atoms have moved to the same line with Fe1 in the direction of the z-axis (Fig. 24b)). The O1 and O3 form bridges between the Fe atoms with bond lengths of 1.98 Å for Fe1-O1, 2.10 Å for Fe2-O1, 1.85 Å for Fe1-O3 and 1.80 Å for Fe2-O3 but the Fe2-O2 and Fe2-O5 bonds were broken. O1 and O2 were bonded to Ti2 and Ti1 atoms with bond lengths of 1.86 Å and 1.79 Å, respectively. Once again, the cluster pulled the Ti1 and Ti2 atoms closer to itself and similarly as the surface oxygen vacancy, the subsurface oxygen vacancy shifted the adjacent Ti atoms away from the vacancy site while the adjacent oxygen atom moved little closer to the vacancy. Especially, the O4 atom was observed to shift notably toward the vacancy site. The distortion at the TiO_2 surface extend even to the third sublayer, slightly shifting the Ti atoms from their initial positions.

The DOS and the partial DOSs of the $(Fe_2O_3)_1/TiO_2$-O_{sv3} is shown in Figures 25a and 25b. Due to the subsurface oxygen vacancy the overall DOS of TiO_2 is shifted considerably lower in energy. The CBM is approximately only 0.73 eV away from the Fermi level.

Compared to the defect-free combined system the CBM has thus changed from 1.92 eV to 0.73 eV. Simultaneously, the VBM is shifted from -0.76 eV closer to -2 eV. It is hard to define the accurate VBM of TiO_2 because its VB edge is not totally symmetric due to changes the subsurface vacancy causes to the electronic structure.

While the VB of TiO_2 is pushed down in energy the Fe_2O_3-derived impurity states are extended upward of it. Most of the states are extended farther from the VB of TiO_2 and they are found in the range of -1 eV to 0 eV. These could be the extended Fe_2O_3-derived states in the CB edge in the $(Fe_2O_3)_1/TiO_2$ that become occupied, if Fe_2O_3 is gaining electrons, and are shifted downward below the Fermi level. Nevertheless, all the impurity state closer to the VB of TiO_2 are below the Fermi level and occupied. The bottom of the CB of Fe_2O_3 locates approximately at 1.5 eV at which there start to be available unoccupied iron and oxygen states. This kind of band alignment, in which the VB and the CB of the Fe_2O_3 lie above the VB and the CB of TiO_2, respectively, indicates a formation of a type II heterojunction between the subsystems, instead of a type I heterojunction, with a staggered gap. The band gap of TiO_2 is still around 2.5 eV but resulting from the impurity states and the shift of the DOS of TiO_2, the band gap energy of $(Fe_2O_3)_1/TiO_2$-O_{sv3} is reduced to 0.67 eV. This is way smaller than the band gap of pristine anatase TiO_2 surface. The optical absorption edge is thus shifted up to the short-wave infrared region (SWIR) but most essentially, the entire visible light range is covered.

Compared to the defect-free $(Fe_2O_3)_1/TiO_2$ and that in the presence of the surface oxygen vacancy, in which iron atoms have a ferromagnetic ordering, it is surprising that in the presence of the subsurface oxygen vacancy the iron atoms seems to have anti-parallel magnetic moments. In Figure 25b, ii) are shown the partial DOSs of Fe1 and Fe2 atoms. Their partial DOSs are, again, resembling somewhat the partial DOS of iron observed in the bulk-Fe_2O_3 but while the majority of spin up state of Fe1 locates in the VB and the majority of spin down state in the CB, this is opposite for Fe2. It implies that Fe2 is in an anti-ferromagnetic state [118], resulting in an anti-parallel ordering for the magnetic moments of iron. The spin up and down components are not totally symmetric but it is not clear from the DOS whether the anti-parallel magnetic moments cancel each other or is the system ferrimagnetic.

We found the magnetic moments of 3.62 μ_B and -3.57 μ_B for Fe1 and Fe2, respectively, confirming that the system indeed is ferrimagnetic and the subsurface oxygen vacancy O_{sv3} induces the magnetic phase transition in Fe2. The magnetic moments do not completely cancel each other, thus resulting in a small positive but almost zero magnetic moment for the total combined system. To qualitatively investigate the magnetic properties the spin density difference plot of the $(Fe_2O_3)_1/TiO_2$-O_{sv3} was calculated and it is shown in Figure 26a). Both orange and turquoise isosurfaces are seen around Fe atoms. Where there is a charge gain in the CDD plot (Fig. 27a)), there is a excess number of spin down electron in the SDD plot and vice versa, the excess spin up electrons are seen in the same locations as the depletion region in the CDD plot, meaning the donated electrons of iron are from spin up states while gained electrons will have spin down orientation. Therefore, the gained electrons most probably occupy the available Fe states in the CB edge of the defect-free $(Fe_2O_3)_1/TiO_2$.

In the SDD plot the O1, O2, Ti1 and Ti2, on the other hand, are surrounded completely by turquoise isosurface in the SDD plot, showing en excess spin down polarization on these sites. The Bader net atomic charges of Ti1 and Ti2 decrease from 2.06 e to 2.01 e and to

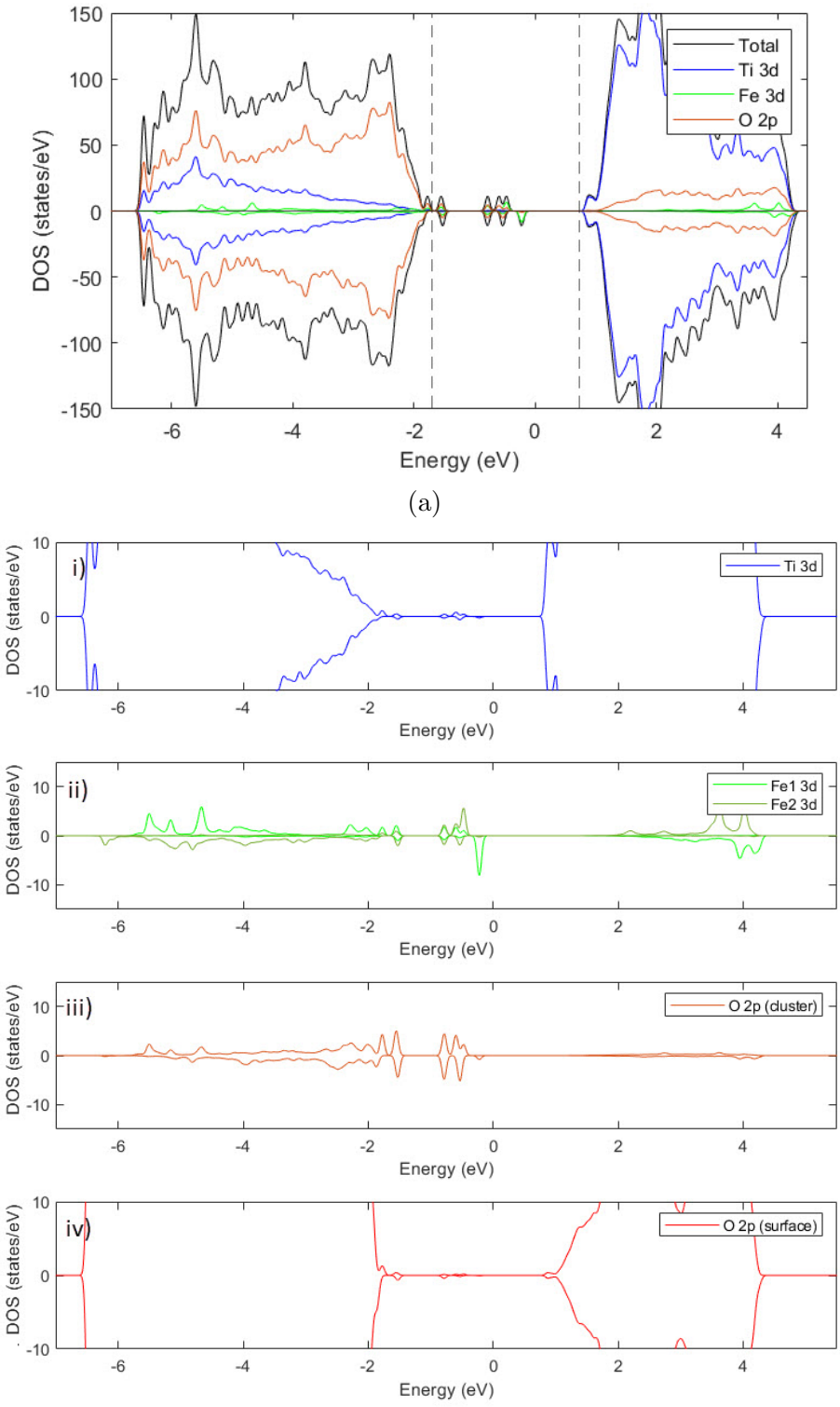

(a)

(b)

Figure 25: a) Overall density of states of the cluster-surface system in the presence of the most stable subsurface oxygen vacancy O_{sv3}. The VBM and the CBM are indicated by dashed lines at around -1.7 eV and 0.75 eV. b) The Partial DOSs of i) Ti states, ii) both Fe1 an Fe2 states and O 2p-states derived from iii) the Fe_2O_{31} cluster and from iv) the TiO_2 surface.

2.04 e, respectively, which supports the small amount of gain of electrons. The magnetic moments were 0.072 μ_B for Ti1 and 0.033 μ_B for Ti2. Differing from the previous investigated systems the O1, O2 and O3 but also the O4 and O5 at the TiO_2 surface have a negative but almost non-zero magnetic moment. The magnetic moment of the O1 is 0.02 mu_B while for the rest have a magnetic moment of -0.006 μ_B or smaller.

The observed lattice distortion could be the primary reason for the observed magnetic phase transition. The bond lengths of Ti1-O2 and Ti2-O1 have been shorten due to the oxygen vacancy. These are the bonds that are surrounded completely by the turquoise isosurface in the SDD plot. The magnetization could been restored on these atoms and bonds which would leads to antiferromagnetic state for Fe2, and ferrimagnetic ordering of iron atoms [119].

The total Bader net atomic charge of the subsystems revealed the net charge transfer from TiO_2 to Fe_2O_3 (black arrow in Fig. 27a)), similarly as in the presence of the investigated surface oxygen vacancy. The amount of charge transfer was found to be 0.62 e from the Bader charge analysis. Again, the top layer of TiO_2 participates the most to the charge transfer. Compared to the defect-free $(Fe_2O_3)_1/TiO_2$ the amount of charge transfer is almost two times higher, although the direction is reversed. The larger charge transfer could indicate more stronger and ionic interaction for the subsystems. The larger net charge transfer also agrees with the lower formation energy of this subsurface oxygen vacancy. Its formation energy was approximately 0.8 eV lower than that of the surface oxygen vacancy.

The Bader net atomic charges of O1 and O2 remain almost unchanged but O3 gain larger amount of electrons and its Bader net atomic charge is almost -1.1 e. Iron atoms are gaining electrons also in the presence of the particular subsurface oxygen vacancy but clearly higher amount than in the presence of the surface oxygen vacancy. Their Bader net atomic charges decrease to 1.26 e for Fe1 and 1.19 e for Fe2. In this case both Fe atoms could be in the 2+ oxidation state [104]. The electrons occupy the empty iron state observed in the CB of Fe_2O_3(Fig. 16b, ii)) due to which the band alignment of the CB of TiO_2 and Fe_2O_3 then changes.

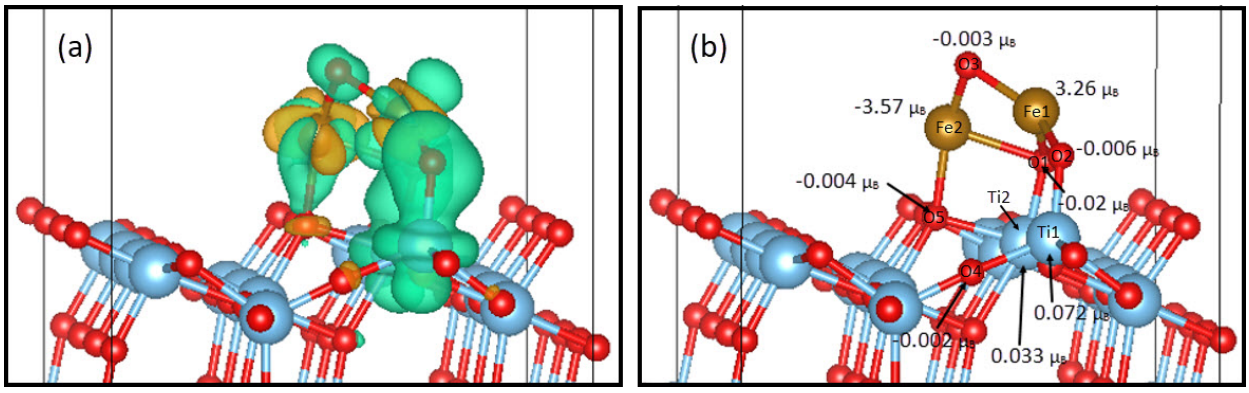

Figure 26: a) Spin density difference plot with the isosurface value of 0.005 e/Å and b) magnetic moments of selected atoms of the $(Fe_2O_3)_1/TiO_2/\text{-}O_{sv3}$.

The DOS indicated the formation of a type II heterojunction between TiO_2 and Fe_2O_3 which could allow electrons to be transferred from the CB of Fe_2O_3 to the CB of TiO_2. However, the direction of the net charge transfer from the Bader analysis implies that this may not be the case. The individual band gap of TiO_2 and Fe_2O_3 were found to be around

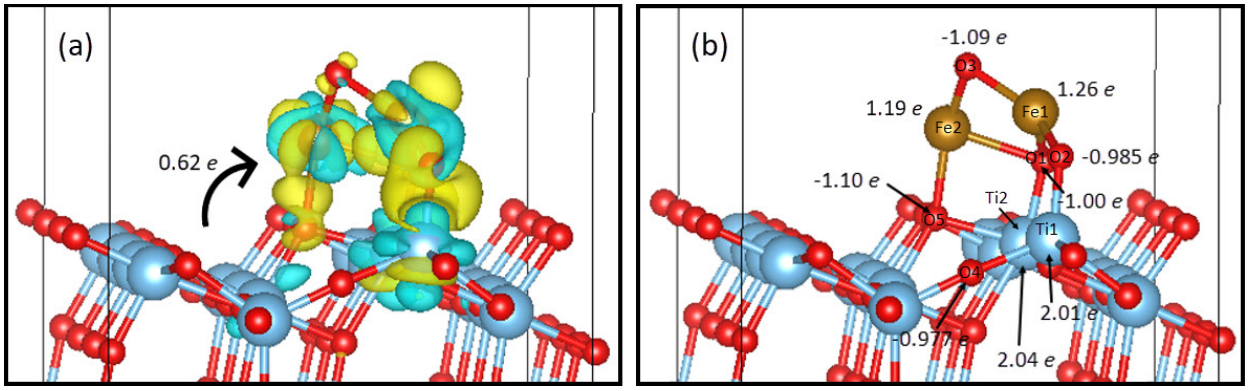

Figure 27: a) Charge density difference plot with the isosurface value of 0.005 e/Å and b) Bader net atomic charges of selected atoms of the $(Fe_2O_3)_1/TiO_2/\text{-}O_{sv3}$.

2.5 eV and 2.0 eV so in both cases electrons can be excited to the conduction bands of the systems by visible light, TiO_2 with wavelength up to 500 nm and Fe_2O_3 with wavelength up to 620 nm. The CB's of TiO_2 and Fe_2O_3 locate relatively far away from each other and the CB of TiO_2 actually locates closer to the VB of Fe_2O_3. Correspondingly, the VB of Fe_2O_3 is closer to the CB of TiO_2 than to the VB of TiO_2. It could be easier for electrons to relax and transfer from the CB of TiO_2 to the VB of Fe_2O_3 due to the existence of higher driving force that originates from the higher potential difference. These transferred electrons recombine with the holes left in the VB of Fe_2O_3 after electron excitations. The combined system could, thus, primarily act as a direct Z-scheme photocatalyst, in which the electrons are then accumulating to the CB of Fe_2O_3 and holes to the VB of TiO_2 [91]. Like a type II heterojunction the Z-scheme heterojunction also provides the spatial separation for the charge carrier. The Z-scheme heterojunction is generally a more convenient way to separate the electrons and holes into the different locations. This is due to the strong electrostatic attraction between electrons and holes. This could efficiently suppress the recombination of the charge carriers by increasing their lifetime. In the type II heterojunction both electrons and holes are transferred to the locations where there already exist electrons or holes. Therefore, it could be more difficult to transfer charge carriers in the particular heterojunction due to the electron-electron and hole-hole repulsion [91].

As a summary, the most stable subsurface vacancy introduces significant lattice distortion in the TiO_2 surface and changes in the geometry of the cluster. As in the presence of the investigated surface oxygen vacancy, the direction of the charge transfer was toward the Fe_2O_3 cluster. The DOS indicated the formation of a type II heterojunction between the subsystems. However, because the VB of Fe_2O_3 and the CB of TiO_2 located closest to each other, the Z-scheme mechanism could be responsible for the charge transfer in the system. It leads to electron accumulation to the Fe_2O_3 and hole accumulation to the TiO_2 surface, oppositely as in the defect-free combined system. Therefore, we could suggest that the Fe_2O_3 is primarily participating to the reduction reactions while TiO_2 has the excess of holes that could initiate oxidation reactions. Therefore, oxygen vacancy can be used to increase to oxidation ability of TiO_2. With highly reduced band gap this could efficiently decrease the recombination rate and improve the photocatalytic activity of TiO_2. In the previous case the iron atoms had a ferromagnetic ordering. However, the investigated subsurface oxygen vacancy surprisingly induced a magnetic phase transition of the other iron atom. The most

probably reason for this is the observed notable lattice distortion. The magnetic moments of iron atoms oriented anti-parallel but did not cancel each other completely, leading to a small ferrimagnetism in the combined system. We may not be able to say what is the primary mechanism leading to the magnetic phase transition and what is the deepest influence of it on the photocatalytic performance based on these results. Therefore, further studies are needed to be performed to understand its role better.

7.3 Oxygen vacancy in the cluster

Alternatively, instead of removing oxygen atom from the TiO_2 surface we removed it from the adsorbed Fe_2O_3 cluster. The oxygen atom at the top of the $(Fe_2O_3)_1$ cluster, labelled as O3 in Figure 15, was removed (Fig. 28). The reduced system was labelled as $(Fe_2O_2)_1/TiO_2$.

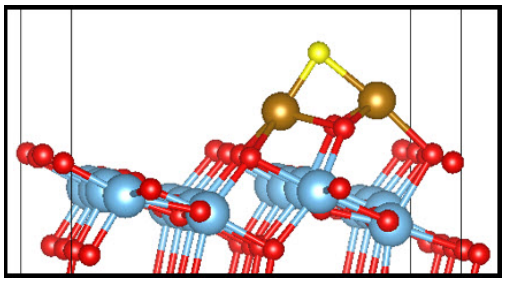

Figure 28: Oxygen vacancy locating at the Fe_2O_3 cluster in the $(Fe_2O_2)_1/TiO_2$ system. The created oxygen vacancy site is coloured yellow.

We calculate the formation energy from Equation (7.1) and it was found to be 1.59 eV. Compared to the formation energies of the oxygen vacancies created in TiO_2 the required energy to remove the O3 atom from the cluster is clearly smaller, and thus the vacancy is easier to create. The required energy is over 1 eV lower than that needed to create the most stable oxygen vacancy in the TiO_2 (Table 2). The reason for this could be simple. In the TiO_2 both surface and subsurface vacancies are more bonded, not only to atoms in their own layer but also to those directly beneath and above them in the sublayers, whereas the O3 atom is held in the cluster-surface system only by the two Fe atoms. Therefore, oxygen is easier to remove from the adsorbed cluster than from the surface.

The optimized structure of the $(Fe_2O_2)_1/TiO_2$ is in Figure 29. Overall, the structure resembles the $(Fe_2O_3)_1/TiO_2$, expect for the missing O3 oxygen atom. Two remaining oxygen atoms O1 and O2 are at bridges between the Fe atoms with bond lengths of 1.89 Å for Fe1-O1 and Fe1-O2, and 2.05 Å for Fe2-O1 and Fe2-O2. In the xy-plane these four atoms form a shape of a kite. Fe atoms are slightly closer to the surface. The bond lengths between Fe1 and O6, and Fe2 and O4 and O5 were 1.86 Å and 1.96 Å while O1 and O2 have been shifted up to the same level as the Fe atoms. Therefore, the top of the cluster is almost flat (Fig. 29b)), forming a small plane above the TiO_2 surface. Both the Ti1-O2 and Ti2-O1 bonds were found to be 1.94 Å.

We were also interested to see the result if either of O1 or O2 atoms were removed instead of O3. The calculations yielded identical results to removing the O3 atom. When removing O1 or O2, the O3 atom shifts to the position of it and the same optimized structure was obtained. Therefore, it seems that there is no matter which one of the three oxygens of the

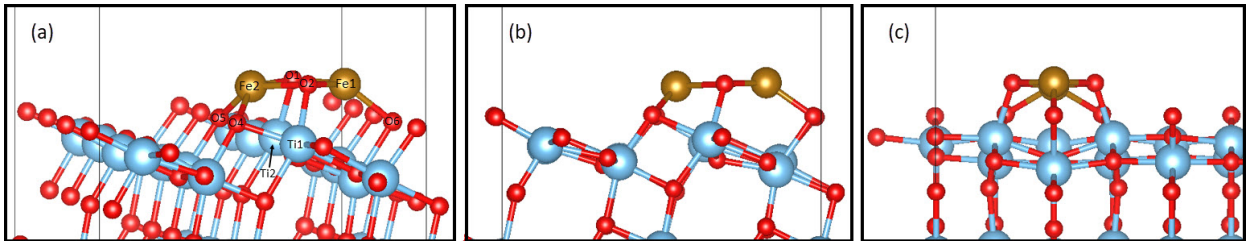

Figure 29: Relaxed structure of the $(Fe_2O_2)_1/TiO_2$ is visualized and selected atoms of the system are labelled in a). The structure of the system is also visualized from the different side views, along b) the y and c) the x directions.

$(Fe_2O_3)_1$ cluster is removed. The final geometry of the cluster and also of the total combined system were the same as shown in Figure 29.

The total DOS and partial DOSs of the elements of $(Fe_2O_2)_1/TiO_2$ were calculated to investigate the electronic structure and they are shown in Figure 30a) and 30b). Within the band gap of TiO_2 the Fe_2O_3-derived impurity states are observed only above the VB of TiO_2 but still below the Fermi level. The impurity states are separated from the VB of TiO_2 by a small gap of 0.17 eV. There are no extended impurity states below the CB of TiO_2 but the CBM of Fe_2O_3 is approximately at 2.0 eV, above the CBM of TiO_2. The VBM and the CBM of TiO_2 are around -0.85 eV and 1.69 eV, respectively, resulting in a band gap of around 2.5 eV for TiO_2. Compared to the defect-free $(Fe_2O_3)_1/TiO_2$, also in this case the overall DOS of TiO_2 is shifted a little bit lower in energy. The observed band alignment of TiO_2 and Fe_2O_3, that VB of Fe_2O_3 lies above the VB of TiO_2 and the CB of Fe_2O_3 above the Cb of TiO_2, indicates a formation of a type II heterojunction between the two subsystems. The band gap of $(Fe_2O_2)_1/TiO_2$ was found to be 1.8 eV. Thus, this system has the highest band gap energy of all the systems already studied in this thesis. The DOS is again asymmetric due to iron, resembling the DOS of bulk-Fe_2O_3 (Fig. 8) and showing a ferromagnetic nature for the $(Fe_2O_2)_1/TiO_2$. Because iron has only spin down channel available in the conduction band it indicates a half-metallic behaviour for it, similarly as in the case of the investigated surface oxygen vacancy.

The charge density difference of $(Fe_2O_2)_1/TiO_2$ is shown in Figure 31a). It is very similar to the CDD plot of the $(Fe_2O_3)_1/TiO_2$. The charge is mainly redistributed in the cluster but again to a same extent at the TiO_2 surface. According to the Bader charge analysis the direction of the charge transfer retains from the cluster to the surface, as in the defect-free $(Fe_2O_3)_1/TiO_2$. However, the amount of charge transfer is almost one and a half times larger, 0.45 e, in this case. The depletion is observed from the top of the cluster, where the oxygen was removed. The Bader net atomic charges revealed that both the Fe atoms and the O1 and O2 of the cluster gain electrons (Fig. 31b)), indicating that part of the excess charge provided by the oxygen vacancy is going to the cluster. The Bader net atomic charges of Fe1, Fe2, O1 and O2 change from 1.61 e to 1.29 e, from 1.58 e to 1.32 e, form -0.987 e to -1.07 e and from -0.984 e to 1.08 e, respectively, when compared to the $(Fe_2O_3)_1/TiO_2$. For iron the particular value could imply a 2+ oxidation state [104].

The Bader net atomic charges of the atoms at the surface, to which the cluster is bonded to, are not generally changing but overall, the top of the TiO_2 surface gain more charge, approximately 0.4 e i.e. almost all of the transferred charge. The rest of the charge is going to sublayers, mostly to the first sublayer. The shape of the isosurface, the four-lobes

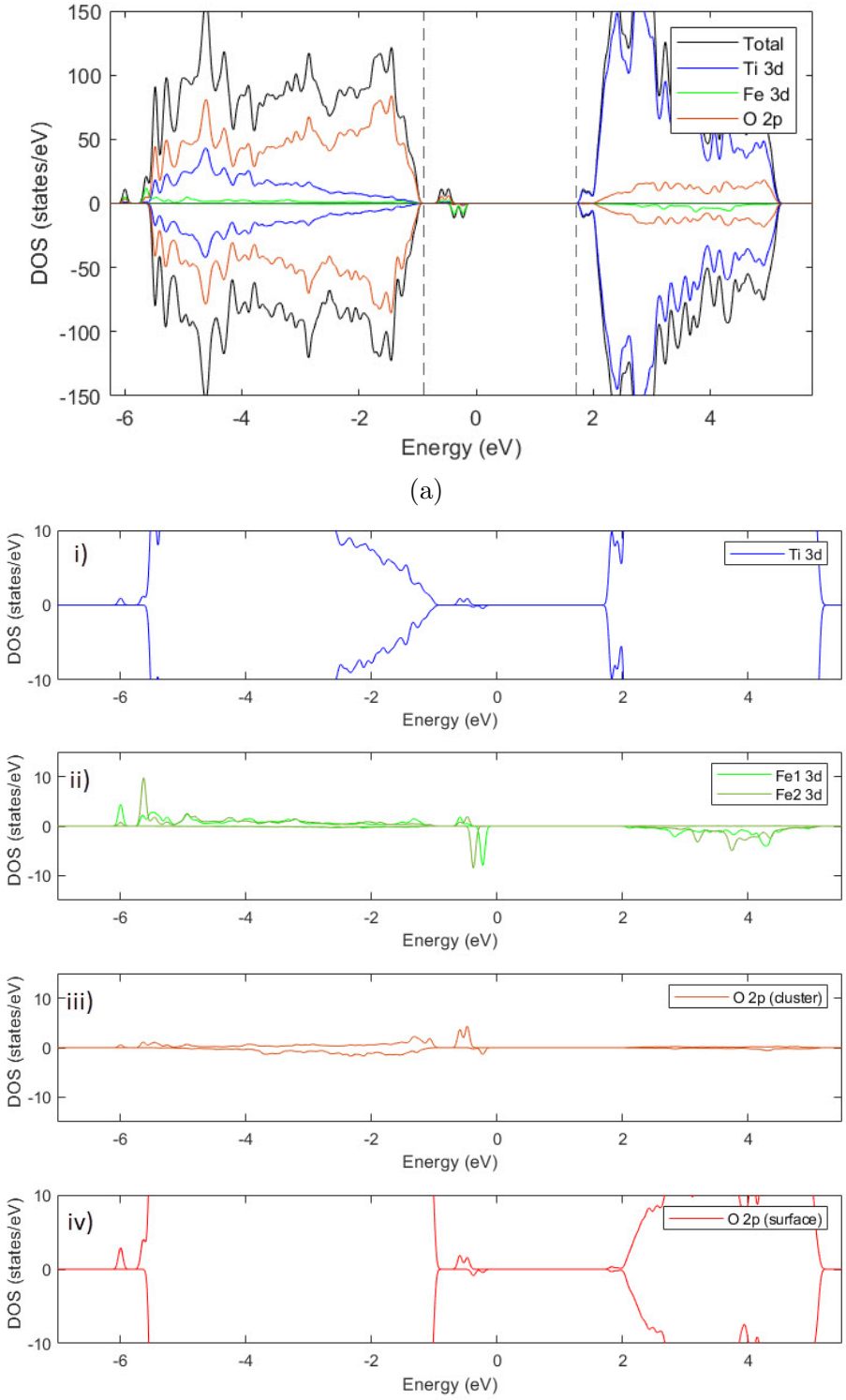

(a)

(b)

Figure 30: a) Overall density of states of the cluster-surface system after the remove of the oxygen atom O3 from the cluster. The VBM and the CBM are indicated by dashed lines at -0.90 eV and 1.7 eV. b) The Partial DOSs of i) Ti states, ii) both Fe1 an Fe2 states and O 2p-states derived from iii) the $Fe_2O_2)_1$ cluster and from iv) the TiO_2 surface.

feature, around Fe atoms indicates 3d orbitals to primarily participate to the charge transfer. Because no nodes are observed in the isosurface in newly formed bonds the sigma bonds are formed between TiO_2 and Fe_2O_3. The DOS of the system revealed an overlap of partial DOSs of Ti, Fe and O, upholding a covalent bonding also in this case.

According to the SDD plot in Figure 32, the main redistribution of the spin density occurs in the Fe_2O_3 cluster. Both orange and turquoise isosurfaces around Fe atoms indicates the Fe also gain an amount of electrons. Again, the charge is depleting from the spin up states while the gained electrons of Fe are occupying the spin down states (Fig. 31a) and Fig. 32a)). That rises the CB of Fe_2O_3 above the CB of TiO_2. This also lowers the magnetic moments of Fe1 and Fe2 closer to 3.7 μ_B which could uphold the +2 oxidation state for them [105] The angles Fe1-O1-Fe2 and Fe1-O2-Fe2 are around 95° which can enabling the superexchange and ferromagnetic interaction between Fe atoms [106] that have most likely the same oxidation state. Small amount of magnetization has also been transferred on the nearest atom of iron but generally less with the vacancy (Fig. 18b)).

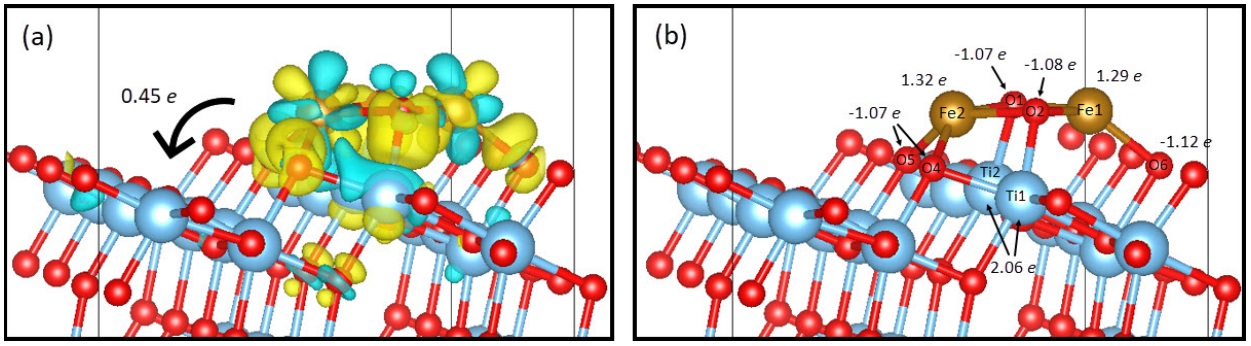

Figure 31: Charge density difference plot and Bader net atomic charges of the selected atoms are shown in a) and b), respectively. The isosurface value is set to 0.005 $e/$Å.

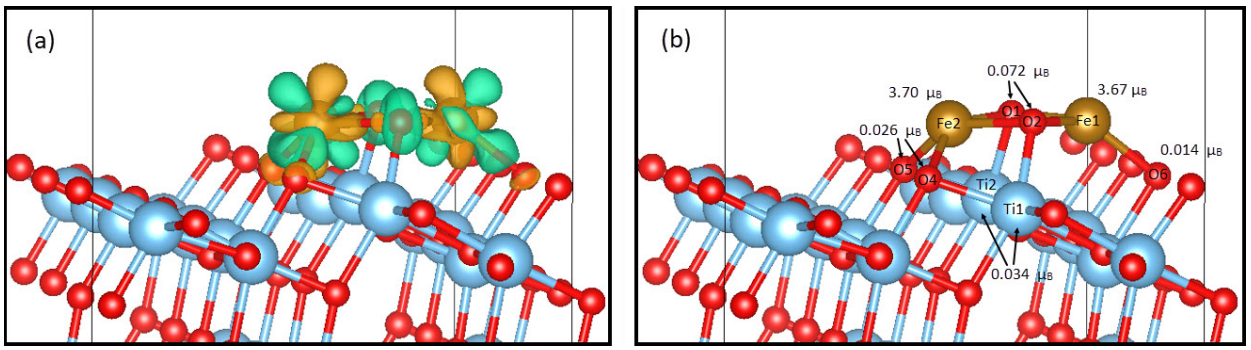

Figure 32: Spin density difference plot and magnetic moments of the selected atoms are shown in a) and b), respectively. The isosurface value is set to 0.005 $e/$Å.

Compared to the $(Fe_2O_3)_1/TiO_2$ the net charge transfer has the direction from the cluster to the surface, but the amount of it was higher. The reason for this could be the band alignment of the conduction bands of TiO_2 and Fe_2O_3. Without the vacancy, we observed shallow impurity states below the CB of TiO_2 that can act as electron traps. Based on the Bader charge analysis we deduced that electrons were eventually accumulating to the CB of TiO_2. However, in the $(Fe_2O_2)_1/TiO_2$ the CB of Fe_2O_3 locates around 0.3 eV above

the CB of Fe_2O_3. The electron excitation is possible from both the VB of TiO_2 and Fe_2O_3 but because of the band alignment the electrons can go directly to the CB of TiO_2. The Fe_2O_3 is no longer trapping the electrons photogenerated electron from the VB or from the CB of TiO_2. Therefore there is no longer so called intermediate stage for electrons due to the Fe_2O_3, and therefore a higher net charge transfer is observed. In addition, because the CB of Fe_2O_3 lies above the CB of TiO_2 the excited electrons from the CB of Fe_2O_3 can be transferred to the CB of TiO_2 [91]. This could improve the reduction ability of TiO_2 even more. At the same time the holes are left to the VB of Fe_2O_3. The oxidation reactions would then take place in Fe_2O_3.

Based on the results, the possible formation of a type II heterojunction could provide efficient separation of the charge carrier in the $(Fe_2O_2)_1/TiO_2$. While the photogenerated electrons are accumulating to TiO_2 the photogenerated holes are accumulating to Fe_2O_3. This could also efficiently suppress the recombination of electrons and holes. In addition, the amount of transferred charge was higher due to which a larger number of electrons and holes could participate to redox reactions. Therefore, the particular oxygen vacancy could lead to a better photocatalytic activity compared to defect-free system, $(Fe_2O_3)_1/TiO_2$. It could improve the reduction ability of TiO_2 as the electrons are accumulating to the surface rather than Fe_2O_3. The band gap energy of 1.8 eV allows the $(Fe_2O_2)_1/TiO_2$ to absorb wavelengths up to 690 nm which almost covers the whole visible light region. The longest red light wavelengths exceed this limit. This, on the other hand, slightly limits the photocatalytic activity of $(Fe_2O_2)_1$. From this we could deduce that the oxygen vacancy in the cluster is not as efficient as oxygen vacancy located in the TiO_2 in order to decrease the band gap energy of TiO_2. However, the system can own other advantageous properties, as discussed.

7.4 Influence of oxygen vacancy to the work function

The work function of the TiO_2 and the defect-free system were found to be 7.23 eV and 6.70 eV. The oxygen vacancy was observed to decrease the work function further. The work function in each investigated reduced systems was close to 5 eV (see Table 3). A neutral oxygen vacancy, which we created, is a positively charged point-defect. Thus it will make the negatively charged surface more positive. It modulates the Fermi-level and vacuum level, and thus the work function. Due to the surface charge being less negative due to oxygen vacancy, it is easier to remove an electron from the surface.

System	Work function ϕ (eV)
$(Fe_2O_3)_1/TiO_2{-}O_v$	5.27
$(Fe_2O_3)_1/TiO_2{-}O_{sv3}$	5.28
$(Fe_2O_2)_1/TiO_2$	5.41

Table 3: The work function of $(Fe_2O_3)_1/TiO_2$ in the presence of the investigated oxygen vacancy sites.

8 Increase the cluster size: $(Fe_2O_3)_2$ on TiO_2 surface

Previous studies have reported that the larger Fe_2O_3 cluster size and the larger Fe_2O_3 concentration can decrease the photocatalytic performance of TiO_2 [39, 36, 37]. Therefore, we have also studied the second smallest cluster size of Fe_2O_3, $(Fe_2O_3)_2$, on the TiO_2 surface. We tried to elucidate whether the larger cluster size could hinder the photocatalytic performance and what could be the primary reason for it.

8.1 Computational details

Correspondingly, we started with the simulation of a free $(Fe_2O_3)_2$ cluster using the simulation box with a side length of 20 Å and only one k-point, Γ-point. The calculations were performed within both the GGA and the GGA+U.

After that we combined the larger cluster and the TiO_2 surface. We used the same simulated supercell for the TiO_2 surface as described in Section 6.1 but instead of $(Fe_2O_3)_1$ cluster we attached the $(Fe_2O_3)_2$ cluster on the anatase TiO_2 surface. The combined system was labelled as $(Fe_2O_3)_2/TiO_2$. Also the same computational parameters were used in these calculations. The binding energy of the $(Fe_2O_3)_2$ cluster is calculated from Equation (6.1) by replacing the energy $E((Fe_2O_3)_1)$ with $E((Fe_2O_3)_2)$. The same observables as previously were computed to investigate this combined system.

8.2 $(Fe_2O_3)_2$ cluster

The optimized geometry of the free $(Fe_2O_3)_2$ cluster within the GGA and the GGA+U are shown in Figure 33. The free cluster has a cage-like structure. Generally, the bond lengths are predicted to be slightly longer by the GGA+U. The bond lengths were 1.73-1.83 Å and 1.77-1.89 Å from the GGA and the GGA+U, respectively (Table 4). This effect was observed also in the case of the $(Fe_2O_3)_1$ cluster and is explained by the added Hubbard correction that accounts for the on-site Coulomb interaction. Both the GGA and the GGA+U predicted the cluster to be ferromagnetic, however, the GGA predicts the magnetic moments of Fe atoms to be only in the range of $1.31 - 2.26\ \mu_B$. The incorrect description of the magnetic properties of Fe_2O_3 by the GGA were already observed when simulating bulk-Fe_2O_3. The GGA+U predicted magnetic moments of 3.26 μ_B for Fe1 and 4.09 μ_B for Fe2, Fe3 and Fe4.

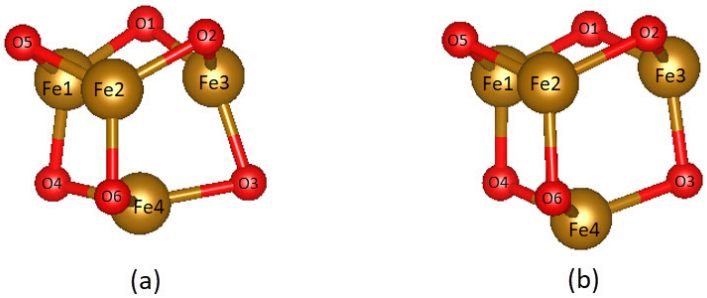

Figure 33: Geometry of the free $(Fe_2O_3)_2$ cluster within a) the GGA and b) the GGA+U exchange-correlation functional.

	r(Å)	
Bond	GGA	GGA+U
Fe1-O1	1.74	1.77
Fe1-O4	1.75	1.77
Fe1-O5	1.74	1.79
Fe2-O2	1.73	1.84
Fe2-O5	1.78	1.88
Fe2-O6	1.73	1.84
Fe3-O1	1.83	1.89
Fe3-O2	1.80	1.84
Fe3-O3	1.80	1.84
Fe4-O3	1.80	1.84
Fe4-O4	1.83	1.89
Fe4-O6	1.80	1.84

Table 4: Bond lengths between the iron and oxygen atoms in the $(Fe_2O_3)_2$ predicted by both the GGA and the GGA+U.

8.3 $(Fe_2O_3)_2$ on TiO_2 surface

The $(Fe_2O_3)_2$ cluster was attached on the anatase TiO_2 surface. At the first try we constructed an initial geometry for the $(Fe_2O_3)_2$ cluster shown in Figure 34a). We started the calculations with the GGA functional. The optimization step of the structure converged. However, the results showed that the cluster did not remain stable, as a cluster, on the surface (Fig. 34b)). To fix this, we tried a different initial structure for the cluster. This time we tried to get it to resemble the cage-like structure of the free $(Fe_2O_3)_2$ cluster (Fig. 34c)). The optimization of the second try finished properly and the optimized geometry of the combined system of TiO_2 and $(Fe_2O_3)_2$ is shown in Figure 34d). The combined system was labelled as $(Fe_2O_3)_2/TiO_2$. Essentially, the cluster remains stable, and using this initial structure after the relaxation the $(Fe_2O_3)_2$ cluster is predicted to retain its cage-like structure on the TiO_2 surface. Its geometry is very close to that of the free $(Fe_2O_3)_2$ cluster. Compared to the $(Fe_2O_3)_1$ cluster this larger cluster seems to be more loosely bonded to the surface. The calculated binding energy of -1.72 eV confirms this. The binding energy is still negative, indicating favourable interaction also between the TiO_2 surface and the $(Fe_2O_3)_2$ cluster. The reason for the failure in the first relaxation stage could be the chosen initial structure that may not have been reasonable enough, what it is in the second try.

Besides the binding energy, we also calculated the work function of the $(Fe_2O_3)_2/TiO_2$. It was found to be 5.90 eV. This is 0.8 eV lower than the work function of the $(Fe_2O_3)_1/TiO_2$. From this we can conclude that a larger Fe_2O_3 cluster reduces the work function of TiO_2 more.

In the case of the previously investigated systems the GGA+U did not change the structure of the combined system dramatically. What was observed to change were the bond lengths, due to taking the on-site Coulomb interaction into account. The geometry of the $(Fe_2O_3)_2/TiO_2$, however, changes significantly by the GGA+U. The obtained structure within the GGA+U is shown in Figure 35. Instead of two bonds, the GGA+U predicts the cluster to form four bonds with the TiO_2 surface. The cluster still retains its cage-like

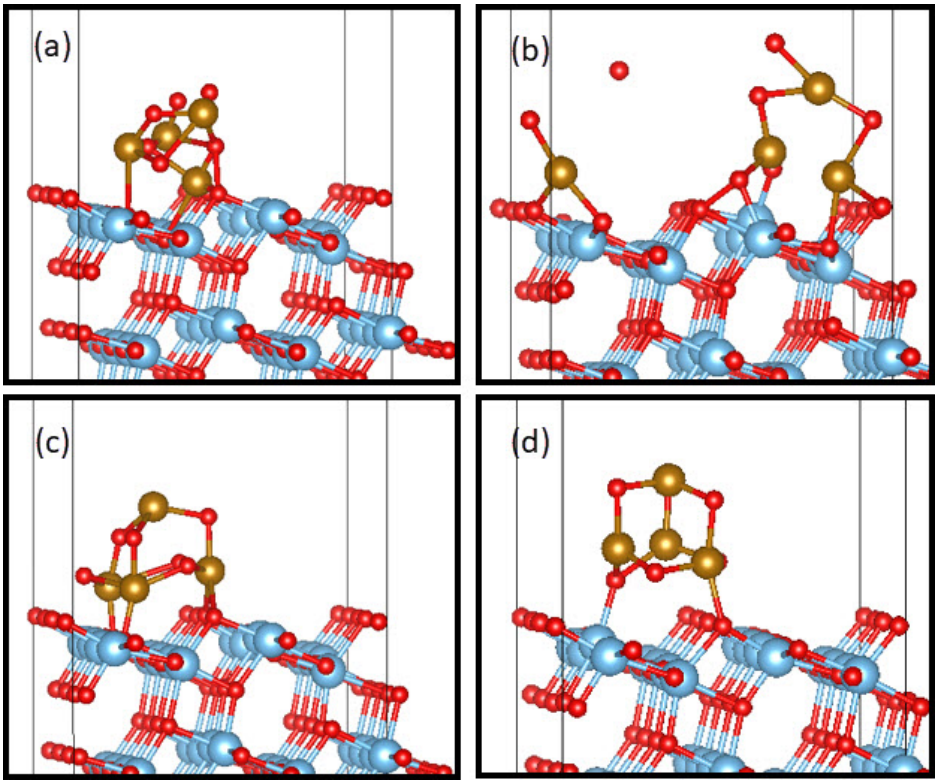

Figure 34: First tried initial structure of the $(Fe_2O_3)_2/TiO_2$ is visualized in a) which resulted in an undesired relax structure shown in b). The more reasonable initial structure and the optimized structure of it are visualized in c) and d), respectively.

structure although it is no longer as spherical and symmetric as the GGA predicts it to be. The GGA+U also predicts slightly larger lattice distortion at the TiO_2 surface.

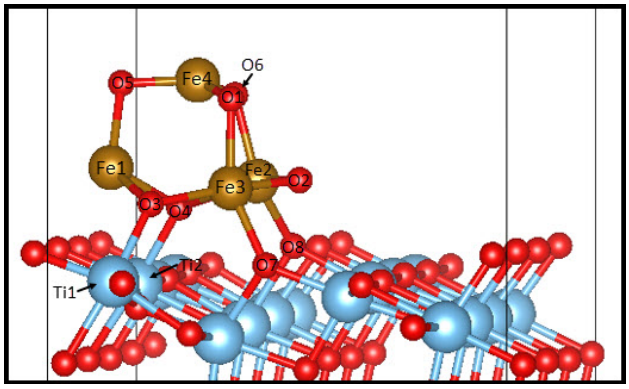

Figure 35: Optimized structure of the $(Fe_2O_3)_2/TiO_2$ within the GGA+U. The selected atoms of the systems are labelled in the figure also.

The electronic structure was computed within the GGA+U for the $(Fe_2O_3)_2/TiO_2$, as usual. The obtained total DOS and the partial DOSs are in Figure 36a). Lot of similarities with the DOS of the $(Fe_2O_3)_1/TiO_2$ can be found. The magnetism is again arising for the iron. Again, in the VB the larger amount of iron states have a spin up polarization while in the CB the majority of the iron state have spin down polarization. This asymmetric partial

DOS upholds the ferromagnetic states for each Fe atom and the observed parallel magnetic moments. There is also iron spin up channel available in the CB, and therefore it does not show a half-metallic nature.

A lot of iron states are appearing below the VB of TiO_2 but we are once again more interested in the Fe_2O_3-derived state in the band gap of TiO_2. Similarly as in the case of the $(Fe_2O_3)_1$ cluster, shallow impurity states are observed above the VB and below the CB of TiO_2. This band alignment indicated the formation of a type I heterojunction. The larger Fe_2O_3 cluster does not change the type of the heterojunction between the anatase TiO_2 surface and the Fe_2O_3 cluster. However, it generates a large number of impurity states in the band gap which are observed to extend farther, toward the middle of the band gap, from the VB and the CB of TiO_2. This reduces the band gap of the combined system to 0.85 eV. This extends the photoresponse of the combined system to even infrared region. The VBM and the CBM of TiO_2 located at around -0.92 eV and 1.62 eV while the VBM and the CBM of Fe_2O_3 were found to be -0.1 eV and -0.75 eV. Thus, the band gap of TiO_2 is remaining pretty much the same, around 2.5 eV, as for the pristine TiO_2 surface.

The charge density and the spin density difference of the $(Fe_2O_3)_2/TiO_2$ are shown in Figure 37. The Bader net atomic charges and magnetization of selected atoms are tabulated in Table 5. The main redistributions are occurring in the cluster, but an amount of charge redistribution is also observed at the TiO_2 surface. The spin density of TiO_2, though does not seem to experience large changes at the surface. The observed magnetic moments uphold that a small amount, smaller than in the presence of the $(Fe_2O_3)_1$ cluster, of magnetization is transferred to the nearest atoms of the cluster at the surface, less than 0.01 μ_B. The oxygen atoms of the cluster also gain various amounts of magnetization. For O2, O3 and O4 they were found to be 0.514 μ_B, 0.126 μ_B and 0.210 μ_B, respectively, while O1, O5 and O6 gain less than 0.01 μ_B. Also the magnetization of Fe atoms are fairly different. It was 4.11 μ_B for Fe2 and 4.20 μ_B for Fe3 but for Fe1 and Fe4 they were 3.77 μ_B and only 2.52 μ_B, respectively. Generally, Fe atoms are mainly surrounded by a turquoise isosurface in the SDD plot, indicating excess spin down polarization. The DOS also revealed unoccupied iron states with spin down polarization in the conduction band. In the conduction band there is also small amount of spin up states. The two spin up peaks locating arising in the conduction band in the DOS originate from Fe4.

Iron is still acting as an electron donor. The Bader net atomic charges of Fe atoms are positive but also their values vary a lot. Fe3 and Fe4 lose electrons 1.48 e and 1.41 e but Fe2 loses more, 1.62 e, while Fe1 loses less, 1.29 e. Based on these it could be that all the Fe atoms may not have the same oxidation state [104]. Oxygen atoms of the $(Fe_2O_3)_2$ cluster are generally gaining around -0.80 e, except O3 and O4, that form bonds with the Ti1 and Ti2 at the surface, gain over -1.00 e. The Bader net atomic charge of Ti atoms in TiO_2 are slightly over 2.00 e so the trend is the same as in the presence of the $(Fe_2O_3)_1$ cluster on the surface. We found the net charge transfer of 0.21 e from the Bader charge analysis, occurring from the cluster to the TiO_2. The possible charge transfer mechanism is probably very similar to that of in the $(Fe_2O_3)_1/TiO_2$. All the shallow impurity states above the VB of TiO_2 are below the Fermi level. The band gap of Fe_2O_3 is only around 1 eV and therefore the electrons are more easily excited in the Fe_2O_3. Still a visible light induced electron excitations are also possible from the VB of TiO_2 to the CB of TiO_2 with the longer wavelengths. The shallow impurity state below the CB of TiO_2 could acting as electron traps. They could trap the photogenerated electrons from the VB of $TiO_2$and

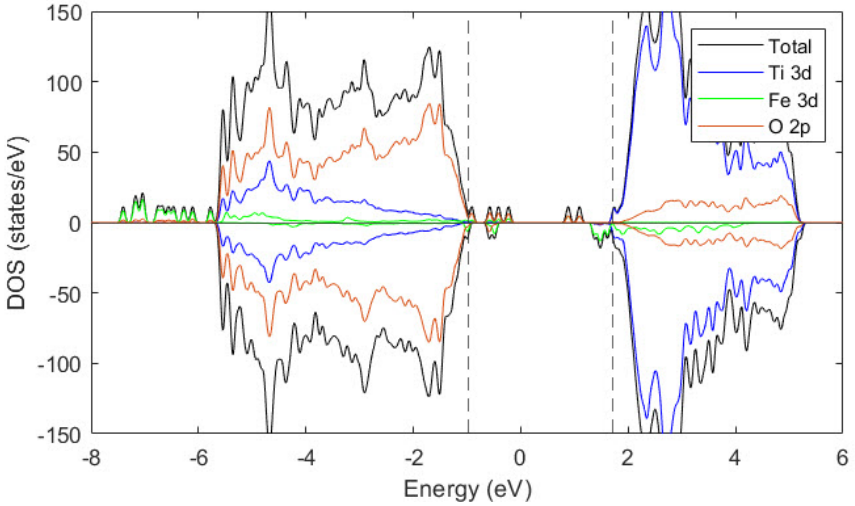

(a)

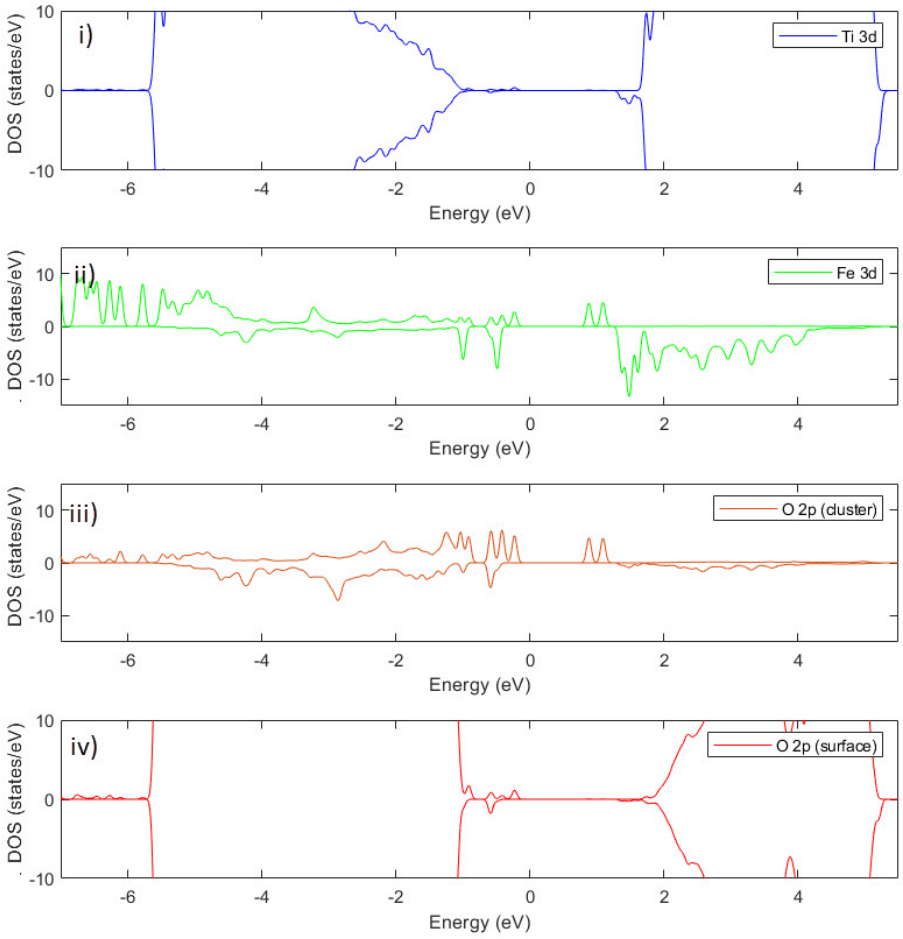

(b)

Figure 36: a) Density of states of the $(Fe_2O_3)_2/TiO_2$. The two dashed lines at -0.97 eV and 1.7 indicate the VBM and the CBM positions of TiO_2. b) The Partial DOSs of i) Ti states, ii) both Fe1 an Fe2 states and O 2p-states derived from iii) the Fe_2O_{32} cluster and from iv) the TiO_2 surface.

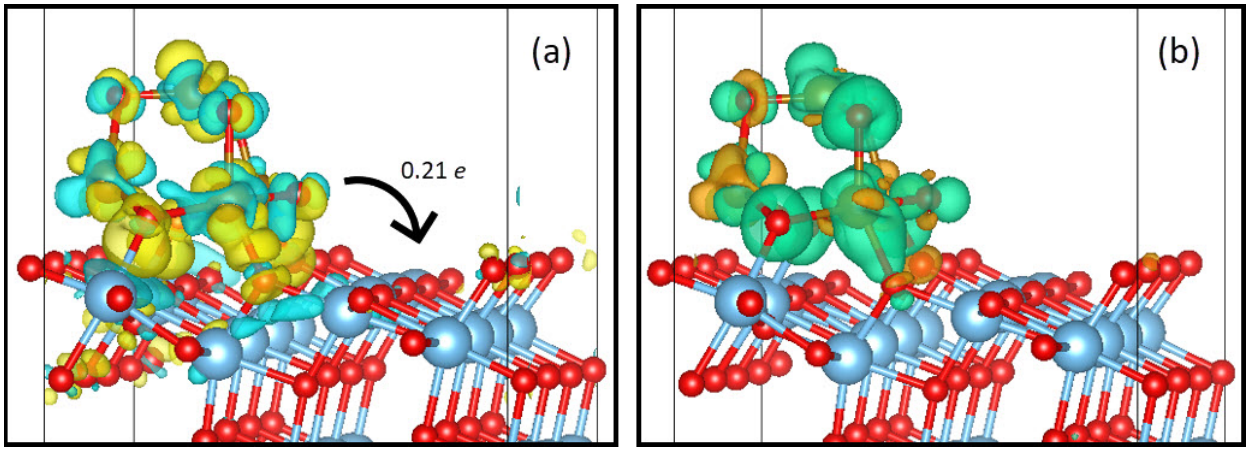

Figure 37: a) Charge density difference and b) spin density difference plots of the $(Fe_2O_3)_2/TiO_2$. The net charge transfer of 0.21 e from the cluster to the surface is indicated by black arrow in a).

in turn the excited electrons from the CB of TiO_2. However, Fe is most likely releasing the trapped electrons in order to receive the stable half-filled configuration. Therefore, the electrons could migrate to the CB of TiO_2. This could be likely to occur also in this system, based on the direction of the net charge transfer.

However, compared to the $(Fe_2O_3)_1/TiO_2$, the net charge transfer is approximately 0.10 e smaller in the $(Fe_2O_3)_2/TiO_2$. In the CB the shallow impurity state are extended farther from the CB of TiO_2. The CBM of Fe_2O_3 is locating at 0.95 e. All the electron trapped by the deeper impurity state may not be transferred to the CB of TiO_2. The VB and the CB of Fe_2O_3 are relatively close each other and therefore, it could be that some of the electrons recombine with the holes left in the VB of Fe_2O_3 before they are transferred to the CB of TiO_2. The narrow band gap enables the activation by all visible light wavelengths and therefore it is not restricting the photocatalytic activity. In addition, the magnetic properties are similar to the defect-free combined system. Therefore, the concentration of Fe_2O_3 can be the primary reason for the reduced amount of charge transfer. As proposed in the previous studies, the larger Fe_2O_3 concentration can change the nature of Fe_2O_3. Rather than improving the photocatalytic activity it can promote the recombination and become a recombination center for the electrons and holes. It could reduce the photocatalytic activity and explain the smaller amount of charge transfer. If the charge transfer properties plays a crucial role in the photocatalytic performance of the system, our results could suggest the larger Fe_2O_3 clusters and the Fe_2O_3 concentration to have a detrimental influence on the photocatalytic performance of TiO_2.

Atom	ρ_{BNAC} (e)	μ (μ_{B})
Fe1	1.29	3.77
Fe2	1.62	4.11
Fe3	1.48	4.20
Fe4	1.41	2.52
O1	-0.757	0.041
O2	-0.868	0.514
O3	-1.07	0.126
O4	-1.181	0.210
O5	-0.835	-0.014
O6	-0.874	0.024
O7	-1.02	0.082
O8	-1.11	0.046
Ti1	2.07	0.044
Ti2	2.06	0.031

Table 5: Bader net atomic charges and magnetic moments of selected atoms in the $(Fe_2O_3)_2/TiO_2$. The labels corresponding to the individual atoms can be found in Figure 35.

9 Conclusions

The aim of this thesis was to study the photocatalytic system formed by titanium oxide and hematite, and gain a better theoretical understanding of photocatalytic processes occurring in it. Further, we study the effect of oxygen vacancy to the photocatalytic process of the system. We proposed a model of α-Fe_2O_3 cluster on anatase TiO_2 (101) surface and this model was simulated using the density functional theory.

We started our investigations by introducing the smallest hematite cluster, $(Fe_2O_3)_1$, on the TiO_2 surface. The negative binding energy of the hematite cluster showed energetically favourable interaction with TiO_2. The work function further identified hematite to act as an electropositive cocatalyst, donating electrons to TiO_2. This was upheld by the Bader charge analysis and charge density difference plot. Due to the adsorption, impurity states arose in the electronic structure of TiO_2. This led to band gap narrowing of the cluster-surface system. The band alignment of TiO_2 and Fe_2O_3 in turn indicated a formation of a type I heterojunction that can be responsible for the observed and notable charge transfer. Thus it can promote the charge transfer and inhibit the recombination of electrons and holes as they were observed to accumulate to the different subsystems. These results indicate that TiO_2 can be a better photocatalyst with the hematite cluster.

We proceeded to investigate the effect of an oxygen vacancy in the combined system of TiO_2 and $(Fe_2O_3)_1$ cluster. An oxygen atom was removed from both the TiO_2 surface and the hematite cluster. Compared to the pristine TiO_2 surface the hematite cluster was generally observed to reduce the formation energy of the oxygen vacancies. In the TiO_2 the subsurface vacancy turned out to be energetically more stable than the surface oxygen vacancy. The subsurface vacancy, chosen to more detailed investigations, also led to a formation of a different type of heterojunction, a type II heterojunction. Further, based on the Bader charge analysis we proposed the subsurface oxygen vacancy to enable the Z-scheme photocatalytic mechanism in the cluster-surface system, leading to a larger charge transfer and efficient charge separation. In the case of surface oxygen vacancy we were not able to deduce the primary photocatalytic process. However, the large formation energy of it and the minor charge transfer make it less favourable compared to the subsurface oxygen vacancy. Generally, the oxygen vacancy was observed to reverse the direction of the charge transfer from the surface to the cluster.

Alternatively, we removed an oxygen atom from the $(Fe_2O_3)_1$ cluster. It was found to be even more stable than the subsurface vacancy in the TiO_2 surface. The band alignment indicated a formation of a type II heterojunction between the TiO_2 and the reduced hematite cluster. It was proposed to enable a larger amount of charge transfer. The charge transfer remained from the cluster to the surface, as in the defect-free cluster-surface system. However, in this case the oxygen vacancy had a less substantial effect in band gap narrowing.

Based on the results we can conclude that the oxygen vacancy locating in the cluster and the subsurface oxygen vacancy in the TiO_2 can be advantageous in order to improve the photocatalytic performance of the investigated cluster-surface system. The formation of heterojunction they provided is generally more efficient than a type I heterojunction. The clear drawback of the former mentioned case was the larger band gap that restricts the utilization of the whole visible light spectrum. Nonetheless, both of them can promote the charge transfer and suppress the recombination rate of the charge carriers. One significant

difference between the effect of these vacancy sites were observed. The subsurface vacancy and the proposed Z-scheme mechanism allow the electrons to accumulate to the Fe_2O_3 and holes to the TiO_2. In the presence of an oxygen vacancy in the cluster the accumulation of the electrons and holes to TiO_2 and Fe_2O_3 was the opposite. Therefore, depending on the location of the oxygen vacancy it seems that we able to either promote the oxidization or reduction ability of TiO_2 in the presence of hematite cluster.

As the last topic, we modelled a second smallest Fe_2O_3 cluster on the TiO_2 surface. The purpose of this simulation was to find support for the proposal of the reduced photocatalytic performance due to the larger Fe_2O_3 cluster size and concentration. The adsorption of the cluster generated impurity state in the band gap, narrowing the band gap and leading to a formation of a type I heterojunction, similarly as the smallest hematite cluster. The amount of charge transfer was though observed to reduce. It indicates that smaller number of electrons and holes can participate to the redox reactions. The larger cluster generated larger amount of impurity states in the band gap which can increase the recombination of the charge carriers, hindering the photocatalytic performance further. Based on these the proposal can be truthful. However, we are not able to confirm of refute this, and state whether the observed changes are due to the larger Fe_2O_3 cluster size or Fe_2O_3 concentration or both.

Fe_2O_3 gave rise to magnetism in the cluster-surface system. Generally the combined system showed a ferromagnetic nature due to iron, also in the presence of oxygen vacancy. However, our results showed the oxygen vacancy to be able to induce a magnetic phase transition in iron and change the cluster-surface system to a ferrimagnetic state. This happened in the presence of the investigated subsurface vacancy. This was proposed to ensue from the notable lattice distortion caused by the vacancy. It still remains unclear what is the influence of magnetism on the photocatalytic process occurring in the cluster-surface system and whether it is an essential factor determining the photocatalytic performance. To obtain further information extensive and intensive studies focusing on the magnetic properties and their relation to the charge transfer processes are needed.

It has to be borne in mind that we did not perform extensive optimization studies of the geometry of hematite clusters on the TiO_2 surface. Indeed, the clusters can have various geometries on the TiO_2 surface and it is possible that one of them is more stable than the others. Depending on the geometry the coordination number of the cluster can vary which can also affect the degree of lattice distortion observed on the TiO_2 surface and further the photocatalytic properties of TiO_2. In this thesis we only investigate the specific constructed models. Further studies could induce the finding of an optimal geometry and global energy minimum of the hematite clusters on the TiO_2 surface.

References

[1] A. T. Al-Fawwaz and M. Abdullah, *Decolorization of Methylene Blue and Malachite Green by Immobilized Desmodesmus sp. Isolated from North Jordan*, Int. J. Environ. Sci., **7**, 95 (2016).

[2] M. Samer, *Biological and Chemical Wastewater Treatment Processes*, Wastewater Treatment Engineering, 1st edition, InTech Europe, 1-50 (2015).

[3] A. Fujishima and K. Honda, *Electrochemical photolysis of water at a semiconductor electrode*, Nature, **238**, 37 (1972).

[4] L. Schlapbach and A. Züttel, *Hydrogen-storage materials for mobile applications*, Nature, **414**, 353 (2001).

[5] S. N. Frank and A. J. Brad, *Semiconductor electrodes. II. Electrochemistry at n-type titanium dioxide electrodes in acetonitrile solutions*, J. Am. Chem. Soc., **97**, 7427 (1975).

[6] Z. Zhang, L. Bai, Z. Li, Y. Qu and L. Jing, *Review of strategies for the fabrication of heterojunctional nanocomposites as efficient visible-light catalysts by modulating excited electrons with appropriate thermodynamic energy*, J. Mater. Chem. A, **7**, 10879 (2019): Figure 1 is from source: Web of Science; date: January 29, 2019.

[7] Y. Nosaka, M. Nakamura and T. Hirakawa, *Behavior of superoxide radicals formed on TiO_2 powder photocatalysts studied by a chemiluminescent probe method*, Phys. Chem. Chem. Phys., **4**, 1088 (2002).

[8] S. C. Lee, H. O. Lintang and L. Yuliati, *High photocatalytic activity of Fe_2O_3/TiO_2 nanocomposites prepared by photodeposition for degradation of 2,4-dichlorophenoxyacetic acid*, Beilstein J. Nanotechnol., **8**, 915 (2017).

[9] B. Guo, H. Shen, K. Shu, Y. Zeng and W. Ning, *The study of the relationship between pore structure and photocatalysis of mesoporous TiO_2*, J. Chem. Sci., **121**, 317 (2009).

[10] F. Huang, A. Yan and H. Zhao, *Influences of Doping on Photocatalytic Properties of TiO2 Photocatalyst*: Semicond. Photocatal. Mater. Mech. Appl., 2016.

[11] A. N. Banerjee, *The design, fabrication, and photocatalytic utility of nanostructured semiconductors: focus on TiO_2-based nanostructures*, Nanotechnol. Sci. Appl., **4**, 35 (2011).

[12] L. Cheng, Q. Xiang, Y. Liao and H. Zhang, *CdS-Based photocatalysts*, Energy Environ. Sci., **11**, 1362 (2018).

[13] X. Meng and Z. Zhang, *Bismuth-based photocatalytic semiconductors: Introduction, challenges and possible approaches*, J. Mol. Cat. A Chem., **423**, 533 (2016).

[14] R.M. Cornell and U. Schwertmann, *The Iron Oxides: Structure, Properties, Reactions, Occurrences and Uses*, 2nd edition, Wiley-VCH, 2003.

[15] E. R. Monazam, R. W. Breault and R. Siriwardane, *Kinetics of Magnetite (Fe_3O_4) Oxidation to Hematite (Fe_2O_3 in Air for Chemical Looping Combustion*, Ind. Eng. Chem. Res., **53**, 13320 (2014).

[16] L. Pauling and S. B. Hendricks, *The crystal structures of hematite and corundum*, J. Am. Chem. Soc., **47**, 781 (1925).

[17] R. Rivera, H. P Pinto, A. Stashans and L. Piedra, *Density functional theory study of Al-doped hematite*, Phys. Scr. **85**, 015602 (2012).

[18] L.W. Finger, R.M. Hazen, emphCrystal structure and isothermal compression of Fe_2O_3, Cr_2O_3, and V_2O_3 to 50 kbars, J. Appl. Phys., **51**, 5362 (1980).

[19])Pâmela Cristine Ladwig Muraro, Sergio Roberto Mortar, Bruno Stefanello Vizzotto, Gabriela Chuy, Cristiane dos Santos, Luis Fernando Wentz Brum and William Leonardo da Silva, *Iron oxide nanocatalyst with titanium and silver nanoparticles: Synthesis, characterization and photocatalytic activity on the degradation of Rhodamine B dye*, Sci. Rep., **10**, 3055 (2020).

[20] J. A. Glasscock, P. R. F. Barnes, I. C. Plumb, A. Bendavid and P. J. Martin, *Structural, optical and electrical properties of undoped polycrystalline hematite thin films produced using filtered arc deposition*, Thin Solid Films, **516**, 1716 (2008).

[21] E. Greenberg, I. Leonov, S. Layek, Z. Konopkova *et al.*, *Pressure-Induced Site-Selective Mott Insulator-Metal Transition in Fe_2O_3*, Phys. Rev. X, **8**, 031059 (2018).

[22] T. Uozumi, K. Okada and A. Kotani, *Theory of photoemission spectra for M_2O_3(M=Ti, V, Cr, Mn, Fe) compounds*, J. Electron Spectrosc. Relat. Phenom., **78**, 103 (1996).

[23] A. Fujimori, M. Saeki, N. Kimizuka, M. Taniguchi and S. Suga, *Photoemission satellites and electronic structure of Fe_2O_3*, Phys. Rev. B, **34**, 7318 (1986).

[24] G. Rollmann, A. Rohrbach, P. Entel and J. Hafner, *First-principle calculation of the structure and magnetic phases of hematite*, Phys. Rev. B, **69**, 165107 (2004).

[25] P. Liao, M. C. Toroker and E. A. Carter, *Electron Transport in Pure and Doped Hematite*, Nano Lett., **11**, 1775 (2011).

[26] N. Iordanova, M. Dupuis and K. M. Rosso, *Charge transport in metal oxides: A theoretical study of hematite α-Fe_2O_3*, J. Chem. Phys., **122**, 144305 (2005).

[27] F. J. Morin, *Electrical Properties of αFe_2O_3 and αFe_2O_3 Containing Titanium*, Physical Review, **83**, 1005 (1951).

[28] T. Nakau, *Electrical conductivity of α-Fe_2O_3*, J. Phys. Soc. Jpn., **15**, 727 (1960).

[29] E. Krén, P. Szabó and G. Konczos, *Neutron diffraction studies on the (1-x)Fe_2O_3-xRh_2O_3 system*, Phys. Lett., **19**, 103 (1965).

[30] J. Lee and S. Han, *Thermodynamics of native point defects in α-Fe_2O_3: an ab initio study*, Phys. Chem. Chem. Phys, **15**, 18906 (2013).

[31] M. N. Huda, A. Walsh, Y. Yan, S. H. Wei and M. M. Al-Jassim, *Electronic, structural, and magnetic effects of 3d transition metals in hematite*, J. Appl. Phys., **107**, 123712 (2010).

[32] N. J. Cherepy, D. B. Liston, J. A. Lovejoy, H. Deng and J. Z. Zhang, *Ultrafast Studies of Photoexcited Electron Dynamic in γ- and α-Fe_2O_3 Semiconductor nanoparticles*, J. Phys. Chem. B, **102**, 770 (1998).

[33] X. Zhang, H. Li, S. Wang, F. R. F. Fan and A. J. Bard, *Improvement of Hematite as Photocatalyst by Doping with Tantalum*, J. Phys. Chem. C, **118**, 16842 (2014).

[34] R. Sugrañez, J. Balbuena, M. Cruz-Yusta, F. Martin, J. Morales and L. Sánchez, *Efficient behaviour of hematite towards the photocatalytic degration of NO_x gases*, Appl. Catal. B. Environ., **165**, 529 (2015).

[35] D. Zhang, Y. Wang, Y. Wang, Y. Zhang, X.M. Song , *Fe_2O_3/NiO photoanode for photocatalytic methanol fuel cell: An insight on solar energy conversion*, J. Alloys Compd., **815**, 152377 (2020).

[36] Y. Xia and L. Yin, *Core-shell structured α-Fe_2O_3@TiO_2 nanocomposites with improved photocatalytic activity in the visible light region*, Phys. Chem. Chem. Phys., **15**, 18627 (2013).

[37] X. Li, H. Lin, X. Chen, H. Niu, J. Liu, T. Zhang and F. Qu, *Dendritic α-Fe_2O_3/TiO_2 nanocomposites with improved visible light photocatalytic activity*, Phys. Chem. Chem. Phys., **18**, 9176 (2016).

[38] J. Liu, S. Yang, W. Wu, Q. Tian, S. Cui, Z. Dai, F. Ren, X. Xiao and C. Jiang, *3D Flowerlike α-Fe_2O_3@TiO_2 Core-Shell Nanostructures: General Synthesis and Enhanced Photocatalytic Performance*, ACS Sustainable Chem. Eng., **3**, 2975 (2015).

[39] J. Deng, Q. Zhuo and X. Lv, *Hierarchical TiO_2/Fe_2O_3 heterojunction photoanode for improved photoelectrochemical water oxidation*, J. Electroanal. Chem., **835**, 287 (2019).

[40] Q. Sun, W. Leng, Z. Li and Y. Xu, *Effect of the surface Fe_2O_3 clusters on the photocatalytic activity of TiO_2 for phenol degradation in water*, J. Hazard. Mater., **229-230**, 224 (2012).

[41] S. J. A. Moniz, S. A. Shevlin, Xiaoqiang, Z-X. Guo and J. Tang, *Fe_2O_3-TiO_2 Nanocomposites for Enhanced Charge Separation and Photocatalytic Activity*, Chem. Eur. J., **20**, 15571 (2014).

[42] Y. Yu, P. Zhang, L. Guo, Z. Chen, Q. Wu, Y. Ding, W. Zheng and Y. Cao, *The Design of TiO_2 Nanostructures (Nanoparticles, Nanotube, and Nanosheet) and Their Photocatalytic activity*, J. Phys. Chem. C, **118**, 12727 (2014).

[43] D. Jassby, J. F. Budarz and M. Wiesner, *Impact of Aggregate Size and Structure on the Photocatalytic Properties of TiO_2 and ZnO Nanoparticles*, Environ. Sci. Technol., **46**, 6934 (2012).

[44] G. M. Pastor, P. Stampfli and K. H. Bennemann, *On the transition from Van der Waals- to metallic bonding in Hg-clusters as a function of cluster size*, Phys. Scr., **34**, 623 (1988).

[45] B. Kaiser and K. Rademann, *Photoelectron spectroscopy of neutral mercury clusters Hg_x ($x \leq 109$) in a molecular beam*, Phys. Rev. Lett., **69**, 3204 (1992).

[46] M. Haruta, *When gold is not noble: catalysis by nanoparticles*, Chem. Rec., **3**, 75 (2003).

[47] J. Melcher, N. Barth, C. Shilde, A. Kwade and D. Bahnemann, *Influence of TiO_2 agglomerate and aggregate sizes on photocatalytic activity*, J. Mater. Sci., **52**, 1047 (2017).

[48] Y. Chen, L. Soler, C. Xie, X. Vendrell, J. Serafin, D. Crespo and J. Llorca, *A straightforward method to prepare supported Au clusters by mechanochemistry and its application in photocatalysis*, Appl. Mater. Today, **21**, 100873 (2020).

[49] A. P. Singh, R. B. Wang, C. Tossi, I. Tittonen, B. Wickman and A. Hellman, *Hydrogen induced interface engineering in Fe_2O_3-TiO_2 heterostructures for efficient charge separation for solar-driven water oxidation in photochemical cells*, RSC Adv., **21**, 4297 (2021).

[50] R. M. Martin, *Electronic Structure, Basic Theory and Practical Methods*, Gambridge University Press, United Kingdom, 2004.

[51] Jorge Kohanoff, *Electronic Structure Calculations for Solid and Molecules, Theory and Computational methods*, Gambridge University Press, United Kingdom, 2006.

[52] P. Elliott, K. Burke and F. Furche, *Excited states from time-dependent density functional theory*, Rev. Comput. Chem., **26**, 91 (2008).

[53] K- Capelle, C.A. Ullrich and G. Vignale, *Degenerate ground states and nonunique potentials: breakdown and restoration of density functionals*, Phys. Rev. A, **76**, 012508 (2007).

[54] D. M. Ceperley and B. J. Alder, *Ground state of the electron gas by a stochastic method*, Phys. Rev. Lett., **45**, 566 (1980).

[55] J.P. Perdew, K. Burke and M. Ernzerhof, *Generalized gradient approximation made simple*, Phys. Rev. Lett., **77**, 3865 (1996).

[56] E.H. Lieb and S. Oxford, *Improved lower bound on the indirect coulomb energy*, Int. J. Quantum Chem., **19**, 427 (1981).

[57] F. Zahariev, S. S. Leang and M. S. Gordon, *Functional derivatives of meta-generalized gradient approximation (meta-GGA) type exchange-correlation density functionals*, J. Chem. Phys., **138**, 224108 (2013).

[58] S. F. Sousa, P. A. Fernandes and M. J. Ramos, *General Performance of Density Functionals*, J. Phys. Chem. A, **111**, 10439 (2007).

[59] J. Sun, A. Ruzsinszky and J. P. Perdew, *Strongly Constrained and Appropriately Normed Semilocal Density Functional*, Phys. Rev. Lett., **115**, 036402 (2015).

[60] J. Tao, J. P. Perdew, V. N. Staroverov, and G. E. Scuseria, *Climbing the Density Functional Ladder: Nonempirical Meta-Generalized Gradient Approximation Designed for Molecules and Solids*, Phys. Rev. Lett., **91**, 146401 (2003).

[61] R. C. Remsing, M. L. Klein and J. Sun, *Dependence of the structure and dynamics of liquid silicon on the choice of density functional approximation*, Phys. Rev. B, **96**, 024203 (2017).

[62] Y. Si, M. Li, Z. Zhou, M. Liu and O. Prezhdo, *Improved description of hematite surfaces by the SCAN functional*, J. Chem. Phys., **152**, 024706 (2020).

[63] J. Sun, J. P. Perdew, and A. Ruzsinszky, *Semilocal density functional obeying a strongly tightened bound for exchange*, PNAS, **112**, 685 (2015).

[64] J.P. Perdew and M. Levy, *Physical Content of the Exact Kohn-Sham Orbital Energies: Band Gaps and Derivative Discontinuities*, Phys. Rev. Lett., **51**, 1884 (1983).

[65] B. Himmetoglu, A. Floris, S. de Gironcoli and M. Cococcioni, *Hubbard-corrected DFT energy functionals: the LDA+U description of correlated systems*, Int. J. Quantum Chem., **114**, 14 (2014).

[66] T. Yanagisawa, M. Miyazaki and K. Yamaji, *Correlated-Electron Systems and High-Temperature Superconductivity*, J. Mod. Phys., **4**, 33 (2013).

[67] M. Cococcioni and S. de Gironcoli, *A linear response approach to the calculation of the effective interaction parameters in the LDA+U method*, Phys. Rev. B, **71**, 035105 (2005).

[68] A. I. Liechtenstein, V. I. Anisimov and J. Zaanen, *Density-functional theory and strong interactions: Orbital ordering in Mott-Hubbard insulators*, Phy. Rev. B, **52**, R5467 (1995).

[69] S. L. Dudarev, G. A. Botton, S. Y. Savrasov, C. J. Humphreys and A. P. Sutton, *Electron-energy-loss spectra and the structural stability of nickel oxide: An LSDA+U study*, Phys. Rev. B, **57**, 1505 (1998).

[70] N.W. Ashcroft and N.D. Mermin, *Solid State Physics*, Saunders College Publishing, New York, 1976.

[71] M. L. Cohen, M. Schlüter, J. R. Chelikowsky, and S. G. Louie, *Self-consistent pseudopotential method for localized configurations: Molecules*, Phys. Rev. B, **12**, 5575 (1975).

[72] H. J. Monkhorst and J. D. Pack, *Special points for Brilloin-zone integrations*, Phys. Rev. B, **13**, 5188 (1976).

[73] P. E. Blöchl, O. Jepsen and O. K. Andersen, *Improved tetrahedron method fro Brillouin-zone integrations*, Phys. Rev. B, **49**, 16223 (1994).

[74] J. Aarons, M. Sarwar, D. Thompsett and C-K. Skylaris, *Perspective: Methods for large-scale density functional calculations on metallic systems*, J. Chem. Phys. **145**, 220901 (2016).

[75] E. Mete, *Electronic properties of transition metal oxides*, Doctoral thesis, Department of Physics, 2003. Available on `https://www.researchgate.net/publication/33575690_Electronic_Properties_of_Transition_Metal_Oxides` (cited 15.5.2021).

[76] D. R. Hamann, M. Schlüter and C. Chiang, *Norm-Conserving Pseudopotentials*, Phys. Rev. Lett., **40**, 1494 (1979).

[77] D. Vanderbilt, *Soft self-consistent pseudopotential in a generalized eigenvalue formalism*, Phys. Rev. B, **41**, 7892 (1990).

[78] Georg K. H. Madsen, P. Blaha, K. Schwarz, E. Sjöstedt and L. Nordström, *Efficient linearization of the augmented plane-wave method*, Phys. Rev. B, **64**, 195134 (2001).

[79] A. V. Nikolaev, D. Lamoen and B. Partoens, *Extension of the basis set of linearized augmented plane wave method (LAPW) by using supplemented tight binding basis functions*, J. Chem. Phys. **145**, 014101 (2016).

[80] P. E. Blöchl, *Projected augmented-wave method*, Phys. Rev. B, **50**, 17953 (1994).

[81] G. Kresse and J. Hafner, *Ab initio molecular dynamics for liquid metals*, Phys. Rev. B, **47**, 558 (1993).

[82] G. Kresse and J. Furthmüller, *Efficient iterative schemes for ab initio total-energy calculations using a plane-wave basis set*, Phys. Rev. B, **54**, 11169 (1996).

[83] K. Momma and F. Izumi, *VESTA: A Three-Dimensional Visualization System for Electronic and Structural Analysis*, J. Appl. Cryst., **41**, 653 (2008).

[84] V. Wang, N. Xu, J. C. Liu, G. Tang and W. T. Geng, *VASPKIT: A User-friendly Interface Facilitating High-throughput Computing and Analysis Using VASP Code*, arVix:1908.08269 (2019).

[85] H. Hellmann, *Einfuührung in die quantenchemie*, Leipzig und Wien: F. Deuticke (1937).

[86] R. P. Feynman, *Forces in Molecules*, Phys. Rev., **56**, 340 (1939).

[87] R. F. W. Bader, *Atoms in Molecules: A Quantum theory*, Oxford University Press, 1990.

[88] G. Henkelman. A. Arnaldsson and H. Jónsson, *A fast and robust algorithm for Bader decompostion of charge dnesity*, Comp. Mater. Sci., **36**, 354 (2006).

[89] M. Yu and D. R. Trinkle, *Accurate and efficient algorithm for Bader charge integration*, J. Chem. Phys., **134**, 064111 (2011).

[90] Q. Pang, H. DorMohammadi, O. Burkan Isgor and L. Árnadóttir, *Density functional theory study on the effect of OH and Cl adsorption on the surface structure of α-Fe_2O_3*, Comput. Theor. Chem., **1100**, 91 (2017).

[91] B. T. Barrocas, N. Ambrožová and K. Kočí, *Photocatalytic Reduction of Carbon Dioxide on TiO_2 Heterojunction Photocatalysts−A Review*, Materials, **15**, 967 (2022).

[92] J. Zhang, P. Zhou, J. Liu and J. Yu, *New Understanding of the difference of photocatalytic activity among anatase, rutile and brookite TiO_2*, Phys. Chem. Chem. Phys., **16**, 20382 (2014).

[93] T. Luttrell, S. Halpegamage, J. Tao, A. Kramer, E. Sutter and M. Batzill, *Why is anatase a better photocatalyst than rutile? - Model studies on epitaxial TiO_2 films*, Sci. Rep., **4**, 1 (2014).

[94] U. Diebold, N. Ruzycki, G. S. Herma and A. Selloni, *One step towards bridging the materials gap: surface studies of TiO_2 anatase*, Catal., **85**, 93 (2003).

[95] A. Y. Ahmed, T. A. Kandiel, T. Oekermann and D. Bahnemann, *Photocatalytic Activities of Different Well-defined Single Crystal TiO_2 Surfaces: Anatase versus Rutile*, J. Phys. Chem. Lett., **2**, 2461 (2011).

[96] C. Günnemann, C. Haisch, M. Fleisch, J. Schneider, A. V. Emeline and D. W. Bahnemann, *Insights into Different Photocatalytic Oxidation Activities of Anatase, Brookite, and Rutile Single-Crystal Facets*, ACS Catal., **9**, 1001 (2019).

[97] A. Majid, S. Zahid, S. U. D. Khan, and S. U. D. Khan, *Theoretical study of (TM)FeO_3 (TM = 3d transition metals) molecular clusters*, J. Nanopart. Res., **22**, 1 (2020).

[98] J. K. Burbett, T. Hughbanks, G. J. Miller, J. W. Richardson Jr. and J. V. Smith, *Structural-electronic relationships in inorganic solids: powder neutron diffraction studies of the rutile and anatase polymorphs of titanium dioxide at 15 and 295 K*, J. Am. Chem. Soc., **109**, 3639 (1987).

[99] E. German, R. Faccio and A. W. Mombrú, *A DFT+U study on structural, electronic, vibrational and thermodynamic properties of TiO_2 polymorphs and hydrogen titanate: tuning the Hubbard 'U-term'*, J. Phys. Commun., **1**, 055006 (2017).

[100] V. Kumaravel, S. Rhatigan, S. Mathew et al., *Indium-Doped TiO_2 Photocatalysts with High-Temperature Anatase Stability*, J. Phys. Chem. C, **123**, 21083 (2019).

[101] J. Wang, J. Huang, J. Meng, Q. Li and J. Yang, *Enhanced photoelectrochemical performance of anatase TiO_2 for water splitting via surface codoping*, RSC Adv., **7**, 39877 (2017).

[102] V. Mansfeldova, M. Zlamalova, H. Tarabkova, P. Janda, M. Vorokhta, L. Piliai and L. Kavan, *Work Function of TiO_2 (Anatase, Rutile, and Brookite) Single Crystal: Effects of the Environment*, J. Phys. Chem. C, **125**, 1902 (2021).

[103] D. Barreca, G. Carraro, A. Gasparotto, C. Maccato, M. E. A. Warwick, K. Kaunisto, C. Sada, S. Turner *et al.*, *Fe_2O_3-TiO_2 Nano-heterostructure Photoanodes for Highly Efficient Solar Water oxidation*, Adv. Mater. Interfaces, **2**, 1500313 (2015).

[104] S. Posysaev, O. Miroshnichenko, M Alatalo, D. Le and T. S. Rahman, *Oxidation states of binary oxides from data analytics of the electronic structure*, Comp. Mat. Sci., **161**, 403 (2019).

[105] G. Geneste, C. Paillard and B. Dkhil, *Polarons, vacancies, vacancy associations, and defect states in multiferroic $BiFeO_3$*, Phys. Rev. B, **99**, 024104 (2019).

[106] N. Ota or Ohta, *Ferromagnetic Order Analysis of Fe-and FeO-modified Graphene-nano-ribbon*, arXiv.org. arXiv. 1310.7740. 10.3379/msjmag.1402R011 (2013).

[107] N. S. Portillo-Vélez, O. Olvera-Neria, I. Hérnandez-Pérez and A. Rubio-Ponce, *Localized electronic states induced by oxygen vacancies on anatase TiO_2 (101) surface*, Surf. Sci., **616**, 115 (2013).

[108] H. H. Pham and L.W. Wang, *Oxygen vacancy and hole conduction in amorphous TiO_2*, Phys. Chem. Chem. Phys., **17**, 541 (2015).

[109] D. Li, H. Haneda, N. K. Labhsetwar, S. Hishita and N. Ohashi, *Visible-light-driven photocatalysis on fluorine-doped TiO_2 powders by the creation of surface oxygen vacancies*, Chem. Phys. Lett., **401**, 579 (2005).

[110] X. Shen, G. Doug, L. Wang, L. Ye and J. Sun, *Enhancing Photocatalytic Activity of NO Removal through an In Situ Control of Oxygen Vacancies in Growth of TiO_2*, Adv. Mater. Interfaces, Advanced Materials **6**, 1901032 (2019).

[111] Z. Zhang, X. Wang, J. Long, Q. Gu, Z. Ding and X. Fu, *Nitrogen-doped titanium dioxide visible light photocatalyst: Spectroscopic identification of photoactive centers*, J. Catal., **276**, 201 (2015).

[112] H. Li, Y. Guo and J. Robertson, *Calculation of TiO_2 Surface and Subsurface Oxygen Vacancy by the Screened Exchange Functional*, J. Chem. Phys. C, **119**, 18160 (2015).

[113] H. Cheng and A. Selloni, *Surface and subsurface oxygen vacancies in anatase TiO_2 and differences with rutile*, Phys. Rev. B, **79**, 092101 (2009).

[114] S. W. Hoh, L. Thomas, G. Jones and D. J. Willock, *A density functional study of oxygen vacancy formation on α-Fe_2O_3(0001) surface and the effect of supported Au nanoparticles*, Res. Chem. Intermed., **41**, 9587 (2015).

[115] V. Kumaravel, E. Bianchetti, S. Mathew, S. J. Hinder, J. Bartlett, C. Di Valentin and S. C. Pillai,*New Insights into Crystal Defects, Oxygen Vacancies, and Phase Transition of Ir-TiO_2*, J. Phys. Chem. C, **125**, 23548 (2021).

[116] J. R. De Lile, S. G. Kang, Y.A. Song and S. G. Lee, *Investigating Polaron Formation in Anatase and Brookite TiO_2 by Density Functional Theory with Hybrid-Functional and DFT+U Methods*, ACS Omega, **4**, 8056 (2019).

[117] P.-G. de Gennes, *Effect of Double Exchange in Magnetic crystals*, Phys. Rev., **118**, 141 (1960).

[118] S. K. Mishra, D. Mazumdar, K. Tarafdar, L.W. Wang, S.D. Kevan, S. Sanchez-Hanke, A. Gupta and S. Roy, *Altered magnetism and new electronic length scales in magnetoelectric* $La_{2/3}Sr_{1/3}MnO_3{-}BiFeO_3$ *heterointerface*, New J. Phys., **15**, 113042 (2013).

[119] C. Menéndez, D. Chu and C. Carzola, *Oxygen-vacancy induced magnetic phase transitions in multiferroic thin films*, Comput. Mater., **6**, 76 (2020).